Using parity-violating weak interaction to measure neutron matter density and search for new physics

by

Sakib Rahman

A thesis submitted to
The Faculty of Graduate Studies of
The University of Manitoba
in partial fulfillment of the requirements
of the degree of

DOCTOR OF PHILOSOPHY

Physics And Astronomy
The University of Manitoba
Winnipeg, Manitoba, Canada
December 2021

Thesis advisor | Author
Juliette Mammei | **Sakib Rahman**

Using parity-violating weak interaction to measure neutron matter density and search for new physics

Abstract

The weak interaction is the only fundamental interaction in nature that violates parity symmetry. Parity-violation produces asymmetric outcomes in mirror image experiments. The high-precision asymmetry measurements, using electrons with rapidly flipping polarization as probes, have extraordinary scientific reach across various subfields. PREX-2 and MOLLER are two such experiments that can only be conducted at the state-of-the-art Thomas Jefferson National Accelerator Facility. The asymmetries (A_{PV}) measured at PREX-2 and MOLLER kinematics (Q^2), can help to estimate the density distributions in neutron-rich matter and search for Physics Beyond the Standard Model respectively. PREX-2 was conducted by scattering a longitudinally polarized 953 MeV electron beam elastically from ^{208}Pb at a ~ 5 degree scattering angle. The measured asymmetry was $A_{PV} = 550 \pm 16$ [stat.] $\pm\, 8$ [sys.] ppb at average $Q^2 = 0.00616$ GeV^2. Together with PREX-1, it imposes robust constraints on the interior baryon density (0.1480 ± 0.0036 [exp.] $\pm\, 0.0013$ [theo.] fm^{-3}) and the neutron skin (0.283 ± 0.071 fm) of ^{208}Pb. Model correlations between the neutron skin and the nuclear symmetry pressure indicate a stiff symmetry energy near the nuclear saturation density. Together with neutron star observations, it enhances the understanding of exotic matter states. In contrast to PREX-2, MOLLER will operate with an 11 GeV longitudinally polarized electron beam as the flagship experiment utilizing the 12 GeV upgrade at Jefferson Lab. The electrons will be scattered from atomic electrons in a liquid hydrogen target and the scattered electrons will be guided by a novel spectrometer with full azimuthal coverage to an array of quartz Cerenkov detectors.

The asymmetry and consequently the weak charge of the electron will be measured to a precision of 2.4% at average $Q^2 = 0.0056$ GeV^2. The value of the electroweak mixing angle derived from the above measurement can be compared to the Standard Model prediction in search of a deviation. MOLLER is sensitive to new physics in the MeV to multi-TeV range. This dissertation details the PREX-2 measurement and the current design status of MOLLER, highlighting my contributions towards PREX-2 data analysis and optimization of MOLLER experimental subsystems.

Contents

List of Figures

List of Tables

Acknowledgments

I would like to begin by thanking the professors, staff, and fellow students who have aided my pursuit of higher education in physics over the past 11 years. I want to specially acknowledge my current supervisor Dr. Juliette Mammei for guiding me through most of my undergraduate and graduate research career. I also want to acknowledge Dr. Shelley Page who gave me my first undergraduate research project. I am grateful for the expert research support that I have received from Dr. Michael Gericke, Dr. Wouter Deconinck, Dr. Paul King, Dr. Krishna Kumar, Dr. Kent Paschke, Dr. Ciprian Gal, Dr. Chandan Ghosh, the Jefferson Lab magnet engineering group (Dr. Probir Ghoshal, Dr. Ruben Fair, and other brilliant engineers), and many others working on PREX-2 and MOLLER. I also want to thank Dr. Samar Safi-Harb and Dr. Georg Schreckenbach for being part of my graduate advisory group. In addition, I want to thank Susan Beshta, Maiko Langelaar, and Dr. Peiqing Wang at the department of physics and astronomy and the Westgrid/Compute Canada research scientists Dr. Grigory Shamov and Dr. Ali Kerrache for their excellent administrative and technical support. I have met and worked with some incredible students over my educational career. Special thanks to Cameron Clarke for collaborating on a great many tasks with me and the entire PREX-2 student analysis group for their unbelievable effort.

My educational journey would not have been possible without my extended family and friends over 3 different countries. I have been fortunate to live with many kind people who have shown me the same love as my parents. I am grateful to my uncle Hasan Mahmood for opening his home to me as I sought a better school for secondary education in Bangladesh. I am thankful to Ms. Iris Land and her family for accepting me as a foreign exchange student in USA and treating me with incredible generosity and kindness. I also want to thank my friend Henry Petker and his family for giving me my first real job in Canada and inviting me to spend a winter break with them. I also cherish the friends I made at school and university even though I have struggled to keep in touch with most. Lastly, I thank my spouse Ishraat Masood and her family for supporting me during the hard years and long hours of graduate school.

It is best that I end this acknowledgment with a tribute to the teachers who influenced my life the most. Suman Sir first introduced me to the beauty of Mathematics. Farhana Miss instilled great discipline in me as my class teacher during highschool. I sorely miss late Ashish Sir who taught me how to bind my understanding of mathematics and physical sciences together. Finally, I want to mention the teachers I had in the USA, including Ms. Sally Brock and late Ms. Debbie Lloyd, who helped me adjust to a different educational culture and curriculum in a very short time. My teachers taught me the important role educators have in shaping the leaders of tomorrow. They deserve our utmost respect and every child deserves the same quality of education that I had growing up.

I extend my sincere gratitude towards Natural Sciences and Engineering Research Council (NSERC) of Canada, Canadian Foundation of Innovations (CFI), WestGrid (www.westgrid.ca) and Compute Canada/ Calcul Canada (www.computecanada.ca) for the direct support enabling most of my research. I also want to thank the US National Science Foundation (NSF), US Department of Energy (USDOE) and Jefferson Lab Science Associates (JSA) for their funding and resource contributions towards PREX-2 and MOLLER.

To my family and friends who supported me through tough times. In loving memory of my grandparents Khalilur Rahman, Saburonnesa, S M A Wahid and Rabeya Begum. And to the memory of my late teacher Ashish Kumar Saha who inspired me to pursue science.

Chapter 1

Introduction

In this chapter, I discuss the scientific significance of PREX-2 and MOLLER. Both are high-precision parity-violating electron scattering experiments. In addition, I list my contributions within the context of the experiments. A document roadmap is also provided to aid in navigating the dissertation.

1.1 Overview

Out of the four fundamental interactions of nature, only the weak interaction violates parity symmetry or symmetry under sign reversal of spatial dimensions. It was first reported in 1957 that electrons, emitted during the conversion of neutrons to protons via β-transformation inside a polarized ^{60}Co nucleus, preferentially emitted in the direction opposite to the nuclear spin [Wu et al., 1957]. With the nuclear spin oriented in a particular direction with an external magnetic field, electrons emitted in that direction (N_{-}) and the opposite direction (N_{+}) were counted over a period of time. The measured relative difference in counts was the parity-violating asymmetry

$$A_{PV} = \frac{N_{+} - N_{-}}{N_{+} + N_{-}} \tag{1.1}$$

So, the probability of weak interaction is dependent on underlying physical properties of the electrons that change sign with the sign reversal of spatial dimensions [Povh et al., 2015]. Helicity is one such property that defines the relative alignment between spin and momentum. A positive helicity electron has the spin and momentum directions aligned whereas a negative helicity electron has the spin and momentum directions anti-aligned. Modern fixed-target parity-violating electron scattering experiments precisely measure the asymmetry between the rates of electrons with opposite helicities after scattering from stationary targets at chosen kinematics. The state-of-the-art Continuous Electron Beam Accelerator Facility (CEBAF) at the Thomas Jefferson National Laboratory (JLAB), Virginia, USA offers excellent instrumental support to facilitate such experiments [Horowitz et al., 2014]. The recently conducted second iteration of the Lead Radius Experiment (PREX-2) at JLAB used parity-violating elastic electron-nucleus scattering to measure the neutron skin, the difference between nuclear proton and neutron distribution radii, of ^{208}Pb nucleus. This constrained neutron matter density from a range of nuclear structure models. The Measurement of Lepton-Lepton Electroweak Reaction (MOLLER) experiment is a future experiment that will build on the experience of PREX-2 in terms of instrumental capabilities and systemic error controls to search for Physics Beyond the Standard Model using parity-violating electron-electron scattering [Kumar et al., 2014]. PREX-2 and MOLLER will yield useful insights from the perspectives of particle physics, nuclear physics, atomic physics, and astrophysics [Piekarewicz and Fattoyev, 2019; Kumar et al., 2014]. A broader overview of scientific significance is provided in section 1.2. I specifically contributed towards PREX-2 data analysis and optimization of various MOLLER subsystems. The scope of this dissertation, defined in Section 1.3, is to discuss the results and implications from PREX-2, the current conceptual design of MOLLER, and my specific contributions.

1.2 Scientific Significance

In this section, I discuss the scientific significance of PREX-2 and MOLLER in more detail. I also discuss my integral contributions to both experiments.

1.2.1 PREX-2

The objective of the PREX-2 experiment was to measure the parity-violating asymmetry to a high precision when polarized electrons with 953 MeV energy scatter elastically from ^{208}Pb at a 5 degree scattering angle with average $Q^2 = 0.00616$ GeV^2. The measured asymmetry is sensitive to the nuclear weak charge distribution. The relationship can be expressed by the following equation

$$A_{PV} = \frac{G_F Q^2 \left|Q_W\right|}{4\sqrt{2}\pi\alpha Z} \frac{F_W\left(Q^2\right)}{F_{ch}\left(Q^2\right)} \tag{1.2}$$

where A_{PV} is the parity-violating asymmetry, G_F is the Fermi coupling constant, Q_W is the weak charge of the nucleus, Q is the four-momentum transfer and F_W/F_{ch} is the weak/electromagnetic form factor [the Fourier transform of the weak/electromagnetic charge distribution]. Since the weak charge content of the neutrons is much higher than the protons, the weak charge distribution roughly mimics the neutron distribution [Paschke et al., 2011]. The asymmetry measurement led to a determination of the radius of the nuclear neutron distribution (R_n) to 1.4% precision. The difference between R_n and the radius of the nuclear proton distribution (R_p) (probed with electromagnetic interaction) gives the neutron skin of ^{208}Pb. As shown in figure 1.1, there is a strong correlation between model predictions for the neutron skin and the nuclear symmetry pressure [Roca-Maza et al., 2011]. Determination of the symmetry pressure at different densities helps to determine the equation of state (pressure as a function of density) of neutron-rich matter and hence, the distribution of neutrons within small (nuclei) and large (neutron star) aggregates [Piekarewicz and Fattoyev, 2019].

Figure 1.1: Correlation between model predictions of neutron skin and symmetry pressure (density dependence of symmetry energy). Reprinted figure with permission from X. Roca-Maza, M. Centelles, X. Viñas, and M. Warda. Neutron skin of ^{208}Pb, nuclear symmetry energy, and the parity radius experiment. Phys. Rev. Lett., 106(25):252501, June 2011. The nuclear symmetry pressure dictates how neutrons are distributed within neutron-rich aggregates. If the predictions for the ^{208}Pb neutron skin ($R_n - R_p$) is plotted against the predictions for nuclear symmetry pressure (L) from a range of nuclear structure models, a very strong correlation can be observed as shown by the blue regression line [Roca-Maza et al., 2011]. The inner colored band represents the 95% confidence interval and the outer colored band represents the 95% prediction interval. Therefore, measuring the neutron skin constrains the valid nuclear structure models, which are based on different assumptions of neutron matter density. The figure shows the dotted boundary limits for valid models based on a specific assumption of neutron skin and the corresponding symmetry pressure value (green points with error bars).

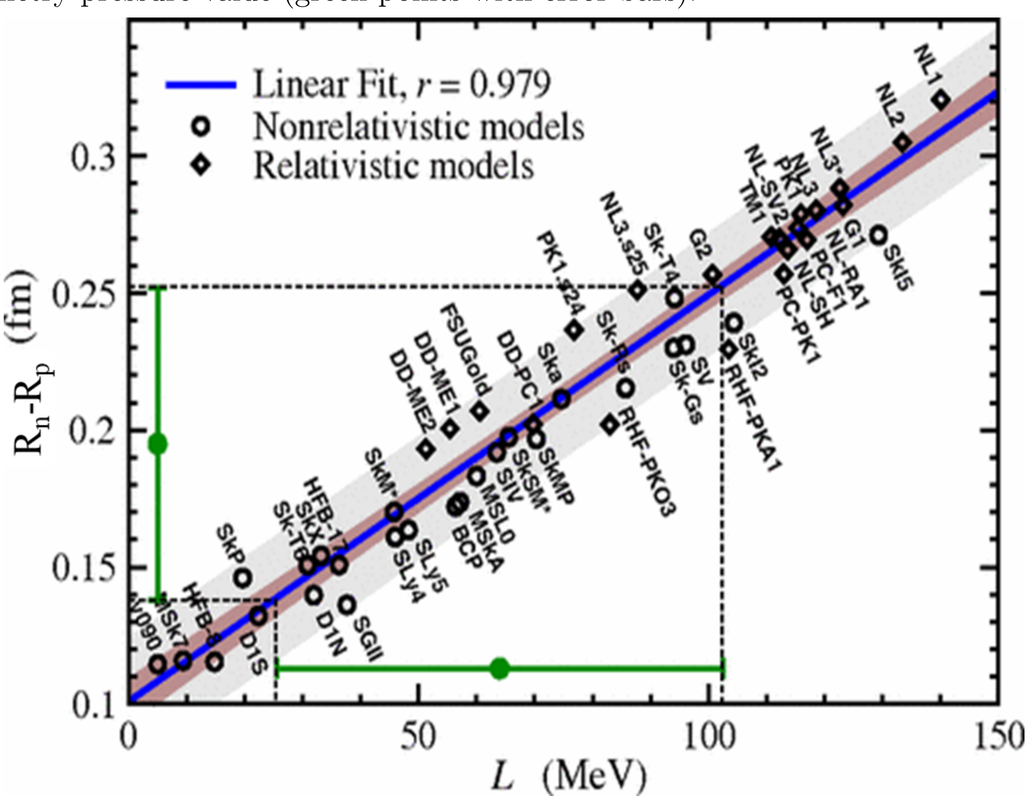

Figure 1.2 highlights many connections to the PREX-2 experiment across various fields. The PREX-2 experiment will complement high-impact studies in astrophysics. The radii of neutron stars can now be measured directly with the NICER telescope on-board the international space station. For a given mass, the radius has a specific correlation with the nuclear symmetry pressure [Piekarewicz and Fattoyev, 2019]. So, an equation of state can be extracted. The PREX-2 and NICER measurements place indirect constraints on the tidal deformability of neutron stars. The observed **GW**170817 gravitational wave event predicted a neutron star tidal deformability limit [Abbott et al., 2018] that shows a 1 standard deviation tension with the combined constraint from PREX-2 and NICER [Reed et al., 2021]. So, this may offer hints of phase transitions in the interior of neutron stars, with the symmetry pressure going from small to large as the neutron matter density decreases.

Heavy ion collision studies at facilities such as RIKEN in Japan, FRIB in USA, and FAIR in Germany will yield further information on the nuclear symmetry pressure at densities higher than the nuclear saturation density. FRIB, specifically, will be using strongly interacting probes to measure the neutron skin of exotic nuclear isotopes and achieve new constraints on nuclear structure models. The PREX-2 result will supply critical calibrating anchors for these studies [Piekarewicz and Fattoyev, 2019].

PREX-2 will also aid precision tests to search for Physics Beyond the Standard Model. Atomic parity-violation experiments use the interaction between the atomic electrons and the nucleus in heavy isotopes such as ^{133}Cs to search for new physics. The uncertainty arising from neutron skin correction in such a measurement will be reduced by the precise measurement of neutron distribution in PREX-2. As of 2005, the induced theoretical uncertainty was 0.5%, which was still comparable to the experimental error bar for the atomic parity-violation amplitude [Wieman and Derevianko, 2019]. Technical improvements made for PREX-2, such as, improvements in injector, polarimeters, beam monitors, tracking, data acquisition systems, etc. will be vital for MOLLER, which is a future Standard Model test.

Figure 1.2: Connections to PREX-2 [Piekarewicz and Fattoyev, 2019; Abbott et al., 2018; Wieman and Derevianko, 2019; Reed et al., 2021; Becker et al., 2018].

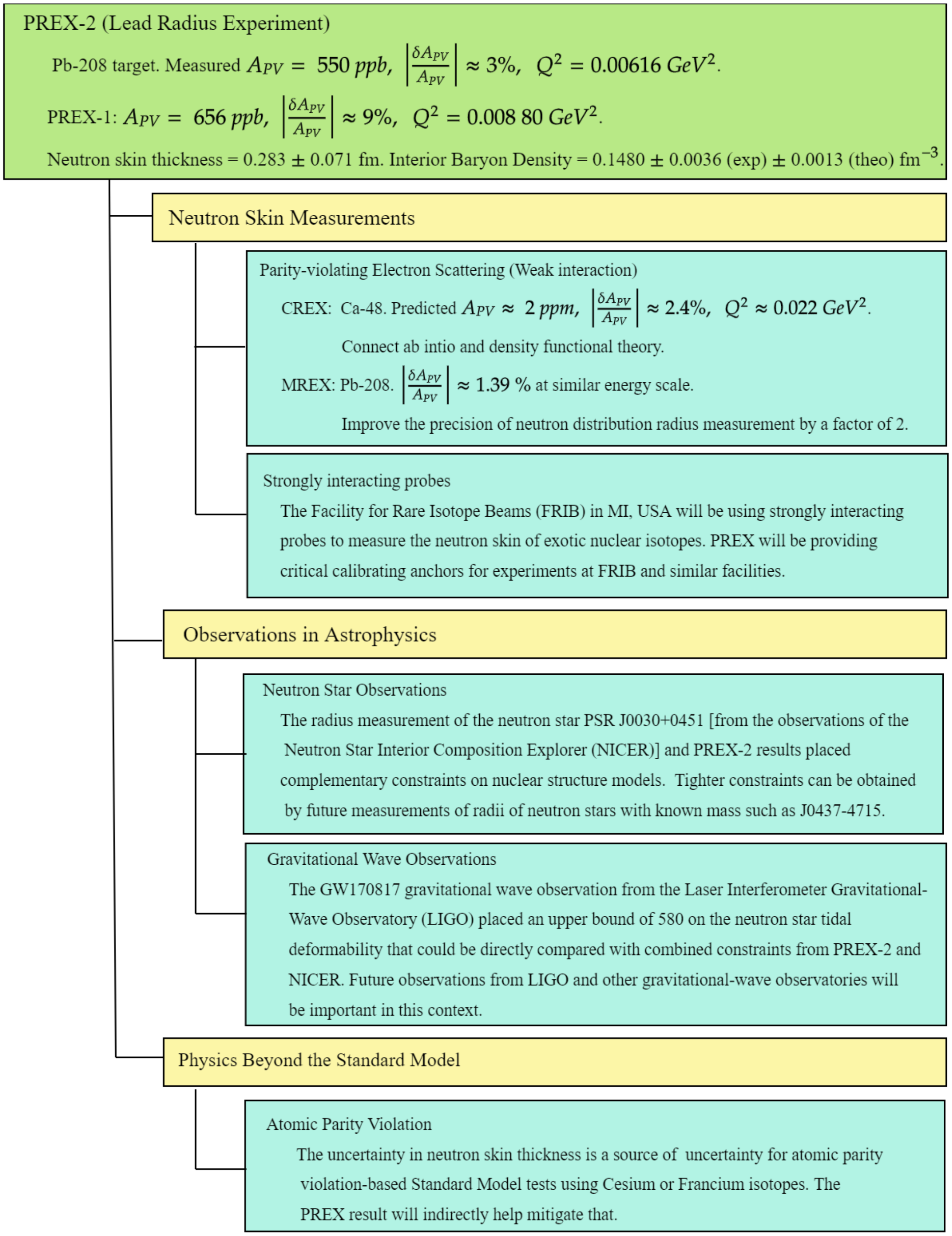

For PREX-2, my principal contribution was towards the development of analysis tools. I worked on a feature on the analysis software JAPAN (Just Another Parity Analyzer) which produced a summary of information related to each period of experimental running. I also worked on a data aggregator tool which allowed monitoring of data quality over different time scales. The tools helped to account for both quick changes and slow drifts in factors such as beam quality that the asymmetry is sensitive to. In addition, I worked as an experimental shift worker and a weekly analysis coordinator assisting in the collection and processing of good data. During my shifts in the commissioning period, I was involved in the optics alignment process which defines the kinematics for the experiment. Further details are provided in section 4.1.

1.2.2 MOLLER

The MOLLER experiment will measure the parity-violating asymmetry to a precision of 0.7 parts per billion (ppb) when polarized 11 GeV electrons are scattered from unpolarized atomic electrons in a liquid hydrogen target with average $Q^2 = 0.0056$ GeV^2. The measured asymmetry is related to the weak charge of the electron (Q^e_W) by the following expression,

$$A_{PV} = mE\frac{G_F}{\sqrt{2}\pi\alpha}\frac{4\sin^2\theta}{(3+\cos^2\theta)^2}Q^e_W = mE\frac{G_F}{\sqrt{2}\pi\alpha}\frac{2y(1-y)}{1+y^4+(1-y)^4}Q^e_W \tag{1.3}$$

where α is the fine structure constant, G_F is the Fermi constant, m is the mass of the electron, θ is the scattering angle in the center-of-mass (COM) frame, and $y = 1 - \frac{E'}{E}$ with E and E' being the energy before and after scattering respectively.

In turn, the weak charge is related to the electroweak mixing angle (θ_W) as follows,

$$Q^e_W = 1 - 4\sin^2\theta_W \tag{1.4}$$

$\sin^2\theta_W$ is an important parameter whose measurement can be used to look for deviations from the prediction of the electroweak theory within the Standard Model. If

Figure 1.3: The running of the electroweak mixing angle. Reprinted figure with kind permission from the European Physical Journal (EPJ) [Becker et al., 2018]. The blue line shows the theoretical prediction of $\sin^2(\theta_W)$ from the Standard Model as a function of the energy scale (μ) using the modified minimal subtraction loop renormalization scheme [Zyla et al., 2020]. At lower energy, the $\sin^2(\theta_W)$ value is higher resulting in a reduction of the weak charge and increase in fractional accuracy. The MOLLER measurement will be conducted in the low energy scale ($\mu \sim 0.075$ GeV) and benefits from not having any complications due to theoretical uncertainties associated with the strong interaction. The result from the completed QWEAK experiment (using elastic electron-proton scattering) is shifted vertically for comparison of uncertainties with the expected MOLLER result. The MOLLER experiment will be sensitive to new neutral interactions with amplitudes as low as $\sim 10^{-3} G_F$ and possible multi-TeV mediator particles [Kumar et al., 2014].

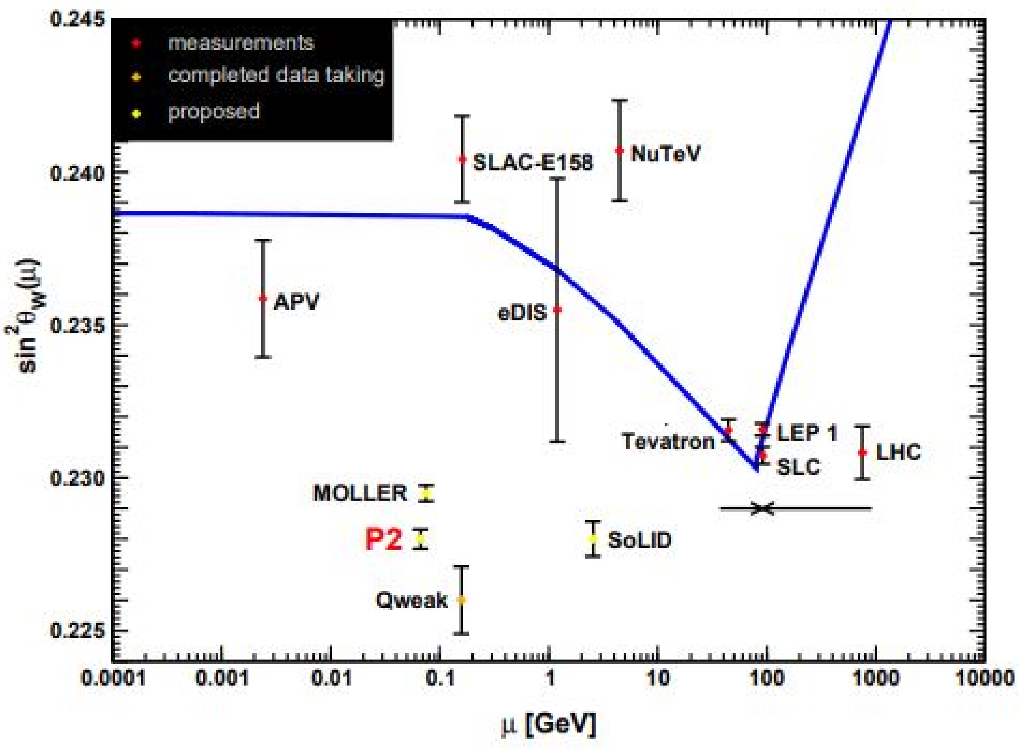

Figure 1.4: Connections to MOLLER [Becker et al., 2018; Zyla et al., 2020; Behr and Gwinner, 2009; The SLAC E158 Collaboration, 2005; The Jefferson Lab QWEAK Collaboration, 2018].

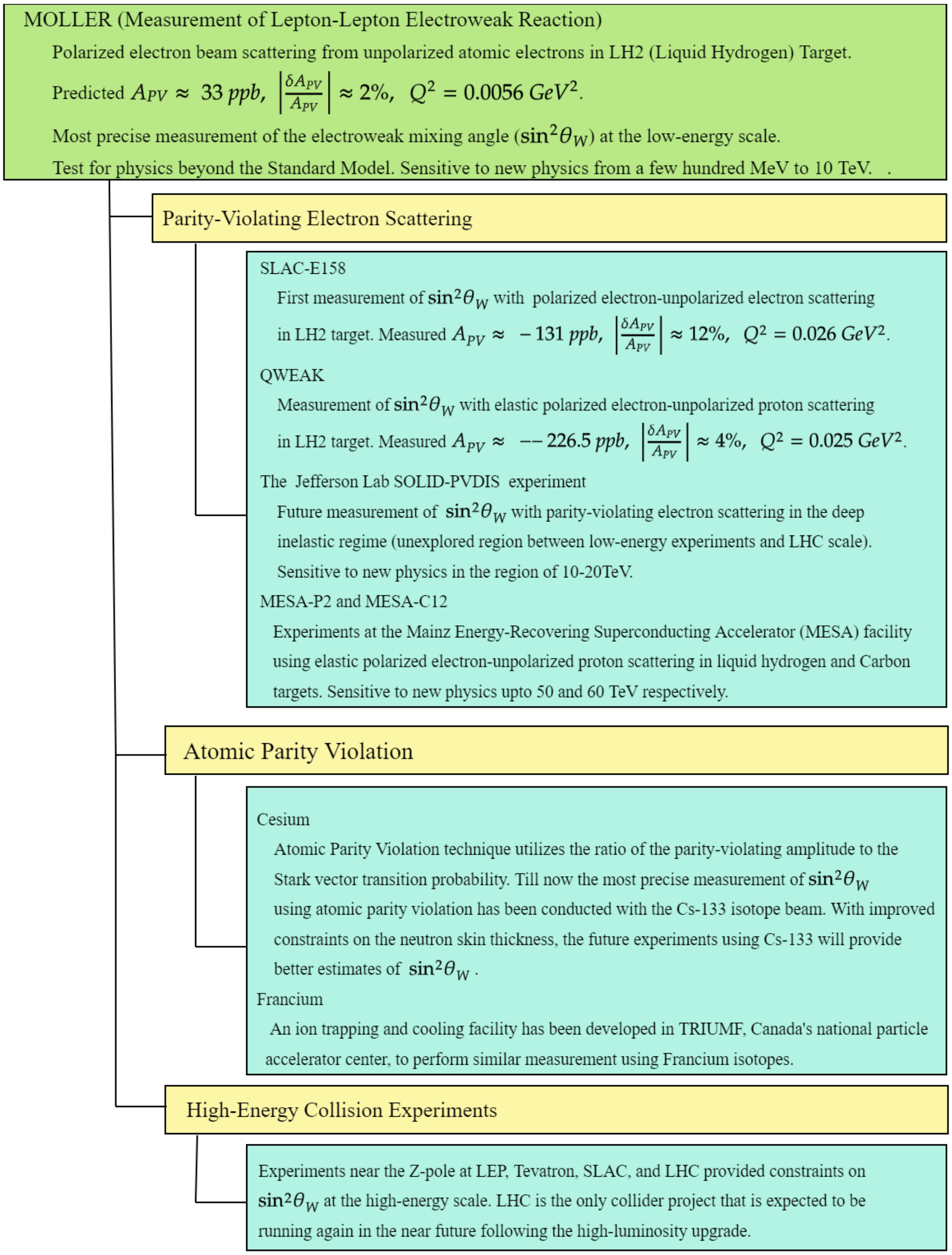

higher order effects are included by a theoretical technique called loop renormalization, $\sin^2\theta_W$ runs as a function of the energy scale as shown in figure 1.3. The 0.7 ppb precision on the asymmetry translates to a 2.4% relative precision on the weak charge and a highly accurate measurement of the electroweak mixing angle at the energy scale of the MOLLER experiment. Such an accurate measurement at the low-energy scale will complement high-energy searches for Physics Beyond the Standard Model at collider experiments and in atomic parity violation experiments [Kumar et al., 2014; Zyla et al., 2020; Behr and Gwinner, 2009]. Figure 1.4 highlights some of the experimental efforts that are relevant to MOLLER.

For MOLLER, I contributed towards development of the software framework used for the design optimizations of various experimental subsystems such as the spectrometer that defines the experimental kinematics and the main detector array. The description of the software tools I developed along with results of some critical studies are provided in section 5.1 and 5.2.

1.3 Personal Contributions

In this section, I provide a list of my contributions to peer-reviewed publications, conference presentations, technical reports, and code repositories during the course of my work on PREX-2 and MOLLER.

- **Peer-Reviewed Publications**
  - K. D. Paschke, S. Rahman, $\cdots$, and PREX Collaboration. An accurate determination of the neutron skin thickness of ^{208}Pb through parity-violation in electron scattering. Phys. Rev. Lett., 126 : 172502, Apr. 2021
  - S. Riordan, Y. X. Zhao, $\cdots$, and S. Rahman. Study of light backgrounds from relativistic electrons in air light-guides. Nucl. Instrum. Methods Phys. Res. A, 896 : 96–102, July 2018.

  - P. K. Ghoshal, R. J. Fair, $\cdots$, and S. Rahman. General failure modes and effects analysis for accelerator and detector magnet design at jlab. IEEE Transactions on Applied Superconductivity, 30(8) : 1–11, 2020.
  - D. Becker, S. Rahman, $\cdots$, and P2 collaboration. The P2 experiment: A future high-precision measurement of the weak mixing angle at low momentum transfer. Eur. Phys. J. A, 54(11), Nov. 2018.

- **Conference Presentations**
  - S. Rahman. Simulation and performance of radiation shielding for recent and future parity-violating electron scattering experiments at Jefferson Lab. In 2020 Fall Meeting of the APS Division of Nuclear Physics. American Physical Society, Nov. 2020.
  - S. Rahman. Spectrometer and Detector Simulations for the MOLLER Experiment. Winter Nuclear and Particle Physics Conference, 2017.
  - S. Rahman. MOLLER Background Studies. Fall Meeting of the American Physical Society Division of Nuclear Physics, 2016.
  - S. Rahman. MOLLER Detector Simulations and Background Studies. National Nuclear Physics Summer School, 2016.
  - S. Rahman. Spectrometer Sensitivity Studies for the MOLLER Experiment at Jefferson Lab. Winter Nuclear and Particle Physics Conference, 2014.

- **Technical Reports**
  - K. S. Kumar, S. Rahman, $\cdots$, and MOLLER Collaboration. The MOLLER project conceptual design report, 2020. URL https://moller.jlab.org/cgi-bin/DocDB/public/ShowDocument?docid=630. Accessed: 2021-2-10.

- R. Fair, S. Rahman, J. Mammei, and C. Gal. Hybrid vs. segmented downselect. https://moller.jlab.org/cgi-bin/DocDB/public/ShowDocument?docid=660, 2020*b*.
- S. Rahman. FOM analysis for shortening the target. https://moller.jlab.org/cgi-bin/DocDB/public/ShowDocument?docid=584, 2019.

- **Code Repositories**
  - C. Clarke, S. Rahman, $\cdots$, and MOLLER Simulation Group. Generator of GDML detector description of the main detector array in the Jefferson Lab 12 GeV MOLLER experiment. https://github.com/JeffersonLab/remoll-detector-generator, 2017.
  - S. Rahman. Scripts for submitting slurm array jobs for remoll simulation and analysis. https://github.com/JeffersonLab/remoll-job-submission, 2021.
  - S. Rahman, W. Deconinck, $\cdots$, and MOLLER Simulation Group. Generator for producing GDML file for remoll showermax detectors. https://github.com/JeffersonLab/remoll-showermax-generator, 2021a.
  - S. Rahman, W. Deconinck, $\cdots$, and MOLLER Simulation Group. Code for generating GDML file of spectrometer magnets in remoll. https://github.com/JeffersonLab/remoll-coil-generator, 2021b.
  - S. Rahman, J. Mammei, $\cdots$, and MOLLER Simulation Group. Code to post-process field map files for remoll. https://github.com/JeffersonLab/remoll-fieldmap-processor, 2021c.
  - S. Riordan, S. Rahman, $\cdots$, and MOLLER Simulation Group. Simulations for the MOLLER experiment at Jefferson Lab. https://github.com/JeffersonLab/remoll, 2013.

– S. Rahman, $\cdots$, and PREX Collaboration. Just another parity analyzer. https://github.com/JeffersonLab/japan, 2018.

1.4 Document Roadmap

The following document roadmap is provided to aid in navigating the detailed information contained in different chapters.

- **Chapter** 1: This chapter contains a brief discussion of the scientific significance of PREX-2 and MOLLER, parity-violating electron scattering experiments furthering our understanding of nature. It also contains an introduction to my work on both experiments and a document roadmap.
- **Chapter** 2: This chapter contains description of relevant concepts- particles, forces and symmetries. It also provides a short introduction to the theory behind parity-violating electron scattering experiments. It concludes with discussions of the neutron skin and the electroweak mixing angle respectively, the main measurable quantities of PREX-2 and MOLLER.
- **Chapter** 3: This chapter covers the infrastructure support provided by the Thomas Jefferson National Accelerator Facility (Jefferson Lab/JLAB), specifically the polarized beam injector and the beam property monitoring tools that are relevant for PREX-2 and MOLLER. The description of the PREX-2 apparatus and the conceptual design of the MOLLER apparatus inside hall A of JLAB are also provided.
- **Chapter** 4: This chapter describes my contributions towards development of analysis tools for PREX-2 and my contributions as a experimental shift worker and weekly analysis coordinator. Important analyses performed by fellow collaborators that led to final result for the overall experiment are also included.

It concludes with a discussion of the final measured asymmetry and derived neutron matter properties.

- **Chapter** 5: This chapter describes my contribution towards the development of simulation framework for MOLLER and the results of some critical design studies for various subsystems.

- **Chapter** 6: This chapter summarizes the results from PREX-2, the progress in MOLLER design, and discusses other current and future experiments that will improve on the knowledge gained from PREX-2 and MOLLER.

Chapter 2

Theory and Foundations

In this chapter, I describe the theoretical framework that is relevant for PREX-2 and MOLLER. I start with a discussion of the Standard Model of particle physics in its current state covering all the fundamental particles and interactions. Then I discuss the exploitation of parity symmetry violation due to weak interaction in electron scattering as an experimental technique that is used in PREX-2 and MOLLER. Since PREX-2 and MOLLER are sensitive to neutron matter properties and Physics Beyond the Standard Model respectively, the theory regarding both topics are briefly discussed as well.

2.1 The Standard Model of Particle Physics

The Standard Model of particle physics, as shown in figure 2.1, is the model of all known particles that make up our universe and the fundamental interactions/-forces between them. It describes the mediators for the electromagnetic, weak and strong interactions and their self-interactions. It also describes how the mediators interact with the matter and anti-matter fields resulting in the manifestation of the fundamental forces. In addition, it describes the interaction of matter particles and force mediators with the Higgs field which imparts mass to them, and the Higgs self-interactions [Woithe et al., 2017]. The only fundamental interaction that is not covered by the Standard Model is gravity.

Figure 2.1: The Standard Model of particle physics. Created based on source image [Dominguez, 2020]. It includes 6 flavors of quarks: up (u), down (d), charm (c), strange (s), top (t), and bottom (b), along with 6 flavors of leptons: electron (e), electron neutrino (ν_e), muon (μ), muon neutrino (ν_μ), tauon (τ), and tauon neutrino (ν_τ). The particles are divided into three generations in increasing order of their masses. Quarks and leptons together make up the particles which form matter. The model also contains the mediator particles for three out of four fundamental interactions: photons (γ) for the electromagnetic interaction, 8 types of gluons (g) for the strong interaction and weak bosons ($W^+, W^-,$ and Z^0) for the weak interaction. In the Standard Model, only the particles which interact with the Higgs field gain mass. The Higgs (H) boson is an excitation of the Higgs field.

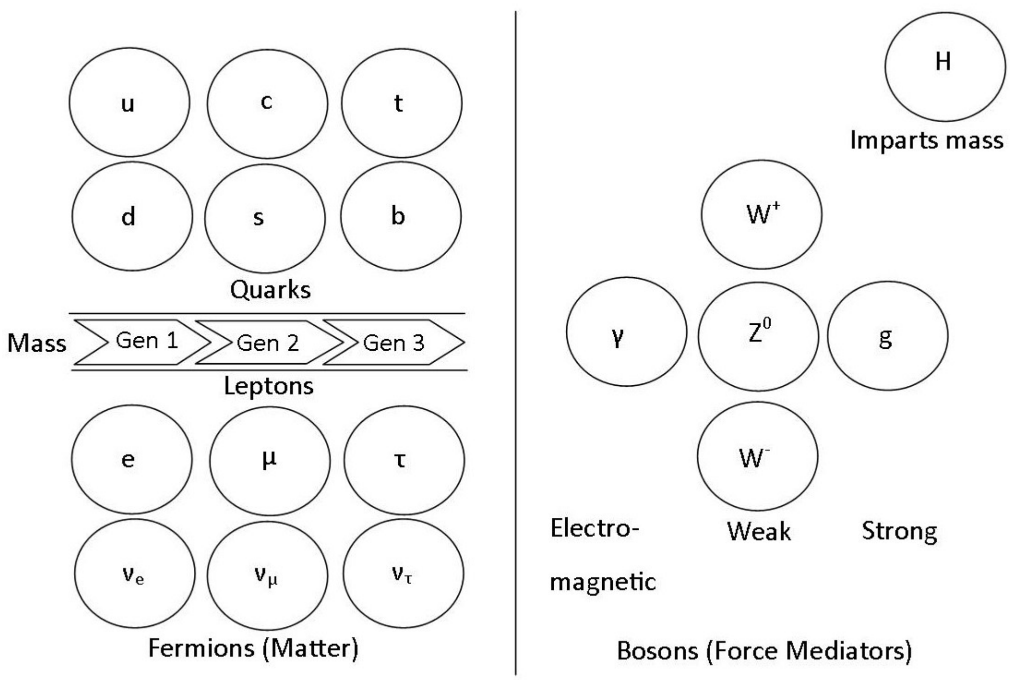

The matter particles are all fermions since their spin (intrinsic angular momentum) is $\frac{1}{2}$. The matter particles can be categorized into quarks and leptons. In each category, there are 6 flavors grouped into 3 generations in increasing order of their masses. Both quarks and leptons can change flavors. In the case of quarks, inter-generational transitions are suppressed but that is not true for leptons. Each matter particle has a corresponding anti-particle with the same mass which is characterized by the flavor quantum numbers (ex: electric charge, etc.) having the opposite sign [Povh et al., 2015].

The mediators are vector bosons with spin 1 and the Higgs particle is a scalar boson with spin 0. Analogous to electric charge in electromagnetic interaction, there are color charge and weak charge for the strong and weak interactions. The strength of the interaction between any two particles depends on the charge content. Additionally, interactions with more massive mediator particles operate over shorter distances. The photons, which mediate the electromagnetic interaction, do not carry electric charge and hence do not interact among themselves. The photons are also massless because they do not interact with the Higgs boson. Consequently, the electromagnetic interaction has infinite range. The gluons, which mediate the strong interaction, are also massless but they interact among themselves because they carry the color charge. So, the strong interaction has a shorter effective range than the electromagnetic interaction. This is also the reason behind color confinement which means that particles carrying color charge can only exist in bound states. The W^+, W^-, and Z^0 particles, which mediate the weak interaction, are massive because they interact heavily with the Higgs field and consequently, the weak interaction operates over very short distances [Povh et al., 2015]. The weak interaction is also unique in the sense that it violates the parity symmetry. In the next section, I discuss how parity-violating electron scattering can be a powerful experimental technique to explore fundamental physics.

2.2 Parity-Violating Electron Scattering

Figure 2.2: Helicity. Created based on source image [Griffiths, 1987]. An electron has positive helicity if its spin and momentum are aligned and negative helicity if its spin and momentum are anti-aligned.

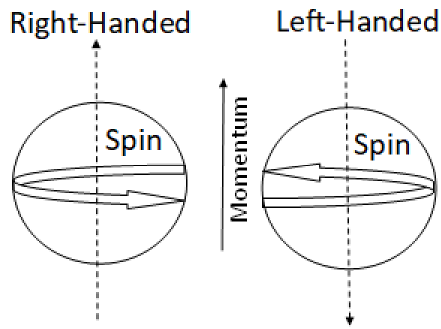

Consider a polarized electron beam with rapidly flipping spin hitting a target. The spin ($\mathbf{s}$) and momentum ($\mathbf{p}$) of the electrons at any point of time determines a property of the electrons in the beam known as helicity, as shown in figure 2.2. The mathematical formulation for helicity is,

$$h = \frac{\mathbf{s} \cdot \mathbf{p}}{|\mathbf{s}|\,|\mathbf{p}|} \tag{2.1}$$

For relativistic electrons interacting via the weak interaction, helicity can be correlated with chirality or handedness. If the spin and momentum direction of the electrons are aligned, they are right-handed, and if the spin and momentum direction are anti-aligned, they are left-handed. This applies to fermions in general too [Povh et al., 2015].

If the parity operator is acted upon an electron, the direction of the momentum is reversed under spatial inversion but the spin preserves itself. This results in a sign change of the helicity. So, any interaction dependent on helicity violates parity. The mediators for the weak interactions do not couple with left-handed and right-handed electrons with equal strength. Therefore, the weak interaction is a parity-violating interaction.

In a parity-violating electron scattering experiment, the incoming polarized electrons scatter from the designated target and are propagated through a system of collimators and magnets and focused onto a detector system. Due to the parity-violating nature of the weak interaction, there is a difference in detected yields between the two helicity states. A relative difference in cross-sections/probabilities of interaction between the two states is defined as the parity-violating asymmetry (A_{PV}). So,

$$A_{PV} = \frac{\sigma_R - \sigma_L}{\sigma_R + \sigma_L} \tag{2.2}$$

where σ_R and σ_L are the scattering cross-sections for right-handed and left-handed electrons respectively. The objective of the experiment is to measure the (A_{PV}) with extreme precision, minimizing the sources of error (backgrounds, false asymmetries, etc.).

However, the asymmetry measurement alone is not sufficient from the perspective of theoretical interpretation. A measurement of the four-momentum transfer squared (Q^2) is also needed. The Q^2 can be expressed by the following equation,

$$Q^2 = 2EE'(1 - \cos(\theta)) \tag{2.3}$$

where E is the incident energy, E' is the final momentum of scattered electron, and θ is the scattering angle. For elastic scattering, the equation can be rewritten as

$$Q^2 = 2E'^2 f_r'(1 - \cos(\theta)) \tag{2.4}$$

where $f_r' = \frac{1}{1 - \frac{E'}{m}(1 - \cos(\theta))}$ is the recoil factor [Liyanage et al., 2011].

Under experimental conditions, the relative probability of an scattered electron making it to the detectors depends on geometric acceptance, magnetic fields, and radiative energy losses. The probability is known as the acceptance function and usually expressed as a function $\epsilon(\theta)$ of lab scattering angle (θ). The final measured A_{PV} and Q^2 in a parity-violating electron scattering experiment are average values over the acceptance function [PREX Collaboration, 2021]. The asymmetry determination at the specific kinematics can be linked with fundamental physical quantities such as neutron skin of heavy nuclei, electroweak mixing angle etc. and they can be determined to very high precision. Therefore, the technique enables PREX-2 and MOLLER to explore neutron matter properties and Physics Beyond the Standard Model respectively. In the next two sections, the relevant theory is discussed.

2.3 Neutron Skin and Neutron Matter

The radius of the atomic nucleus approximately obeys the following empirical relation [Povh et al., 2015],

$$R \propto A^{\frac{1}{3}} \tag{2.5}$$

where R denotes the radius and A denotes the mass number. The mass number is the total number of neutrons and protons in the nucleus which are together referred to as nucleons. The distribution of nucleons within the nucleus is not necessarily uniform. To understand how the neutrons and protons are distributed within the nucleus, it is important to consider different contributions to the energy that binds the nucleus together. Modeling the nucleus as an incompressible liquid drop, the binding energy can be expressed by Weizsäcker's semi-empirical formula [Povh et al., 2015; Piekarewicz and Fattoyev, 2019],

$$B(A,Z) = a_v A - a_s A^{\frac{2}{3}} - a_c \frac{Z^2}{A^{\frac{1}{3}}} - \frac{\delta}{A^{\frac{1}{2}}} - a_a \frac{(N-Z)^2}{4A} \tag{2.6}$$

where the coefficients a_v, a_s, a_c, a_a, and δ are experimentally determined. The proportionality relationships for the individual terms need to be interpreted separately. The first term is referred to as the volume term and the linear dependence on A reflects that the force exerted by a nucleon inside a nucleus does not extend beyond its immediate neighbor nucleons. The term would grow as $A(A-1) \sim A^2$ if each nucleon interacted with the remaining $(A-1)$ nucleons. This is known as nuclear saturation and results in most nuclei having identical central density of $\rho_0 = 0.17\ \text{fm}^{-3}$ [Povh et al., 2015; Piekarewicz and Fattoyev, 2019]. The second term is a correction arising from the fact that surface nucleons have less neighbor nucleons to interact with and is proportional to the surface area of the nucleus leading to a dependence on $R^2 \sim \left(A^{\frac{1}{3}}\right)^2 = A^{\frac{2}{3}}$. The third term is an expression of long range Coulomb repulsion among protons and hence goes as $\frac{Z(Z-1)}{R} \sim \frac{Z^2}{A^{\frac{1}{3}}}$. The fourth term is known as the pairing term which reflects the reality that nuclei with even number of protons and neutrons are more stable compared to those with odd-numbered constituents. The term that is most relevant to PREX-2 is the last term known as the asymmetry term. As nuclei get heavier, they tend to favor accumulating more neutrons compared to protons due to the increasing Coulomb repulsion but a penalty is applied for the resulting asymmetry. A nuclear system is considered more stable if it has an overall higher binding energy, that is, the contribution from the correction terms are minimized. The symmetry energy is higher at the core than the surface of the nucleus and hence an outward symmetry pressure is generated due to the energy gradient. This is countered by the surface tension which tries to minimize the surface area by pushing the nucleons back towards the core. So, the excess neutrons in a heavy nucleus are expected to gravitate towards the surface and form a skin over the charged core if the symmetry pressure is larger than the surface tension pressure. The skin is thicker with higher symmetry pressure as shown in figure 2.3. The thickness of this skin when measured will put a constraint on the symmetry pressure and hence the symmetry energy at the surface where the nuclear density is at sub-saturation level. The liquid drop model is simplistic and does not take into account the change in nuclear density as a function of radius. But the intuition obtained from it holds even for modern nuclear Density Functional Theory (nDFT) models. There is a strong linear correlation between model predictions of neutron skin and symmetry pressure. So, the neutron skin thickness in heavy neutron-rich nuclei puts a constraint on the nDFT models as well. The Pb-208 nucleus is of great interest because in addition to having 44 excess neutrons compared to protons, it is highly stable because of its doubly magic nature, i.e., the outermost neutron and proton shells of the nucleus are

Figure 2.3: Excess neutrons gravitate towards the surface with increased symmetry pressure [Piekarewicz and Fattoyev, 2019]. Reproduced with the permission of American Institute of Physics from J. Piekarewicz and F. J. Fattoyev. Neutron-rich matter in heaven and on earth. Phys. Today, 72(7):30–37, July 2019. The images show that as the model-predicted symmetry pressure increases from 48 MeV to 135 MeV, the central density of neutrons drop and more neutrons gravitate towards higher radius resulting in a thicker neutron skin, i.e., larger difference between the extents of neutron and proton distributions.

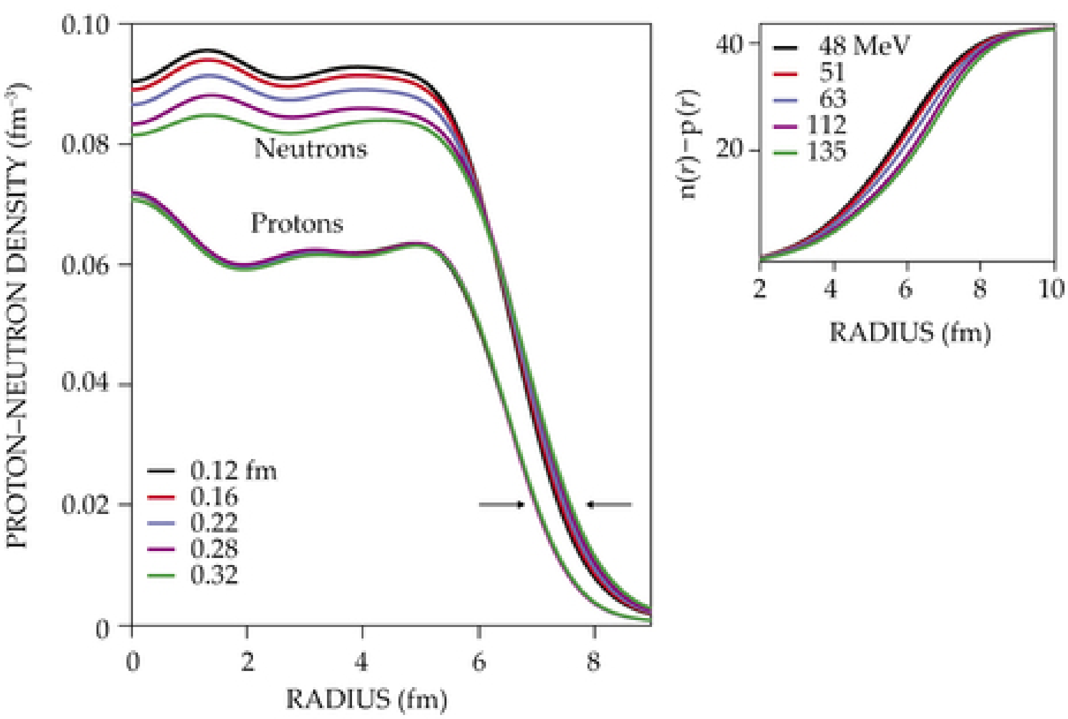

occupied at maximum capacity. PREX-2 measurement of the radius of the neutron distribution of Pb-208 nucleus suffers minimal effect from systemic uncertainties, and model dependence arising from theoretical assumptions compared to other methods such as those using strongly interacting probes, neutrino-nucleus scattering etc.

The neutron and proton density distributions in a nucleus roughly corresponds to

Figure 2.4: Illustration of form factors from various charge distributions. Created based on source image [Povh et al., 2015].

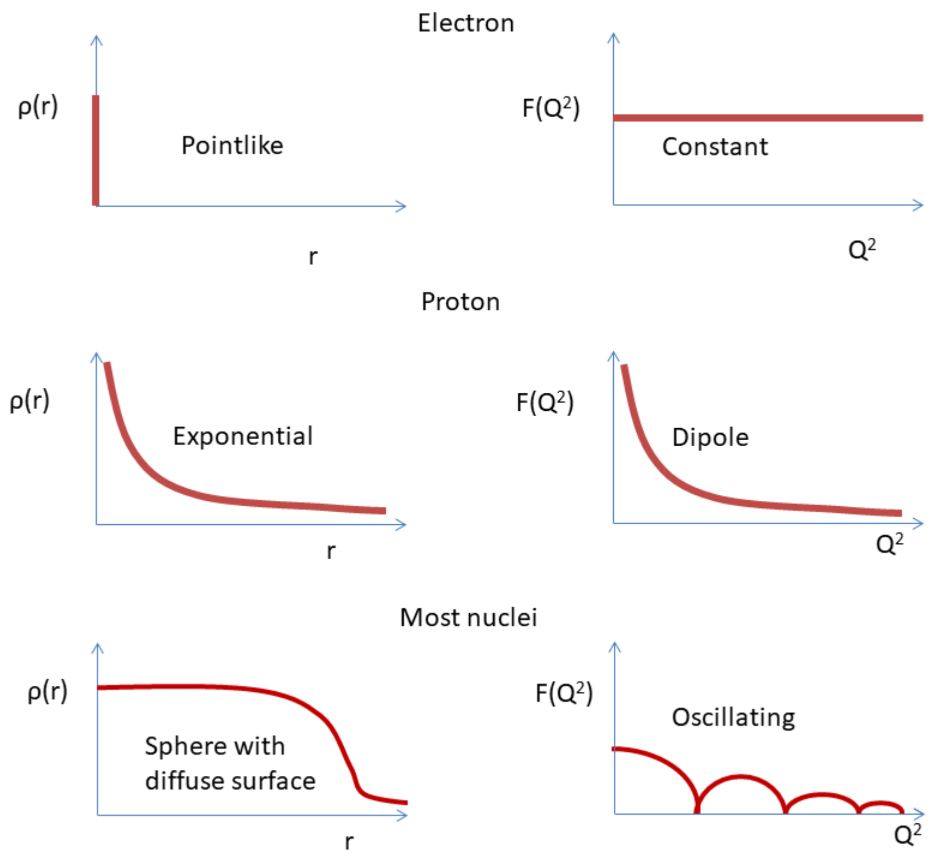

the weak and electromagnetic charge distributions. Experimentally, the electromagnetic charge distribution is probed by measuring the corresponding form factor at different Q^2. The form factor is the ratio of the measured scattering cross-section and the theoretical Mott cross-section describing the scattering of electrons with spin. In the case of elastic electron-nuclei scattering, the form factor can simply be interpreted as the Fourier transform of the charge distribution [Povh et al., 2015]. The figure 2.4 shows the contrast between the form factors of extended nuclei with that of electrons and protons which are not as resolvable with elastic scattering. The PREX-2 asymmetry measurement combined with the electromagnetic form factor measurement give us the the weak form factor value at the chosen kinematics for the experiment [See 1.2]. The weak charge density distribution is extracted using the correlations between model-predicted weak radius/neutron skin and asymmetry [See figure 4.19]. The predicted weak charge densities ($\rho_W(r)$) from a range of relativistic and non-relativistic density functional theories are fitted to a two parameter Fermi function

$$\rho_W(r, c, a) = \rho_W^0 \frac{\sinh\left(\frac{c}{a}\right)}{\cosh\left(\frac{r}{a}\right) + \cosh\left(\frac{c}{a}\right)} \tag{2.7}$$

where ρ_W^0 is a normalization constant, c describes the size of the nucleus while a describes the surface thickness [Paschke et al., 2021]. The c could be identified as the weak charge radius R_W and a as the model uncertainty on R_W. The neutron skin $(R_n - R_p)$ is very close to the difference between the weak charge radius and the electromagnetic charge radius. If the model-predicted weak radius/neutron skin are plotted against the model-predicted asymmetry, the knowledge of the measured asymmetry at the chosen kinematics is sufficient to constrain the above values and underlying models of density distribution.

It is of great interest to link the behavior of neutron rich matter in aggregate to fundamental interactions at the two nucleon and three nucleon level. Figure 2.5 shows the equations of state generated with QMC based on nuclear structure models that take into account only two nucleon (NN) interactions and both two nucleon and three nucleon interactions [Gandolfi and Steiner, 2016]. The red curve corresponds to the Argonne AV8´ NN potential. The black curve corresponds to the addition of the Urbana IX three-body interaction to the Argonne AV8´ NN potential. As it can be seen, the prediction of the symmetry energy at the saturation density ($\rho_0 \sim 0.17$ fm^{-3}) is larger for the black curve (35.1 MeV) compared to the red curve (30.5 MeV). The green and blue bands corresponds to classes of NN+NNN potentials that predict symmetry energies of 32 and 33.7 MeV at the saturation density respectively. There is strong linear relationship between the symmetry pressure and symmetry energy predictions of the models [Gandolfi and Steiner, 2016]. PREX-2 and related CREX

Figure 2.5: Equations of state for various nuclear structure models considering two and three nucleon interactions [Gandolfi and Steiner, 2016]. Reproduced under creative common license 3.0 from S. Gandolfi and A. W. Steiner. Neutron matter, symmetry energy and neutron stars. Journal of Physics: Conference Series, 665:012063, Jan 2016. The colors correspond to different predictions of symmetry energy (30.5, 32, 33.7, and 35.1 respectively) at the saturation density ($\rho_0 \sim 0.17$ fm^{-3}). Inset shows the linear correlation between model predictions of symmetry pressure (L) and symmetry energy (E_{sym}). PREX-2 and related CREX will help determine the EOS near ρ_0 while neutron star mass and radius observations will illuminate the density regimes at multiples of the saturation density, helping us understand the importance of three nucleon interactions in impacting aggregate behavior.

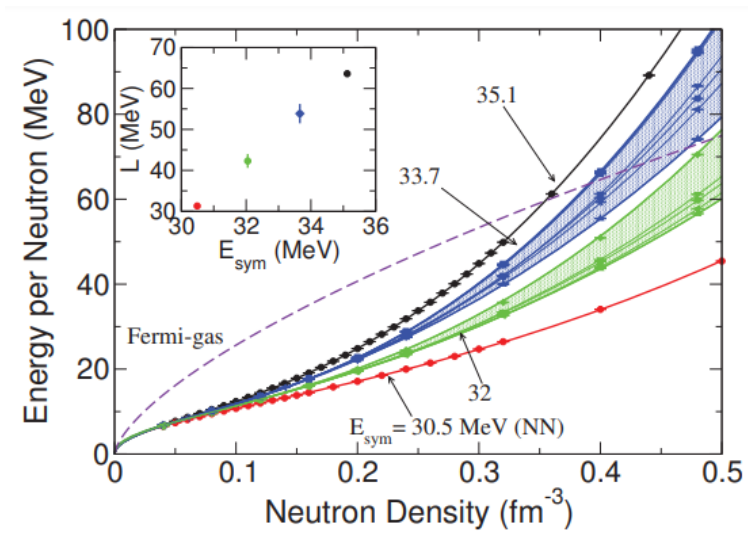

experiment constraints on the symmetry pressure [See figure 1.1] will help to anchor the equations of state near the saturation density. Neutron star mass and radius observations will help illuminate the high density regimes. Already the observation of a neutron star of two solar mass has indicated that just the NN potential is not sufficient to explain EOS behavior in a high density regime [Gandolfi and Steiner, 2016]. So, the PREX-2 and CREX results become very pertinent to understanding the impact of three nucleon interactions on behavior of neutron-rich matter.

2.4 Physics Beyond the Standard Model

The success of the Standard Model is underlined by its remarkable consistency with experimental observations. However, it has many limitations. There are more than 20 free parameters which have to determined through fits to experimental data and cannot be derived from the Standard Model. The Standard Model particles only make up about 4% of the known universe and cannot yet explain dark matter and dark energy whose existence has been confirmed by astronomical observations (ex: the expansion of the universe, discrepancy between optical measurements and gravitational effects, etc.) [Povh et al., 2015]. These issues are accompanied by numerous open questions.

A natural step forward to resolve this problem is to look for new particles and interactions which are collectively termed as Physics Beyond the Standard Model. It is possible to look at past theoretical developments as inspirations in this regard. The electroweak unification theory proposed by Weinberg and Salam postulated that the electromagnetic and the weak interaction were low-energy manifestations of a unified electroweak interaction. The weak isospin (T) quantum number was introduced to explain fermion flavor transformations via the weak interaction with the rule that the third component of weak isospin (T_3) is conserved in the interaction. This lead to the formulation of a weak isospin triplet ($T = 1, T_3 = -1, 0, 1$) and a weak isospin singlet ($T = 0, T_3 = 0$) bosonic state that could mediate the interaction. The coupling strength of the singlet with interacting fermions need not be the same as the coupling strength of the triplet. The W_+ and W_- can be identified as parts of the triplet with $T_3 = 1$ and $T_3 = -1$ respectively. This leaves us with the $W_0(T = 1, T_3 = 0)$ and $B_0(T = 0, T_3 = 0)$ states. The experimentally observed photon (γ) and Z_0, the mediators of the electromagnetic and neutral current weak interactions respectively, are a mixture of W_0 and B_0 states that are orthogonal to each other. This relationship can be expressed as

$$\begin{bmatrix} \gamma_0 \\ Z_0 \end{bmatrix} = \begin{bmatrix} \cos(\theta_W) & \sin(\theta_W) \\ -\sin(\theta_W) & \cos(\theta_W) \end{bmatrix} \begin{bmatrix} B_0 \\ W_0 \end{bmatrix} \tag{2.8}$$

Here, θ_W is the electroweak mixing angle [Povh et al., 2015]. There is a slight caveat. The weak isospin states at the beginning were massless. However, all the weak interaction mediators have mass as per experimental observations. This conundrum was resolved with the introduction of the Higgs Mechanism. It is an example of spontaneous symmetry breaking where the ground state solution to a system does not reflect the symmetry of the original system. A classical example of this would be the planets having elliptical orbits despite the Newton's laws of gravitation having spherical symmetry. With a simple gauge transformation and perturbation about a certain ground state, the electroweak lagrangian can assume a form which makes apparent the existence of scalar fields with 4 degrees of freedom. 3 degrees of freedom are absorbed into the W^+, W^- and Z_0 bosons which gives them mass and the remaining degree of freedom represents the massive Higgs boson [Griffiths, 1987]. On the other hand, the photon (γ) remains massless. Following the success of the electroweak unification, there have been efforts to unify the strong interaction with the electroweak interaction. These theoretical efforts are grouped as Grand Unification Theories (GUTs). The biggest hint that the unification might be possible is the running of the coupling constants as a function of energy scale due to renormalization needed to account for vacuum polarization. So, it can be extrapolated that the coupling constants for electromagnetic, weak and strong interactions will converge to a common value around 10^{15} GeV. Following the example of electroweak unification, it can be postulated that a single interaction, only visible at the high-energy scale, may undergo spontaneous symmetry breaking to produce the three interactions that have been observed observed within our experimental reach so far [Griffiths, 1987]. So, the search for new symmetries and patterns of symmetry-breaking is fundamental to any grand unification scheme and discovery of new physics. I conclude this section with a discussion of a couple of probable candidates for new physics that MOLLER might be sensitive to.

Supersymmetry is one of the notable unification schemes that enables the unification of the matter particles and the force mediators. It can be described as set of continuous transformations in super space-time which is constructed by adding additional anti-commuting coordinates to the space-time coordinates. So, we have the regular space-time symmetries along with new symmetries and consequences. Supersymmetry necessitates that for every particle with spin J, there exists a super particle with heavier mass and spin $J+\frac{1}{2}$ [Gross, 1996]. The mass degeneracy is broken at the Standard Model scale via spontaneous symmetry breaking similar to other situations described earlier, So, Fermions and Bosons are observed as distinct groups of particles. MOLLER will be sensitive to new particles predicted by the Minimal Supersymmetric Standard Model and special scenario such as compressed supersymmetry where the super partners have very similar masses to the regular particles complicating direct detection [Kumar et al., 2020].

MOLLER will have 5 times better precision than E158, the first measurement of the electroweak mixing angle using parity-violating electron scattering. It will be sensitive to TeV-scale neutral Z´ bosons that arise in many Beyond the Standard Model theories [Kumar et al., 2020; Erler et al., 2011]. For example, if the LHC detects a 1.2 TeV Z´, almost complementary regions of the E(6) group model parameter space is ruled out depending on whether the MOLLER result for the electroweak mixing angle agrees with the Standard Model or it lies half away between the E158 measurement and the Standard Model prediction [See figure 2.6]. If MOLLER measures the central value of the E158 at the desired level of improved precision [See figure 1.3], it not only rules out the entire class of Z´ candidates but also Kaluza-Klein candidates from models of extra dimensions. In this particular case, the MOLLER deviation and the LHC signal particle will need independent explanations.

Figure 2.6: 90% confidence level exclusion zones of 1.2 TeV Z´ candidates in the E(6) group for alternate scenarios of the MOLLER measurement. The E(6) group is a probable extension to the Standard Model. Any 3 linearly independent subgroups with U(1) symmetry in the E(6) group can be used to construct a basis for neutral gauge boson (Z´) candidates in this group. It is possible to map such a basis to a sphere, parametrized by two angles α and β [Rojas and Erler, 2015]. The figures below shows the position of various Z´ candidates in a model parameter space with $\alpha \cos \beta$ and β as the horizontal and vertical axes respectively. The colored regions in the figures below show the 90% confidence level exclusion zones in the model parameter space if MOLLER and related experiments agree with the Standard Model (left) vs if the MOLLER measurement of electroweak mixing angle lie half way between E158 central value and the Standard Model prediction (right). Reproduced with permission from author [Kumar et al., 2011].

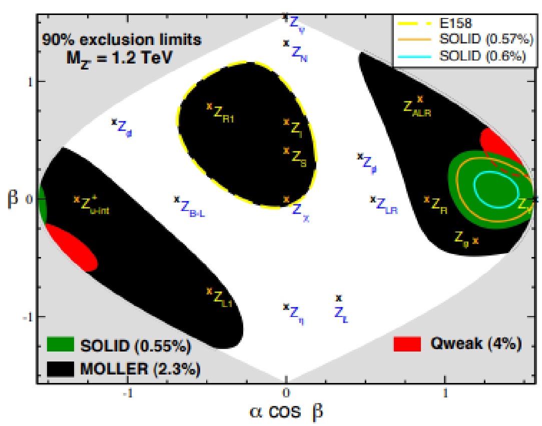

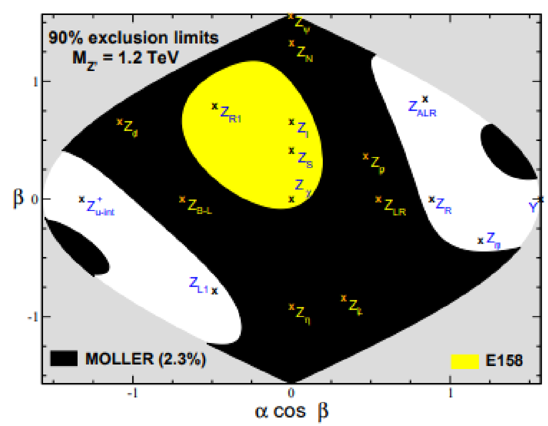

In addition, recently stronger suggestion has emerged for anomalous behavior of muon magnetic moment compared to the Standard Model prediction [Abi et al., 2021]. To explain this, the existence of a light dark boson Z_d has been postulated which arises from the spontaneous breaking of a symmetry in the dark particle sector [Davoudiasl et al., 2012]. The dark Z_d can couple with the ordinary Z boson via kinetic and mass mixing. This may manifest as a shift in the electroweak mixing angle from the Standard Model prediction at low Q^2 [Davoudiasl et al., 2012]. The PREX-2 measurement will allow to improve the precision on weak charge measurement of ^{133}Cs and similar atomic parity violation experiments. MOLLER, along with the results from the weak charge measurements using various methods, will help to achieve more precise determinations of the electroweak mixing angle at low Q^2 and better constraints on the mixing parameters associated with the Z_d, thereby aiding direct searches for such a particle if it exists [Cadeddu et al., 2021].

In the next chapter, I discuss the facility and apparatus that make it possible to perform precision parity-violating experiments like PREX-2 and MOLLER to improve our understanding of nature.

Chapter 3

Facility and Apparatus

In this chapter, I discuss the advanced accelerator technology, precision beam control, and enhanced monitoring capabilities available at the Thomas Jefferson National Accelerator Facility that makes it an ideal location to conduct parity-violating electron scattering experiments like PREX-2 and MOLLER. I also discuss the specific apparatus for the two experiments.

3.1 The Continuous Electron Beam Accelerator Facility

The Continuous Electron Beam Accelerator Facility (CEBAF) is located at the Thomas Jefferson National Laboratory in Newport News, Virginia, USA. The accelerator delivered its first electron beam in 1994 and reached its design goal of supplying 4 GeV electron beam in 1998. However, design efficiency and operational experience made it possible to deliver 6 GeV electron beam by the end of 2000 [Rode, 2010]. The 12 GeV upgrade, completed in 2017, further improved the accelerator in terms science capabilities. There are 4 experimental halls (hall A, hall B, hall C, and hall D) in the facility which are dedicated to a range of particle and nuclear physics experiments exploiting the strong and weak interactions [Jefferson Lab Communications Office, 2017].

Figure 3.1: Overview of the Continuous Electron Beam Accelerator Facility (CEBAF) at the Thomas Jefferson National Laboratory, Newport News, Virginia, USA [Rode, 2010; Gal, 2020]. Reprinted with the full permission of AIP publishing from C. H. Rode. Jefferson Lab 12 GeV CEBAF upgrade. AIP Conf. Proc., 1218(1):26–33, Apr. 2010.

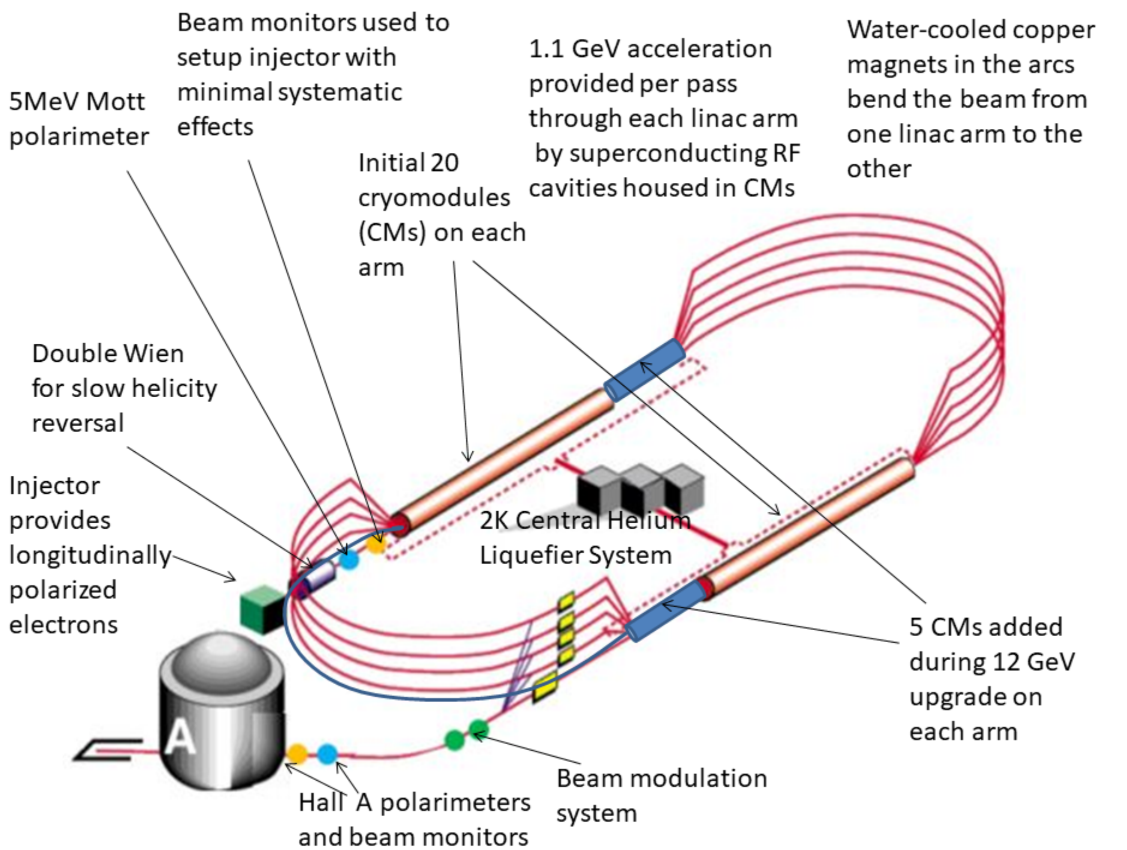

As shown in figure 3.1, the polarized electron beam is produced in the injector region and then accelerated by superconducting radiofrequency (RF) cavities housed in cryomodules (CMs) on the two arms of the linear accelerator. Cooling for the CMs is handled by the 2 K central helium liquefier system. The beam gains 1.1 GeV energy per pass through each arm and transition from one arm to the other is handled by traditional water-cooled copper magnets in the arcs. A series of polarimeters and sensors are distributed along the beamline to monitor beam quality. The unique features of the CEBAF, such as, high degree of polarization and high intensity of delivered beam, precision beam control, and improved infrastructure made it an ideal location to conduct parity-violating electron scattering experiments such as PREX-2 and MOLLER. PREX-2 used the existing setup in hall A involving the high-resolution spectrometers and detector huts, symmetrically positioned to capture electrons scattered at ~ 5 degrees [Gal, 2020]. A new setup will be installed for MOLLER with a state-of-the-art spectrometer and detector array design with full azimuthal coverage in scattering angle [Kumar et al., 2020]. The rest of section 3.1 discusses the important components of the CEBAF facility. The details of the PREX-2 and MOLLER apparatus are provided in section 3.2 and 3.3 respectively.

The source of the polarized electron beam at CEBAF is referred to as the injector. As shown in figure 3.2, the main components of the injector setup during PREX-2 were a laser of wavelength $780 - 850$ nm, a linear polarizer, a Rubidium Titanyl Phosphate (RTP) pockels cell, an insertable half wave plate (IHWP), a rotating half wave plate, a GaAs photocathode, and a double Wien configuration [Palatchi, 2019; Gal, 2020]. Light from the $780 - 850$ nm laser was linearly polarized and then passed through the RTP pockels cell. The pockels cell received a randomized helicity signal and converted the linearly polarized light into circularly polarized light of opposite helicities based on the sign of the input signal state. An insertable half wave plate (IHWP) was used for slow helicity reversals by flipping the laser polarization occasionally to suppress helicity-correlated beam asymmetries. A rotating half wave plate (RHWP) after the pockels cell was used to run scans to align the pockels cell and understand the systematic effects of vacuum window birefringence, position differences and steering with the laser setup. The laser was then impinged on a Gallium Arsenide (GaAs) photocathode which emitted longitudinally polarized electrons with

Figure 3.2: A schematic of the injector setup during PREX-2 that provided the longitudinally polarized electron beam. Created based on source image [Palatchi, 2019; Gal, 2020].

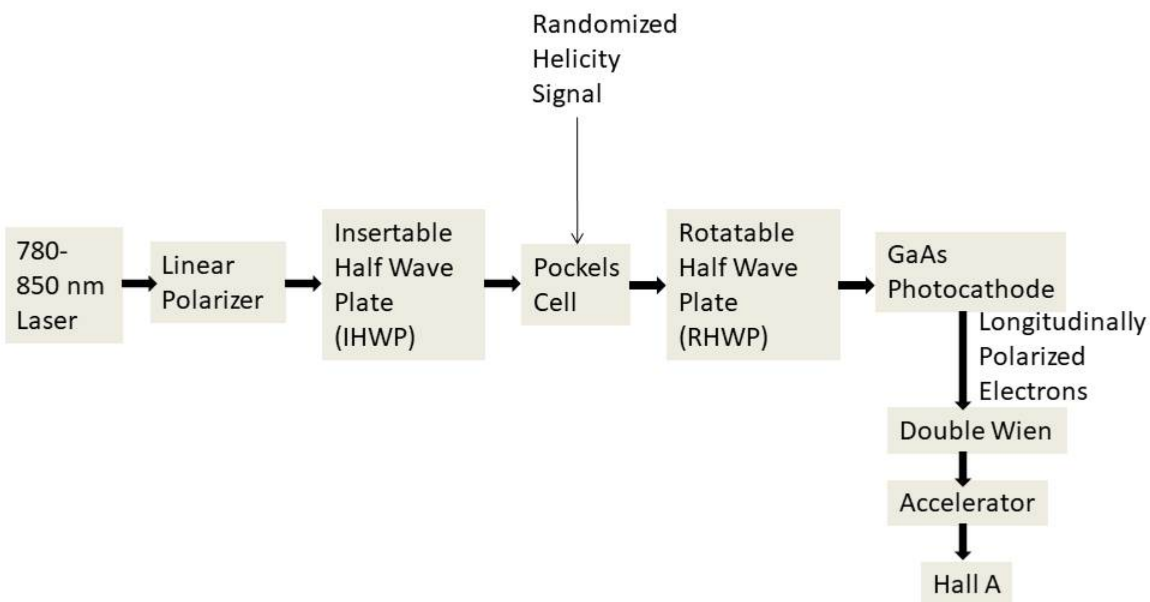

the same helicity as the incoming photons. A double Wien filter configuration along with two separated solenoidal magnets in between was used to perform slow helicity reversals of the electron beam independent of the laser state to further suppress systematic effects. Improvements in the injector (RTP design with better control, high degree of polarization achievable in theory, etc.) was vital for achieving parity-quality beam at the target in the experimental hall. The experiences from PREX-2 and past experiments demonstrate that these improvements coupled with charge and position feedback, slow helicity reversals, adiabatic damping in the accelerator, and incoherent synchrotron light emittance growth could help achieve the levels of intensity, energy, position, angle, and spot size differences acceptable for MOLLER [Palatchi, 2019].

To minimize false asymmetries in a parity-violating electron scattering experiment, the various properties of the beam need to be measured continuously. The current monitoring system for hall A features an Unser monitor and two RF cavity monitors. This enables a highly accurate current measurement in a non-invasive manner over a large range. Although the gain of the Unser to the beam current is stable (~ 4 mV/μA), magnetic environment and temperature fluctuations can result in a time-dependent zero-offset in the order of μA. So, the Unser cannot be used for continuous measurements and is only used for calibrating the cavity monitors in hall A. The Unser itself is cross-calibrated against a cavity monitor and a Faraday cup in the injector region [Higinbotham et al., 2017]. There are two cavity monitors upstream and downstream respectively of the Unser. These are cylindrical wave guides made of stainless steel. There is minimal beam energy loss in the monitors because of their high quality factor. In addition, the monitors have a proportional response to the beam current because they are tuned to the beam frequency (1497 MHz) [Higinbotham et al., 2017].

The beam position is measured with a series of stripline and cavity beam position monitors (BPMs) with high precision. The beam energy is measured with the help of eight dipole magnets in the arc leading into hall A, invasive harp scanners, and non-invasive beam position monitors along the beam line [Liu, 2020].

Small angle monitors (SAMs) along the beam line are sensitive to variations in target condition, beam fluctuations, and electronics noise. Since the parity-violating asymmetry is very small at the highly forward angles, SAMs act as null asymmetry monitors [Kumar et al., 2020].

The beam modulation system is needed to correct out helicity-correlated beam asymmetries from the measured asymmetry. It consists of a set of 6 air-core dipoles and an energy vernier in the arc leading from the beamline into hall A [Owen, 2020].

The response from the modulation is recorded by the beamline sensors so that the systematic effect of the beam parameter fluctuations can be quantified.

The systemic uncertainty in asymmetry measurement in parity-violating experiments can be suppressed by measuring the beam polarization with high precision. One of the major corrections involved in calculating the final asymmetry is dividing the raw measured asymmetry by the beam polarization. So, the error in this correction term adds in quadrature with other uncertainties for the asymmetry measurement. Since the asymmetry is directly connected to measurable quantities such as the weak form factor (F_W) [equation 1.2] and $\sin^2\theta_W$ [equation 1.3 and 1.4] for PREX-2 and MOLLER, it is very important to control the systematic uncertainties associated with the polarization measurement to below 1% of the asymmetry. I discuss the different systems that are used to measure the degree of beam polarizations for experiments with high accuracy in hall A:

- The Mott polarimeter: The Mott polarimeter is used to measure the spin polarization of the electron beam when it leaves the injector region. The polarimeter has its own target, collimation and detector system enclosed within a stainless steel chamber that is connected to the beam line but isolated by a metal valve. A 12.5 degree dipole bend magnet is used to guide the beam into the chamber during measurements. The polarimeter measures the counting rate asymmetry in elastic Mott scattering of beam electrons from nuclei in target metallic foils. The asymmetry is non-zero when the direction of beam polarization is not parallel to the scattering plane. The Sherman function is used to determine the degree of beam polarization based on the measured asymmetry and is subjected to theoretical uncertainty. The accuracy of the measurement also depends on the purity of the spectra (free of contribution from Al windows in the chamber) and the extrapolation of results from finite thickness foil to single nucleus case. The measurement has a systematic uncertainty of 1.1% [Steigerwald, 2001]. The hall polarization measurements can be compared against the

Mott measurement to check for any discrepancies which might indicate loss of beam polarization in transit.

- The Møller polarimeter: The hall A Møller polarimeter measures the beam polarization in the experimental hall by measuring the longitudinal analyzing power when the electron beam is scattered from a polarized iron foil. The scattering cross section (σ) is given by [JLAB Hall A Møller Polarimeter Group, 2019]

$$\sigma \propto 1 + \sum_{i=x,y,z} \left(A_{ii} P_i^{targ} P_i^{beam} \right) \tag{3.1}$$

where $A_{xx/yy}$ and A_{zz} are the transverse and longitudinal analyzing powers respectively assuming that the z-axis is aligned with beam propagation direction, P_i^{targ} is the degree of polarization of the target, and P_i^{beam} is the degree of polarization of the beam. The target foil is placed perpendicular to the beam axis and it is magnetized by a 3 T field along the direction of the beam during measurements. The maximal polarization achievable for the target iron foil is 8.01%. The scattered electron pairs emerging after the Møller scattering are passed through a spectrometer magnet system consisting of four quadrupole magnets and a dipole magnet. The spectrometer system defines the kinematic range of acceptance for the electrons along with a collimator and guides them into a two-arm detector system. Then the coincident events on the two detectors can then be recognized as Møller scattered electrons. The beam polarization is extracted using the following equation [JLAB Hall A Møller Polarimeter Group, 2019]

$$P_z^{beam} = \frac{N_+ - N_-}{N_+ + N_-} \cdot \frac{1}{P^{foil} \langle A_{zz} \rangle} \tag{3.2}$$

where N_+ and N_- are measured counting rates with the beam and target polarizations aligned and anti-aligned respectively, the average analyzing power

$< A_{zz} >$ is obtained by using Monte-Carlo simulation, and the foil polarization P^{foil} is derived from measurements of magnetization in bulk material. Møller polarimetry is invasive so it was conducted every two weeks or so.

- The Compton polarimeter: The Compton polarimeter is used to make continuous measurement of beam polarization during the experiment as a cross-check for the discrete Møller measurements. The polarimeter uses Compton interaction of a laser beam with known circular polarization with the incoming polarized electron beam. The continuous measurement is possible because Compton scattering has very low cross-section, making the process fairly non-invasive [Kiadtisak, 2013]. In the Compton system, a laser beam of wavelength 1064 nm is produced after amplification by a seed laser and then doubled to wavelength 582 nm by a Periodically Poled Lithium Niobate (PPLN) crystal. The laser is locked to the Fabry-Perot cavity to achieve ~kW level of power. A set of 4 dipole magnets are used to tune the beam through the laser cavity and then back into the main beamline. When there is an interaction between a laser photon and an electron, the scattered photon is captured by a photon calorimeter composed of a single Gadolinium Orthosilicate (GSO) crystal and the scattered electron is captured by silicon strip detector [Zec, 2020]. The polarization is measured by calculating the asymmetry between the energy-weighted integrated signal when the beam and laser polarizations are aligned and anti-aligned respectively. So,

$$P_z^{beam} = \frac{S_+ - S_-}{S_+ + S_-} \cdot \frac{1}{P_\gamma \langle A_S \rangle} \tag{3.3}$$

where $S_{+/-}$ are the integrated signals for aligned and anti-aligned electron beam and laser polarizations respectively, P_γ is the photon polarization and $< A_s >$ is the average analyzing power over acceptance determined by Monte-Carlo simulation [Kiadtisak, 2013]. The photon detector was mainly used for polarization measurement during PREX-2 as the electron detector system was under development. Both systems are expected to be operational during MOLLER.

3.2 PREX-2 Apparatus

In this section, I discuss the apparatus specific to the PREX-2 experiment that were constructed inside hall A of Jefferson Lab. The most important systems such as the target, spectrometer, tracking, and main detector system are discussed. The electrons after scattering elastically at the target at 5 degrees scattering angle were guided through high resolution spectrometer (HRS) systems on symmetrically positioned arms before reaching the main detectors. Particle tracking was performed using vertical drift chambers (VDCs) on both arms. Figure 3.3 shows the side view of one of the arms of the experimental apparatus.

Figure 3.3: PREX-2 apparatus side view with schematic highlighting major components. The scattered electrons from the target are bent by septum magnets and then focused by two high-resolution spectrometers (HRS) onto the tracking VDCs and the Quartz Cherenkov main detectors. Each HRS consists of 3 quadrupole magnets (labelled as $Q1$, $Q2$ and $Q3$) and a dipole magnet. Reprinted with permission from author [Gal, 2020].

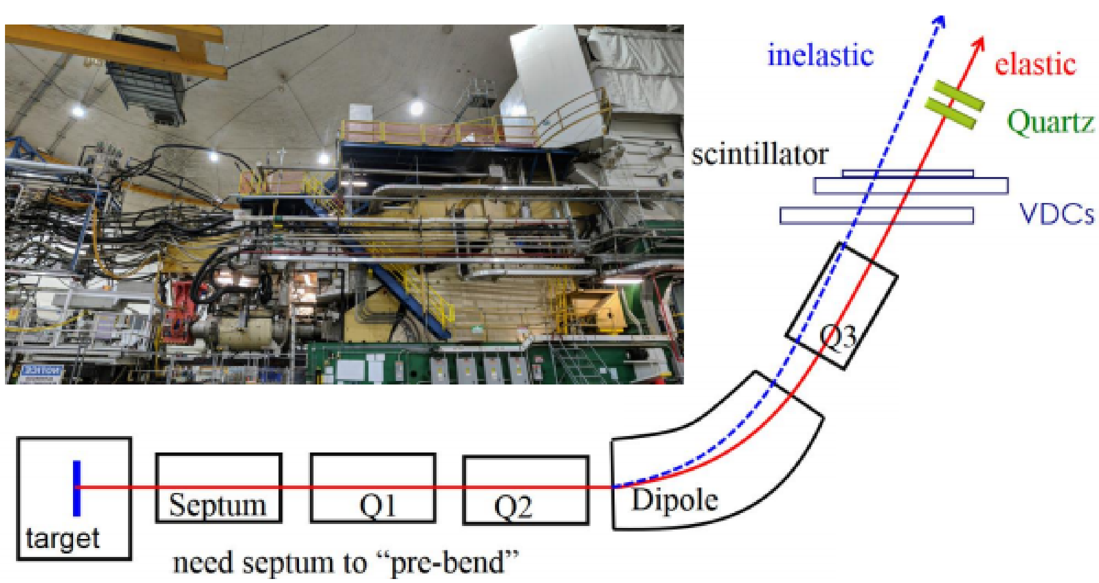

3.2.1 Target System

Figure 3.4: Target system for PREX-2. Reprinted with permission from author [Clarke, 2020b]. Two target ladders were used: one for physics measurement and the other for optics calibration. The main asymmetry measurements were conducted with 7 of the D-^{208}Pb-D sandwiches on the physics ladder. The pointing measurement for Q^2 determination used the water cell on the optics ladder [PREX Collaboration, 2017].

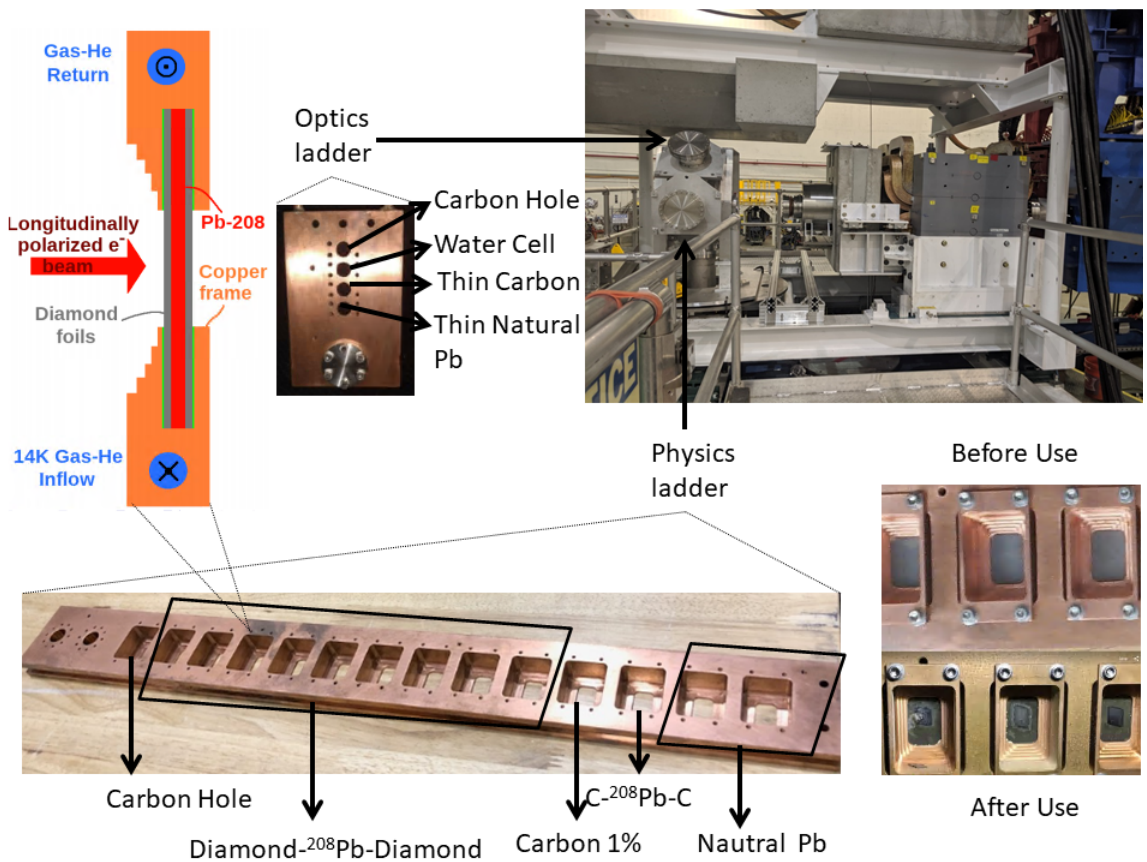

The PREX-2 target chamber was made of Aluminum. The main portion of the chamber was 33 cm long with 60.96 cm diameter. In addition, there was a neck on the downstream side, 9 cm long with 15 cm diameter [Dusa, 2018]. A vacuum of 10^{-5} Torr was maintained inside the chamber. Radiation hard metal seals were used to secure the vacuum environment [PREX Collaboration, 2017]. The target chamber had two target ladders: one for physics measurement and the other for optics calibration [See figure 3.4]. The physics ladder needed to be cooled with circulating 14 K helium gas. The main asymmetry measurements were conducted with the targets which each had a ~ 0.5 mm thick piece of ^{208}Pb sandwiched between two ~ 0.25 mm diamond foils [PREX Collaboration, 2017]. The thicknesses of ^{208}Pb and diamond were measured in terms of radiation lengths to better than 5% accuracy to be 625 mg/cm^2 and 90 mg/cm^2 respectively [Paschke et al., 2021]. Mitigatory steps were taken to improve the resistance of the D-^{208}Pb-D sandwiches to thermal effects and a 4×6 mm^2 raster was used to distribute the heat load around the target surface [Clarke, 2020b]. However, they still had to be switched from time to time after prolonged beam exposure. In total 7 of these targets were used during the entire experiment. Usually after $17 - 22$ Coulomb charge were collected during the experiment at 70 μA running, the target had to be switched out [Clarke, 2020b]. On the optics ladder, the main target of interest was the water cell target which was used for pointing measurements relevant to Q^2 determination. The water cell had 5 mm of water between 0.05 mm of steel windows [PREX Collaboration, 2017]. The water cell target did not require cryogenic cooling. Apart from the above mentioned targets, the other targets were used for various systematic studies and calibration.

3.2.2 Spectrometer System

PREX-2 used the two existing high resolution spectrometer (HRS) magnet assemblies on two arms in hall A. Each HRS has a 45 degree vertically upward bending QQD_nQ design with 3 cryogenically cooled superconducting quadrupole magnets ($Q1$, $Q2$, and $Q3$) and a dipole magnet D_n with field gradient $n = -1.25$. Each HRS has a high momentum resolution of 1×10^{-4} over a scattered momentum range of $\sim 0.8 - 4$ GeV. Each HRS has a angular resolution of 0.5 mrad in the horizontal direction and 1.0 mrad in the vertical direction over a scattered angular range of $\sim 12.5 - 130$

Figure 3.5: Sieve slit collimators before septum magnet and acceptance defining collimators before HRS $Q1$ quadrupole region. The sieve slit collimators were used for optics calibration purposes and the $Q1$ collimators defined the experimental kinematics.

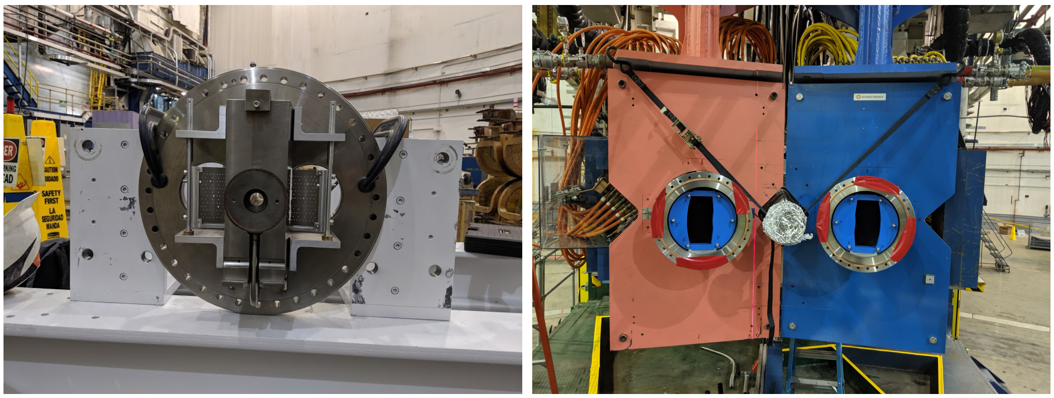

degrees on both arms [J. Alcorn et al., 2004]. Note that for PREX-2, only electrons elastically scattered at ~ 5 degrees needed to be selected which is below the lower limit of the angular range. This was achieved by using the septum magnet in between the target chamber and the $Q1$ region to pre-bend electron elastically scattered at ~ 5 degrees into the $Q1$ region. As shown in figure 3.5, there was a stainless steel sieve slit collimator in front of the septum magnet for optics calibration purposes and an 8 cm thick Tungsten acceptance-defining collimator near the entrance to $Q1$ quadrupole which determined the kinematics of the experiment [PREX Collaboration, 2017]. For each HRS, the $Q1$ quadrupole and the dipole magnet provided the radial focusing. On the other hand, the $Q2$ and $Q3$ quadrupoles provided the azimuthal focusing [J. Alcorn et al., 2004].

3.2.3 Tracking System

On each arm, two vertical drift chambers (VDCs) were placed between the end of the HRS and the main detector system as shown in figure 3.3. Figure 3.6 shows that the VDCs were parallel to the hall horizontal plane. They were at a 45 degree

Figure 3.6: Schematic of the pair of tracking vertical drift chambers (VDCs) on each apparatus arm. Created based on source image [Fissum et al., 2001]. The VDCs were parallel to the hall horizontal plane, and at a 45 degree angle to the nominal particle trajectory and the plane enclosing dispersive (x) and non-dispersive directions (y). Each VDC had two grounded planes of sense wires that crossed at 90 degrees angle and three high-voltage (HV) planes in a chamber filled with gaseous mixture of argon and ethane. Any energetic particle passing through a VDC caused ionization creating free electrons at various locations along the trajectory. Using the drift velocity and time of flight information of these electrons to the sense wires, unique position coordinates were obtained on each wire plane of the two VDCs to reconstruct the trajectory.

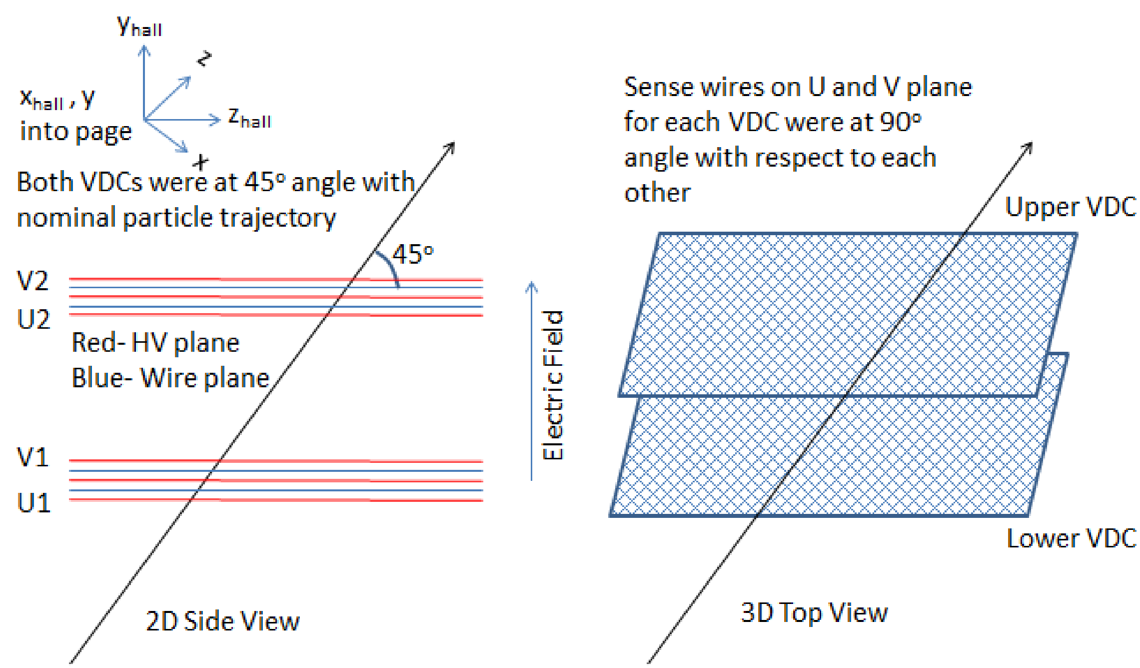

angle to the nominal particle trajectory, and the plane enclosing dispersive (x) and non-dispersive directions (y). Each VDC had two grounded orthogonal wire planes with two single sided HV planes on either extremes and a double sided HV plane in the middle. The setup produced a 3 kV/cm field everywhere in each VDC except the region close to the wire plane sense wires where the field increased by $\frac{1}{r}$ with decreasing distance r [Fissum et al., 2001]. Each VDC was filled with a gaseous mixture of argon (62%) and ethane (38%). Electrons, produced due to the ionization of the gas when a particle passed through each VDC, traveled towards the sense wires with a drift velocity along the path of least time as the acceleration from electric field was canceled out by drag. Avalanche reactions caused by the electrons in the amplified field close to the wires produced detectable currents. Using the electron drift time and velocity information from both VDCs, the particle track could be reconstructed [Fissum et al., 2001].

Figure 3.7: Strong correlation between GEM and VDC reconstructed position variables θ and ϕ. A VDC on each HRS arm was used for particle tracking during optics calibration for PREX-2. Auxiliary measurements were performed with Gas Electron Multiplier (GEM) detectors to test their feasibility. The measurements showed strong correlation and strengthens the case for using GEMs for MOLLER. GEMs can handle a higher signal rate compare to VDCs [Ghosh, 2020].

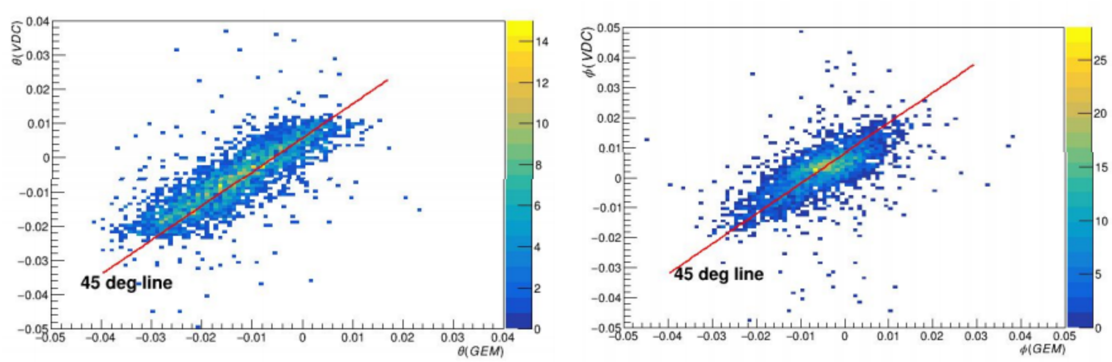

The VDCs were only used during counting mode measurements for optics calibration and Q^2 measurements at low current since their efficiency dropped increasingly with event rate and the operational limit was a rate of 10 kHz/cm^2 [Ghosh, 2020].The trigger for the VDC was provided by a scintillator placed right above the upper VDC as shown in figure 3.8. Although the operational limit for event rate was sufficient for the PREX-2 experiment, a functioning tracking system that can operate in a high rate environment is needed looking forward to MOLLER. During PREX-2, the VDCs were complemented by an auxiliary gas electron multiplier (GEM) tracking system which could handle up to $\sim$ 1 MHz/cm^2 [Ghosh, 2020]. Although the GEM data were not used for the Q^2 measurement, they showed promise in track reconstruction similar to the VDCs as shown in figure 3.7.

3.2.4 Main Detector System

Figure 3.8: PREX-2 detector system side (left) and top (right) view. The red line shows the approximate path of the scattered electrons passing through the positions of the tracking VDCs and trigger scintillators, the main Quartz Cherenkov detectors, and the auxiliary detectors and GEMs.

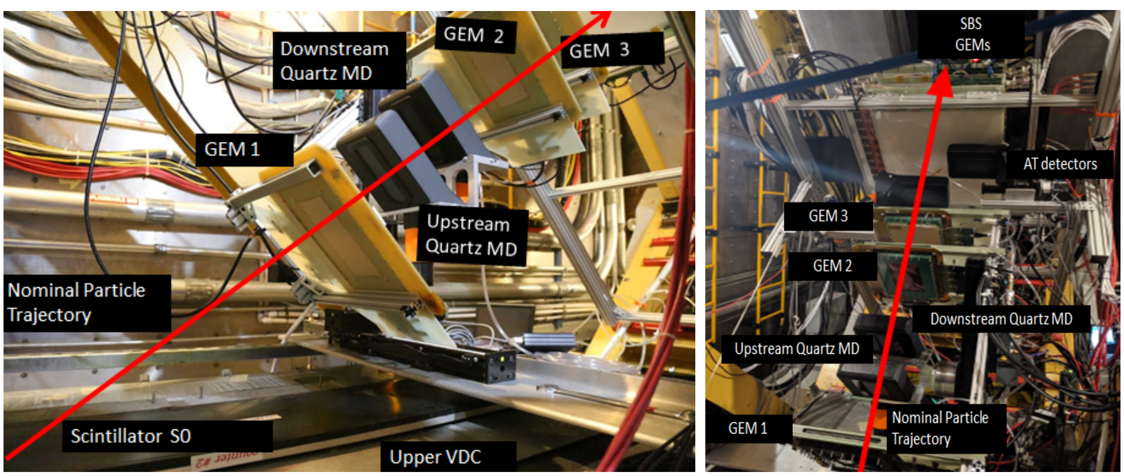

As shown in figure 3.8, the main detector (MD) system for PREX-2 consisted of two detectors on each arm of the spectrometer. The data used for analysis were collected with the upstream detectors and the downstream detectors were used for consistency checks. On each arm, the scattered electron beam was focused on the part of the detector that was made of 16 cm $\times$ 3.5 cm $\times$ 0.5 cm piece of radiation-hard quartz (Spectrosil 2000 fused-silica). The detectors on each arm experienced about

2.2 GHz rate at the nominal 70 μA beam current for the experiment [Adhikari, 2020a]. The Cherenkov radiation, emitted when an electron passed through the quartz of a detector, underwent total internal reflection inside the quartz and was captured by a PMT with 2 inch window. The quartz plane was setup to be perpendicular to the scattered electron direction to capture the entirety of the Cherenkov cone and reduce sensitivity to δ-rays.

Figure 3.9: Scattered electron distribution along the dispersive direction on the detector plane as projected by the VDCs. The scattered electrons were focused by each HRS in a way that the elastic peak was centered on the main detectors on each arm along the dispersive direction (the dispersive direction is labeled as the x-axis). The figure below shows that the VDC-projected elastic peak was indeed centered on the main detectors and the excited states were incident on a region beyond the physical edge of the main detectors along the dispersive direction. Reprinted with permission of author [Adhikari, 2020a].

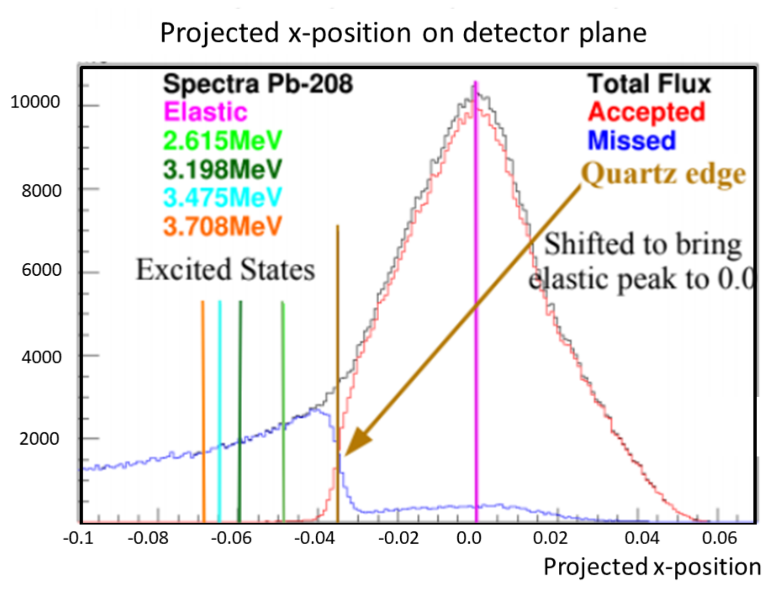

The design was optimized to maximize light yield and resolution since those properties effect the width of the asymmetry,

$$\sigma_{A_{PV}} = \frac{\sigma_{meas}}{\sqrt{1+\Delta_{Det}^2}} \tag{3.4}$$

where $\sigma_{meas} = \sqrt{\sigma_{reg}^2 - \Delta_{BPM}^2 - \Delta_{BCM}^2}$, σ_{reg} is the regressed asymmetry width and $\Delta_i = \frac{RMS_i}{mean_i}$ are equipment resolutions [Adhikari, 2020a]. The pedestal subtracted mean photoelectron yield for the detectors were 28 photoelectrons[Adhikari, 2020a]. The detectors were positioned so that only the events in the elastic peak of the scattered momentum distribution were accepted. An example projected distribution of the scattered particles along the dispersive direction on one of the quartz detectors is shown in figure 3.9. There were also a set of auxiliary transverse (AT) detectors further downstream of the two main detectors to monitor the false asymmetry due to residual polarization of the electron beam in a direction perpendicular to the scattering plane [Adhikari, 2020a]. The AT detectors had the same exact dimensions as the main detectors but they had different geometric acceptance.

3.2.5 Other Systems

PREX-2 had two independent data acquisition systems (DAQs): the parity DAQ and the counting-mode DAQ [Michaels, 2018]. Both DAQs were designed based on a software and hardware framework known as the CEBAF On-line Data Acquisition System (CODA) [JLAB Data Acquisition Group, 2017]. Each DAQ system uses a unique trigger supervisor to communicate back-and-forth with the front-end hardware. The two DAQ uses separate run control processes as well. In each case, data is gathered by the read out controllers (ROCs) and sent out to the event recorder which writes it to tape. The CODA output from the counting DAQ is analyzed by the hall A analyzer and the output from the parity DAQ is analyzed by a software framework called JAPAN (Just Another Parity Analyzer) developed by the PREX-2 collaboration.

Figure 3.10: Side view of the PREX-2 shielding. PREX-2 used a combination of concrete and High Density Polyethylene (HDPE) blocks to shield sensitive equipment from radiation and also to keep the overall radiation level in the experimental hall low. Reprinted with permission from author [PREX Collaboration, 2017].

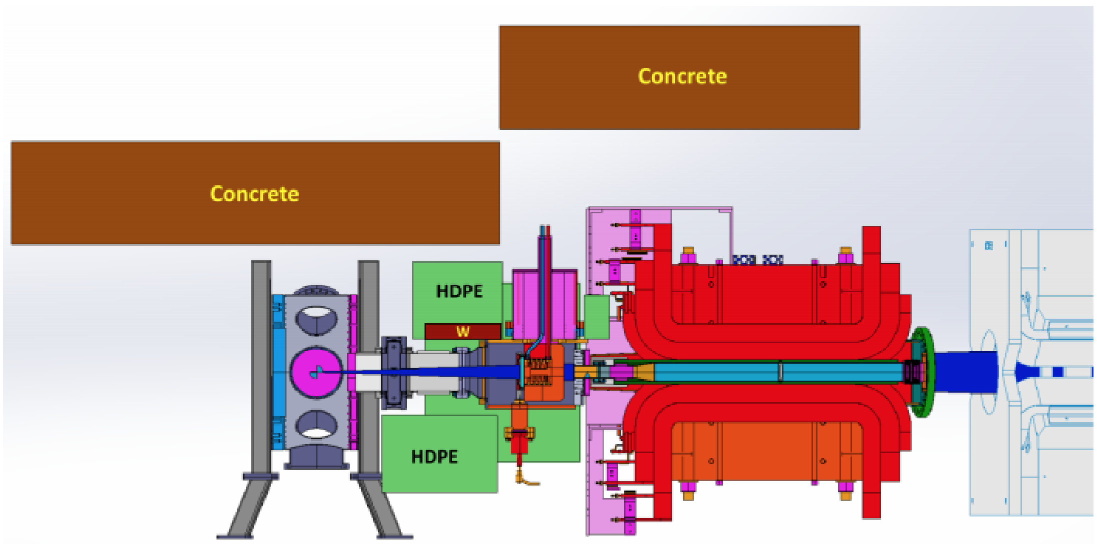

In terms of shielding, PREX-2 had a 6 cm thick tungsten block weighing 160 kg just upstream of the acceptance defining collimator face to stop high energy neutrons ($>$ 30 MeV) originating out of the beamline collimator that was used to keep the central beam from spreading out [PREX Collaboration, 2017]. There were two 40 cm thick concrete blocks weighing 2800 and 2700 kg respectively above the target and the collimator region to further attenuate the high energy neutrons. The extent of these above blocks are shown in figure 3.10. Together the two blocks attenuate 55% of the high energy neutron power reaching the roof of the whole and 40% of the total high energy neutron power [PREX Collaboration, 2017]. This helped to keep the shower from the power escaping through the hall boundary below the lab limit of 10 mrem/yr. There were also HDPE plastic blocks all around the collimator region to attenuate moderate energy neutrons which would be the primary cause of damages to electronics [PREX Collaboration, 2017].

In the next section, I discuss the MOLLER apparatus which has a vastly different design but employing similar basic principles.

3.3 MOLLER Apparatus

Figure 3.11: An overview of the MOLLER experimental apparatus. The main components are the liquid Hydrogen target, the collimators, the two toroidal spectrometer magnet assemblies, the tracking detector system, and the main detector system. Reprinted with permission from author [Kumar et al., 2020].

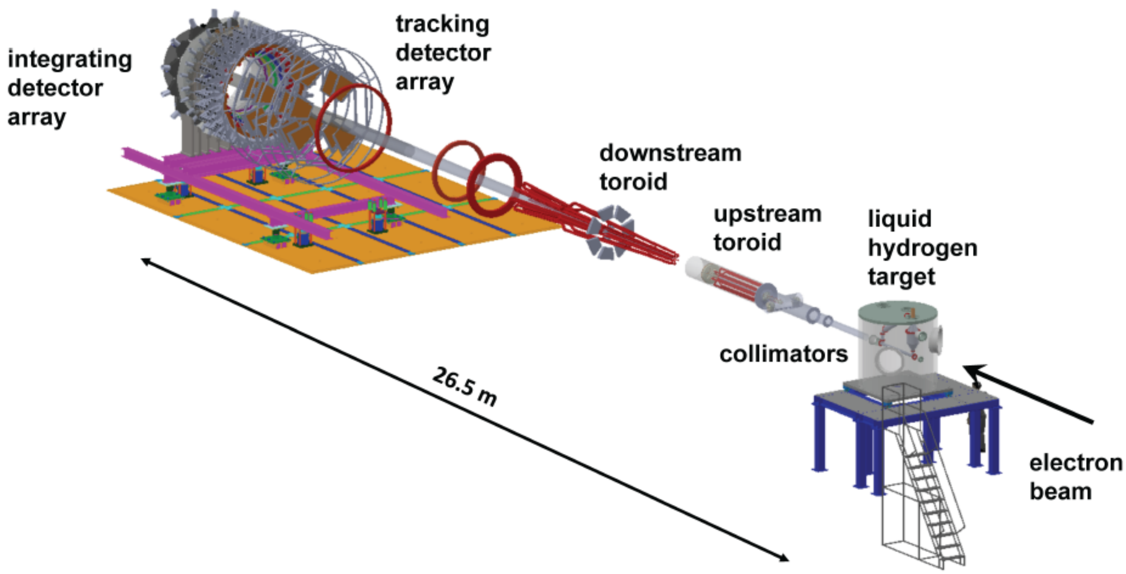

In this section, the conceptual design of various MOLLER subsystems as shown in figure 3.11 are discussed. In the experiment, the electrons in a longitudinally polarized electron beam will be scattered from atomic electrons in an unpolarized liquid Hydrogen target before being guided through a spectrometer system consisting of collimators and two toroidal magnets to a main detector array consisting of 224 quartz Cherenkov detectors. There will also be an auxiliary tungsten-quartz shower max detector system to measure the main Møller (electron-electron scattering) signal. A system of GEM detectors and an acrylic Cherenkov detector array will be used for tracking purposes.

3.3.1 Target System

Figure 3.12: A schematic diagram of the MOLLER target system. Reprinted with permission from author [Kumar et al., 2020]. The liquid hydrogen (LH2) cell will be used for the main measurement. There will be several thin targets to perform optics calibration and establish experimental kinematics. There will be a pair of thin targets with holes to check beam-target alignment. There will be several high power targets to benchmark radiative effects in simulation to correctly predict event rates and measure aluminum (Al) backgrounds from the target can.

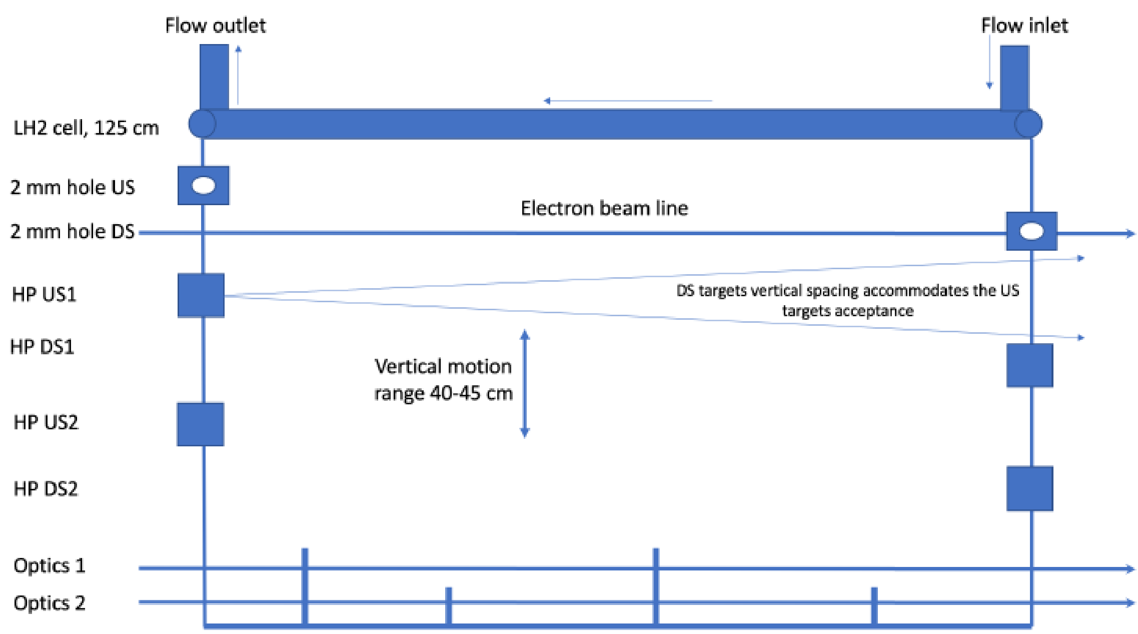

As shown in figure 3.12, the main target for MOLLER is a 125 cm long aluminum (Al) cell filled with liquid hydrogen(LH2). The LH2 target is designed to be dense enough (9g/cm^2) to produce the required luminosity at the operating current of 65 uA and still handle a power load of $\sim$ 4 kW which is a substantial improvement for a target of this size based on previous experimental precedents [Kumar et al., 2020]. The target cell is connected in a loop with a LH2 pump, a heat exchanger and a high power heater. The loop itself is part of a constant volume system which has it connected via gas panels with storage tanks outside hall A containing buffer hydrogen gas. The target is enclosed in a vacuum chamber with a motion system at the top that allows vertical motion in a range of 45 cm. Target boiling due to heating can result in loss of luminosity. Density fluctuations at the helicity flip rate time scale can also be a source of systematic error [Kumar et al., 2020]. The other components in the target loop act in concert to mitigate these issues. The high power heater is used in a closed feedback loop with the beam on the target to maintain a constant heat load on the target. The heat exchanger helps to cool the target by transferring heat from the hydrogen in the target loop to liquid helium from a end station refrigerator. Finally, the pump helps to continuously move the hydrogen through the target loop and helps to prevent the LH2 from boiling due to prolonged beam exposure. The density fluctuation effect is minimized by optimizing the target fluid condition and beam properties such as raster size and intensity. The target motion system also incorporates other solid targets that are used for optics calibration, determining experimental kinematics, beam-target alignment, raster size calibration, benchmarking of radiative effects in simulation, and measuring backgrounds from target Al can [Kumar et al., 2020]. The cold targets are operated at lower current (level of few nA to few μA). There is also a free slot for beam tuning.

3.3.2 Spectrometer System

Figure 3.13: Principle behind full azimuthal coverage by MOLLER acceptance defining collimator with odd number of holes. Reprinted with permission from author [Kumar et al., 2020]. The two plots on the left show the correlation between lab scattering angle and scattered electron energy and the correlation between scattered electron energy and center-of-mass scattering angle. Since Møller scattering is an identical particle scattering process, a collimator design with seven-fold symmetry ensures that the forward and backward scattering partners end up in open and closed sectors 180 degrees apart at different radii. Since the closed sector is blocked off at the acceptance defining collimator to protect the spectrometer magnet coils in the shadow, this helps to prevent double counting and still achieve full azimuthal coverage.

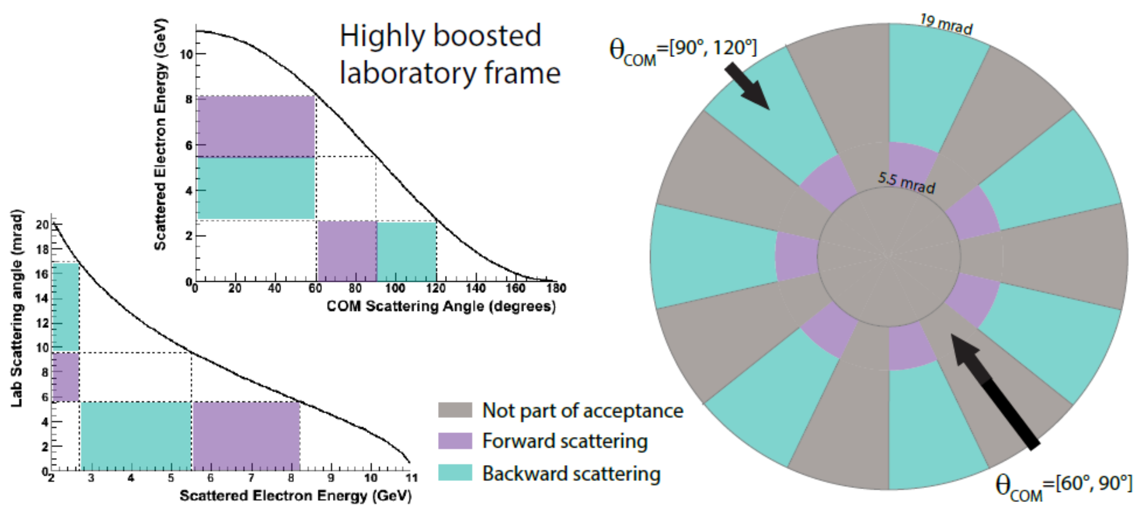

The spectrometer system includes the acceptance defining copper-tungsten alloy (CW95) collimator 2 and collimator 4. The collimator 2 accepts Møller electrons with scattering angle $60 - 120$ degree in the center-of-mass frame [Kumar et al., 2020]. Since the Møller scattering involves identical particles, full azimuthal coverage

Figure 3.14: Cutaway view highlighting the location of collimators and spectrometer coil magnets. Reprinted with permission from author [Kumar et al., 2020].

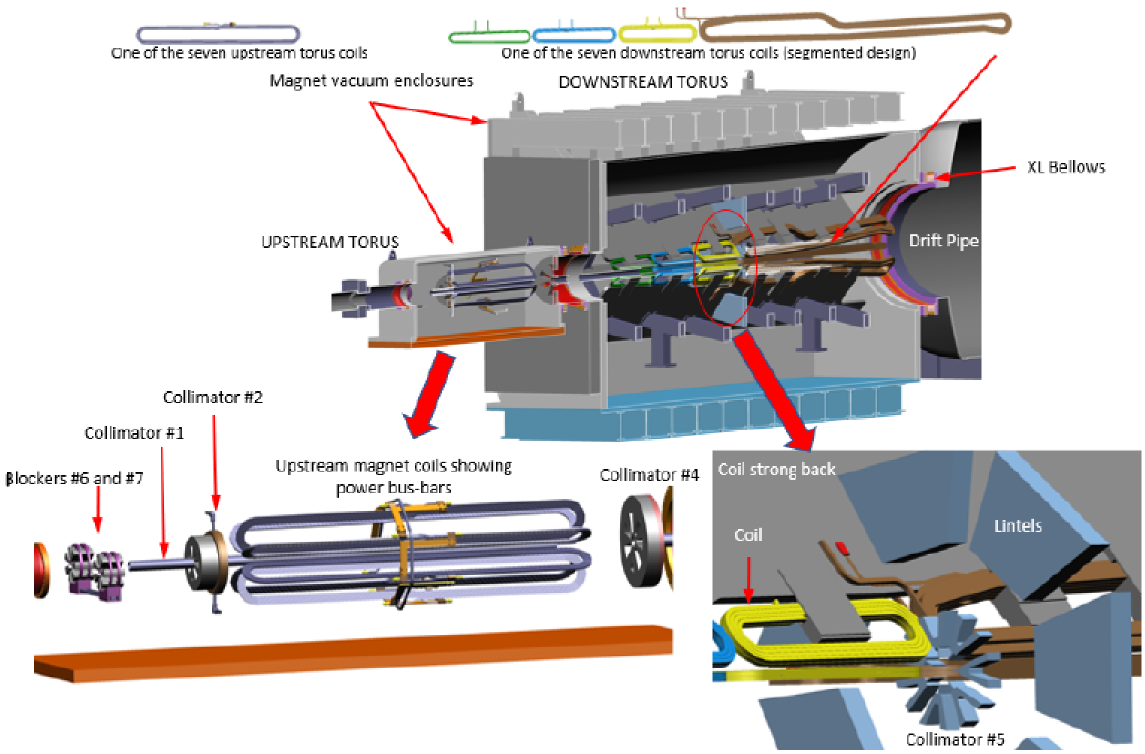

can be achieved by having seven-fold symmetry in the collimator acceptance holes as shown in figure 3.13. The collimator 4 is sculpted in a way so that it intercepts any thing that is not part of the original acceptance defined by collimator 2. The main component of the spectrometer system are two resistive, water-cooled copper toroidal magnets as shown in figure 3.14 [Kumar et al., 2020]. The coils of the spectrometer have epoxy insulation outside and in between conductor layers. There is also inner support made of G10 material to prevent the coils from deforming. The spectrometer magnets provide focusing of the main Møller signal and kinematic separation from the irreducible backgrounds such elastic and inelastic electron-proton processes at the detector plane. Any plane along the beamline can be divided into open, transition and closed azimuthal sectors with the closed sectors aligning with coil positions and the open sectors occupying the middle azimuthal position between two coils. The closed sector is blocked off collimator 4 to protect the coils in the shadow. Both spectrometer magnets are enclosed within vacuum chambers. The other components of the spectrometer system include water chillers and pumps, beampipe, power supplies, control electronics, etc. [Kumar et al., 2020]

3.3.3 Tracking System

Figure 3.15: Important MOLLER tracking system components. Reprinted with permission from author [Kumar et al., 2020]. The GEMs are located upstream of the main detector system and the pion detector array is located downstream of the main detector system.

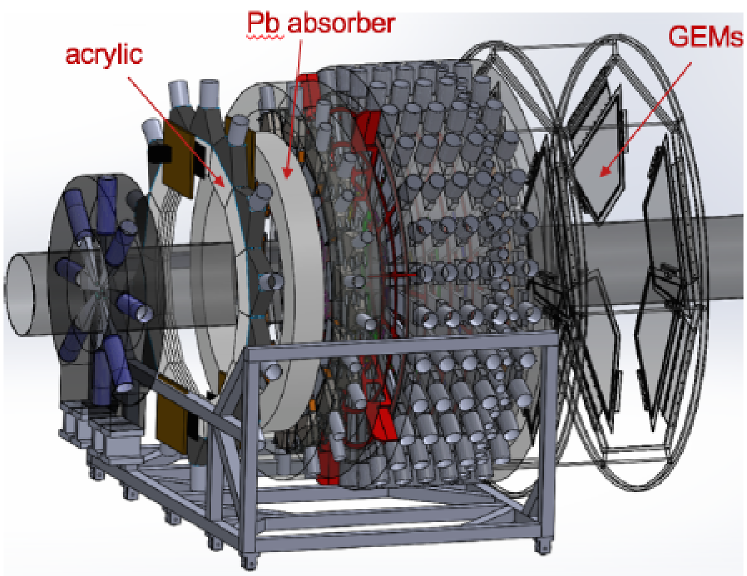

As shown in figure 3.15, the MOLLER tracking system consists of 4 layers of retractable GEM detectors, an acrylic Cherenkov detector array, scintillators at specific locations, and a pair of quartz scanners [Kumar et al., 2020]. The GEMs are located just downstream of the downstream spectrometer and will be used at low current along with sieve hole collimators located farther upstream of collimator 1 for optics calibration and determining experimental kinematics. They will also be used for determining the dilution factors of irreducible backgrounds such as elastic and inelastic eps at the main detector plane [Kumar et al., 2020]. The GEMs can be moved around in the azimuthal direction to achieve full coverage and are parked in retracted position when taking main asymmetry data to avoid overexposure to radiation. The acrylic Cherenkov detector array is used to monitor pions. These detectors are operated at low current to determine the pion dilutions but also operated at the nominal high current to determine pion asymmetries [Kumar et al., 2020]. There will be a lead absorber placed in front of the pion detector array to suppress the Møller flux relative to pions. The pion detector ring is positioned to be in the shadow of ring 5 of the main detector array, also called the Møller ring. When operating at low current, the triggers for the GEMs and the pion detector array are provided by the strategically positioned scintillators. There is also a pair of quartz scanners: one upstream and one downstream at the end of the hall. These are capable of operating at both high and low current with scanner coverage of a single sector of acceptance. The upstream scanner can be used for verifying that the kinematics and backgrounds do not change considerably going from low current to high current. The downstream scanner will be used to ensure beam alignment with the center of the acceptance defining collimator [Kumar et al., 2020].

3.3.4 Main Detector System

The main detector system for MOLLER consists of an array of 224 radiation-hard quartz Cherenkov detectors with air-core light guides and 3 inch PMTs arranged in 6 rings. The ring 5 is the region where the Møller scattering particles are focused. The principle backgrounds like elastic electron-proton and inelastic electron-proton processes are spread among other rings. Within each ring of detectors, there is a high

Figure 3.16: Cutaway view of the main quartz Cherenkov and shower max detector array. The shower max detectors are placed behind the main quartz Cherenkov detectors to provide an alternative energy-weighted measurement of the electron-electron scattering flux. Reprinted with permission from author [Kumar et al., 2020].

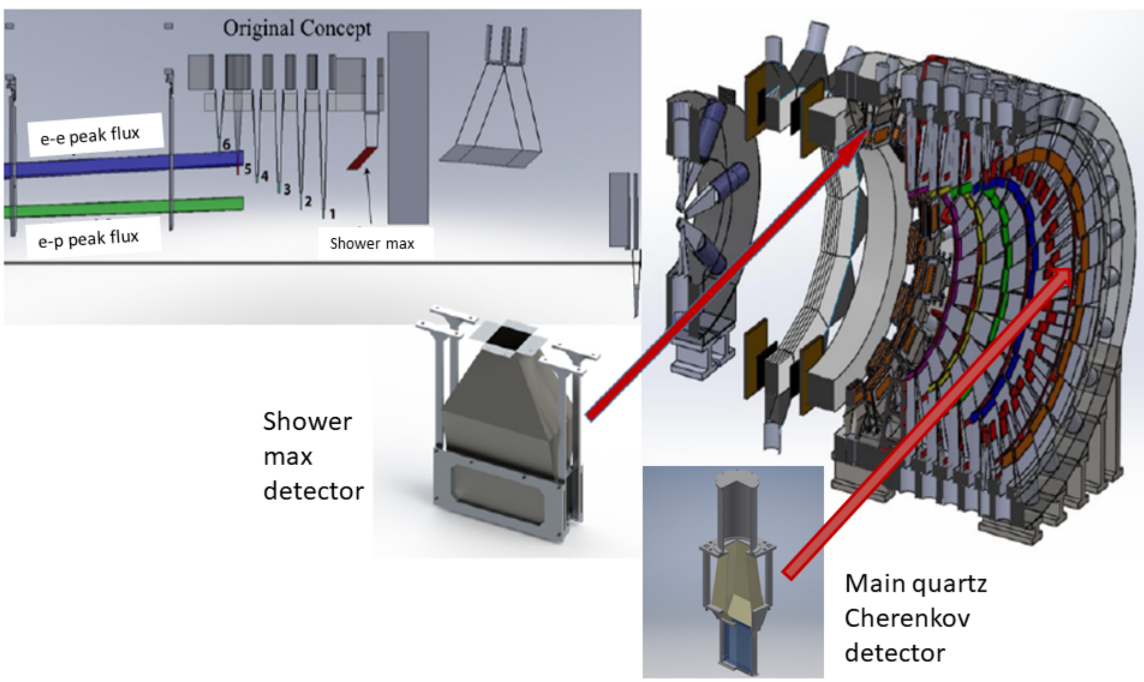

level of azimuthal segmentation because azimuthal defocusing in the spectrometer causes the particles reaching the detector plane have final momentum correlated with where they end up azimuthally on a particular ring. This results in each azimuthal bin capturing slightly different kinematic bites of the acceptance function. With this particular configuration, it is possible to deconvolute the main asymmetry signal from the irreducible backgrounds in analysis. The shower max detector array lies in the shadow of the main detector array and intercepts the same Møller flux. However, the shower max design includes interleaved tungsten and quartz: the first for producing shower from incident flux and the other for capturing the light. This allows to achieve an auxiliary energy-weighted measurement of the incident flux on ring 5 less sensitive to hadrons and soft backgrounds. A cutaway view of the main quartz Cherenkov and shower max detector array is shown in figure 3.16. Since the detectors need to operate at extremely high rate environment, an integration mode data acquisition system (DAQ) will be used for them during the main measurement.

3.3.5 Other Systems

Similar to PREX-2, MOLLER will have an integration mode and a counting mode DAQ. The integration mode DAQ interfaced with the main detector system will be operated at the nominal 65 uA beam current with a helicity flip rate of 1920 Hz to cancel out the 60 Hz noise [Kumar et al., 2020]. The counting mode DAQ will be used along with the tracking system to perform optics calibration, establish experimental kinematics, and estimate certain backgrounds at low current. The helicity electronics dictate the trigger source for the integration mode DAQ whereas the trigger for the counting mode DAQ is provided by strategically located scintillators in the tracking system [Kumar et al., 2020]. The supporting structure of the tracking system are designed so that tracking detectors can be withdrawn during integration mode running. The main detector support structure is designed to be vertically split down the middle to ensure ease of assembly and access to beamline. In addition, on site computing systems will be used to run important feedback systems that help to minimize helicity correlated beam asymmetries as well as record and analyze the data during the experiment [Kumar et al., 2020].

Shielding is necessary to mitigate the effects of radiation on experimental equipment and also reduce the level of background particles at the detector plane. High energy hadrons ($>$ 10 MeV) or low energy neutrons can cause single event effects

Figure 3.17: Important MOLLER shielding components. The main shielding components are made of Tungsten, Lead, or Concrete.

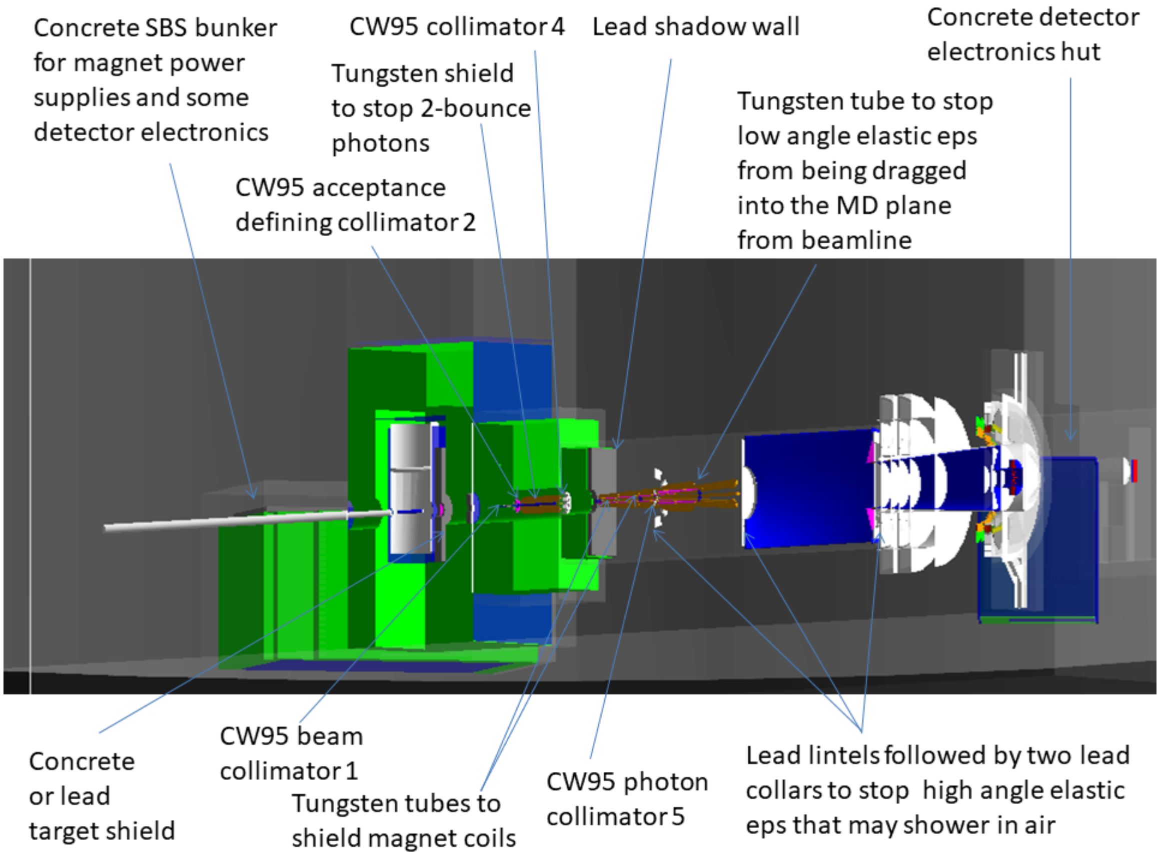

leading to temporary equipment malfunction (ex: memory bit flips). All the different types of particles such as electrons, positrons, pions, photons, neutrons, etc. up to 10 GeV can cause permanent damage to silicon-based chips used in electronics via ionization or non-ionizing energy loss (NIEL) [Kumar et al., 2020]. The spectrometer magnets need to be protected to prevent degrading of insulation due to high radiation dose leading to shorts and failure. Lack of adequate shielding will lead to need for frequent equipment repairs which is a drag on data collection efficiency. Also over the course of experiment, activation of different components will mean that maintenance and repair crew has to wait longer for the radiation environment to cool down to access the hall. This is a personnel safety issue. Another issue effecting personnel will be high energy neutrons (> 30 MeV) that can escape through the roof of the experimental hall and shower in the surrounding area. The dose from such showering needs to be controlled within 10 mrem/yr as mandated by the lab. Figure 3.17 highlights important components of the shielding system for MOLLER to mitigate the radiation-related problems. Equipment that are designed to intercept a lot of the beam such as the target and copper-tungsten alloy (CW95) collimators are enclosed in concrete and steel bunkers. The target receives the most power ($\sim$ 4kW). So, it is surrounded by almost 600 tons of concrete to prevent radiation spreading to sensitive areas such as the roof and 10 tons of steel makes up support. However, the upstream portion of the concrete shield might be taken out going forward. There is also 50 tons of lead downstream of the target which might be replaced with less heavy concrete. The beam collimator 1 intercepts 4 kW power too as it tries to prevent the central beam from spreading out absorbing a large heat load. The acceptance defining collimator 2 which comes right after collimator 1 absorbs around 0.7 kW power and the collimator 4 absorbs around 0.07 kW power. The area around collimator 1 and 2 has about 264 tons of concrete along with supporting steel whereas collimator 4 only has around 2.5 tons of concrete around it [Kumar et al., 2020]. The various other shielding as shown in figure 3.17 such as the lintels and collars, lead shadow wall etc. help to suppress backgrounds at the main detector plane. In addition, the magnet control and power supply equipment along with sensitive detector electronics are protected within two separate bunkers. Finally, the upstream spectrometer has tungsten side plates on the lower arm of the coils and the downstream spectrometer has tungsten inner radial shields to protect the insulation from being damaged. The shielding is continually being optimized and additional local elements may be introduced in the future.

In the next two chapters, I discuss the data collection and analysis processes for PREX-2 and MOLLER respectively utilizing the apparatus described in this chapter and specially focus on my particular contributions to the processes.

Chapter 4

PREX-2

In this chapter, the data collection and analysis tools for PREX-2 are discussed with a focus on my contributions. I was mainly involved in the real-time analysis and post-experiment data-processing. I summarize the results of important analyses, performed by fellow collaborators, that contributed to the final results for completeness. The final results from the experiment are also provided.

4.1 Research Methods

In this section, I discuss the tools that were used to collect and process PREX-2 data. I also discuss the optics calibration process that defined the experimental kinematics. I highlight my software contributions for these efforts along with my contributions as an experimental shift worker and a weekly analysis coordinator.

4.1.1 Data Collection and Post-Processing

The parity and the counting mode DAQs were not operated simultaneously. The parity DAQ was used to collect the main asymmetry measurement data at the nominal beam current ($\sim$ 70 uA) and the counting-mode DAQ was used for calibrating optics, collecting Q^2 measurement data, and measuring backgrounds at low beam current ($\sim$

nA to uA level). The data from the DAQs and supplementary information from the accelerator control system EPICS [Controls Software Group, 2017] were analyzed in real-time by JAPAN, an analysis software developed by the PREX-2 collaboration [PREX Collaboration, 2018].

Figure 4.1: An octet helicity flip pattern during PREX-2. Reprinted with permission of author [Ye, 2020]. A 120 Hz quartet flip pattern was used at the beginning of the experiment but a 240 Hz octet pattern was used later in the experiment. Both patterns have the advantage of suppressing 60 Hz electronics noise.

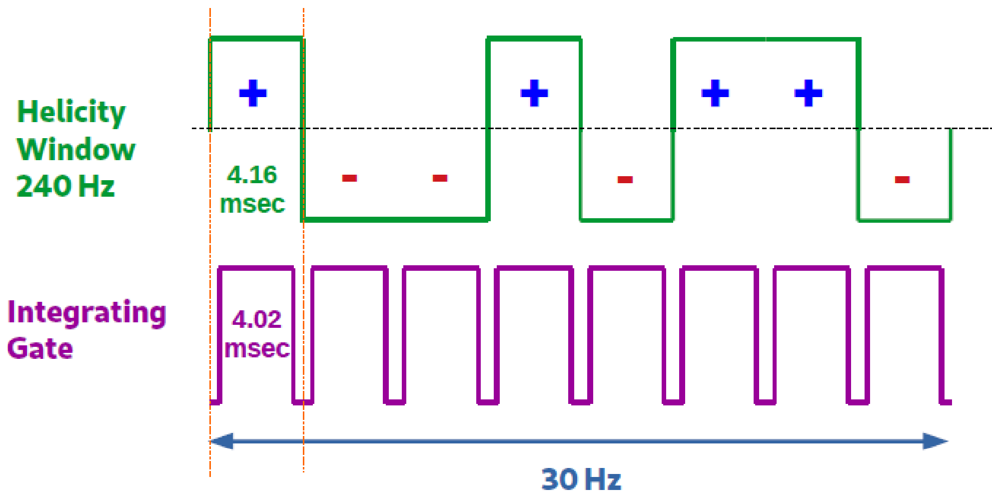

During the main asymmetry measurement, the data was taken with one of the lead-diamond sandwich targets at mostly 70 μA beam current. The beam helicity was flipped in 120 Hz quartet or 240 Hz octet patterns as shown in figure 4.1. The information for individual events was not recorded by the parity DAQ. Rather the asymmetry over an entire multiplet pattern was calculated using integrated intensity normalized yields in opposite helicity states within the pattern [Ye, 2020]. A good multiplet is a multiplet without beam trips or device failures. The data was grouped in different time scales during the experiment. A collection of $\sim$ 10000 good multiplets formed a “minirun”, a collection of miniruns formed a “run”, and a collection of runs formed a “slug”. The slugs were again grouped under specific HWP & Wien states and the entire experiment was a collection of four unique HWP & Wien states. The grouping over different time scales were done to ensure that purely statistical behavior existed at all scales.

I added the prompt summary output feature in JAPAN [PREX Collaboration, 2018]. It extracted useful information such as the number of events with good data, and the yields and asymmetries/differences associated with various devices during each period of experimental running from the data stream. Then it printed out the information in a human readable format. This was a useful tool for real-time beam quality monitoring and beam time accounting. An example of the prompt summary output is shown below:

```
Run: 5408
Start Time: 2019-12-12 22:43:30
End Time: 2019-12-12 23:19:42
Number of events processed: 259910
Number of events in good multiplicity patterns: 190444
Percentage of good events: 73.3 %
==========================================================================
Yield Units: bcm($\mu$A), cavq($\mu$A), bpm(mm), sam(mV/$\mu$A)
Asymmetry/Difference Units: bcm(ppm), cavq(ppm), bpm(um), sam(ppm)
==========================================================================
                                  Yields
==========================================================================
           bcm_an_us | Mean:  103.748 +/-    0.004   Width:    0.937
           bcm_an_ds | Mean:  103.687 +/-    0.004   Width:    0.935
             --------- | Mean:  ------- +/-    -----   Width:    -----
                sam6 | Mean:   10.998 +/-    0.000   Width:    0.019
                sam7 | Mean:    1.779 +/-    0.000   Width:    0.007
==========================================================================
                          Asymmetries/Differences
==========================================================================
           bcm_an_us | Mean:    0.846 +/-    1.145   Width:  249.763
```

```
bcm_an_ds | Mean:    0.665 +/-    1.142   Width:  249.134
--------- | Mean:  ------- +/-    -----   Width:    -----
     sam7 | Mean:    3.045 +/-    2.818   Width:  614.800
     sam8 | Mean:    1.097 +/-    1.574   Width:  343.480
```

Figure 4.2: Slug level aggregator output for bpm12X differences. An example of an aggregator plot used to check beam quality. The position differences needed to be minimized to ensure that the helicity correlated beam asymmetry correction using regression does not fail.

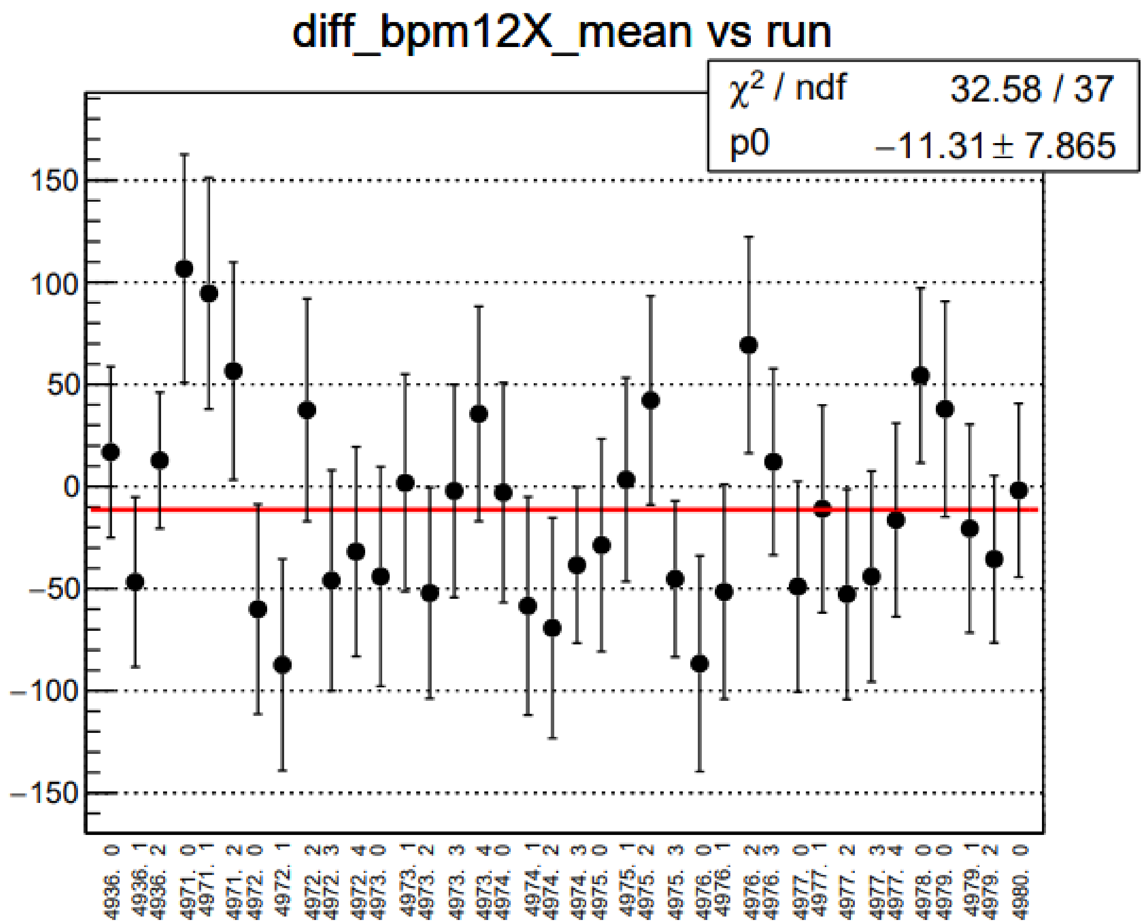

An output ROOT file produced by JAPAN contained information at the run, minirun, and multiplet levels. To view the data at larger time scales, I contributed towards

Figure 4.3: Grand aggregator output for bpm12X differences showing all HWP (In / Out) & Wien (Right / Left) states. Slow drifts in beam properties are expected. So, the moderately high reduced χ^2 in the fits over long timescales as shown in the figure are not a point of concern. In any case, the slow drifts are canceled out by fast helicity reversals and regression corrections at a much faster time scale. However, the position differences in all bpms should average out close to zero over the course of the experiment to achieve further suppression in systematic uncertainties. With the help of the quality check plots, corrective measures were taken by parity quality beam experts during the experiment to ensure this.

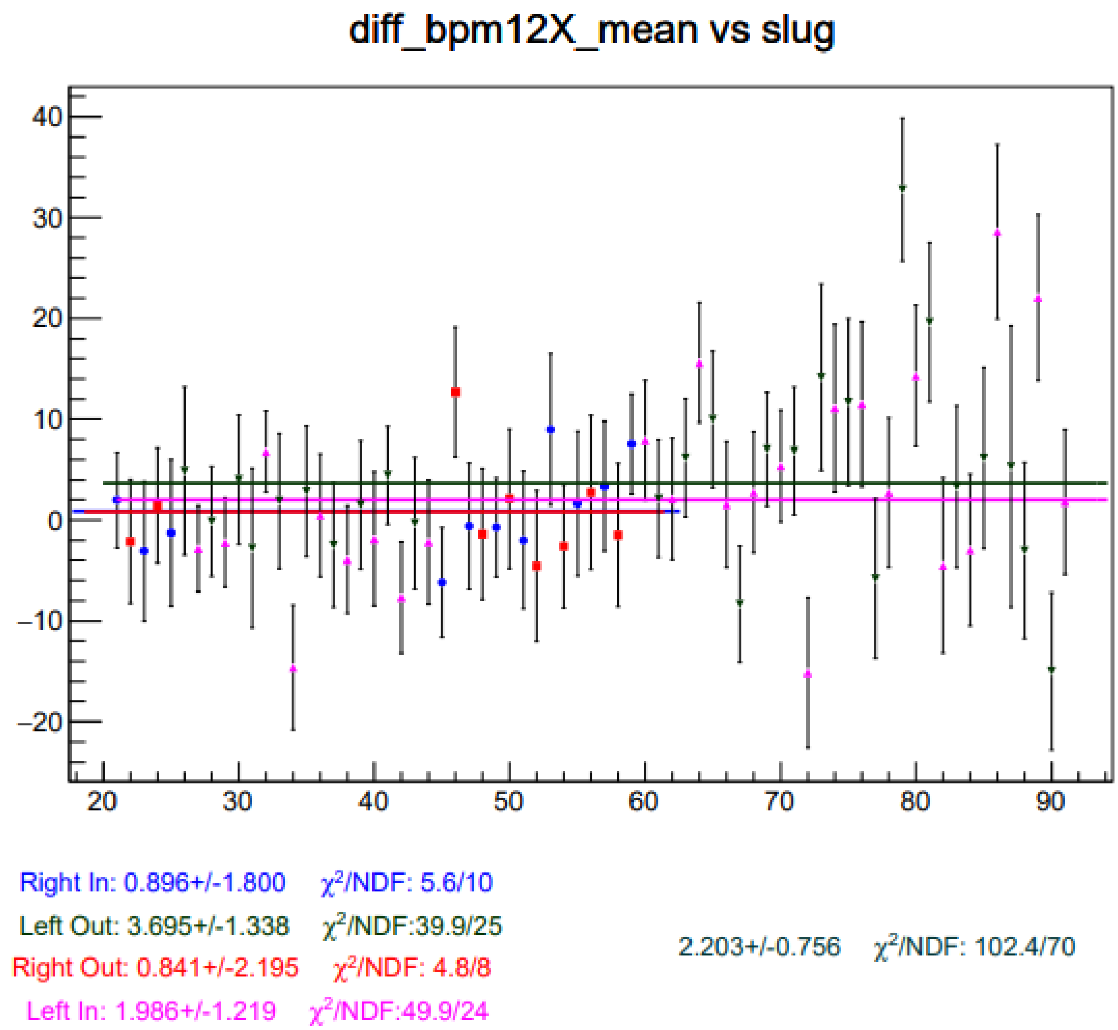

the development of an aggregator framework [PREX Collaboration, 2018]. The aggregator had the capability to take a specific device list as input, extract minirun level data from many output root files and combine them to produce plots of yields and asymmetries/differences from various devices over a longer period. These aggregator plots were used by experts in various subsystems to ensure high data quality. Examples of aggregator output for bpm12X differences at different aggregation levels are shown in figures 4.2 and 4.3. Plots similar to these were used by parity quality beam experts to take corrective measures during the experiment if necessary.

In addition to the above contributions, I also worked as an experimental shift worker and a weekly analysis coordinator. I carefully monitored data at various levels of aggregation, sorted runs into good and bad/suspicious categories in the run control database, and created slurm job submission scripts for post-experiment JAPAN analysis of data on the JLAB ifarm cluster with refined pedestals and other updated information. During my shifts in the commissioning period, I was involved in the optics alignment with the high resolution spectrometers. This is discussed in the next subsection.

4.1.2 Optics Calibration

The high resolution spectrometers (HRS) needed to be calibrated for accurate measurement of the accepted kinematic (Q^2) distribution. The calibration involved determination of the transport tensor that linked the spectrometer focal plane variables measured by the vertical drift chambers (VDCs) to the variables at the target. The relationship could be expressed as follows [Kiadtisak, 2013],

$$\begin{bmatrix} \theta \\ \phi \\ y \\ \delta \end{bmatrix}_{tg} = \Big[\text{Optics Transport Tensor}\Big] \begin{bmatrix} x \\ \theta \\ y \\ \phi \end{bmatrix}_{fp} \tag{4.1}$$

Figure 4.4: The target coordinate system for the left HRS. Created based on source image [Kiadtisak, 2013]. x_{tg} and x_{sieve} are into the plane. y_{tg} and y_{sieve} are as shown. L is the distance from the hall center to the sieve plane. D is the displacement of the target from its ideal position. θ_0 is the spectrometer central angle with respect to the beam axis. $x_{tg} = 0$ in this setup. In addition, $z_{react} = 0$ since a thin foil was used instead of an extended target.

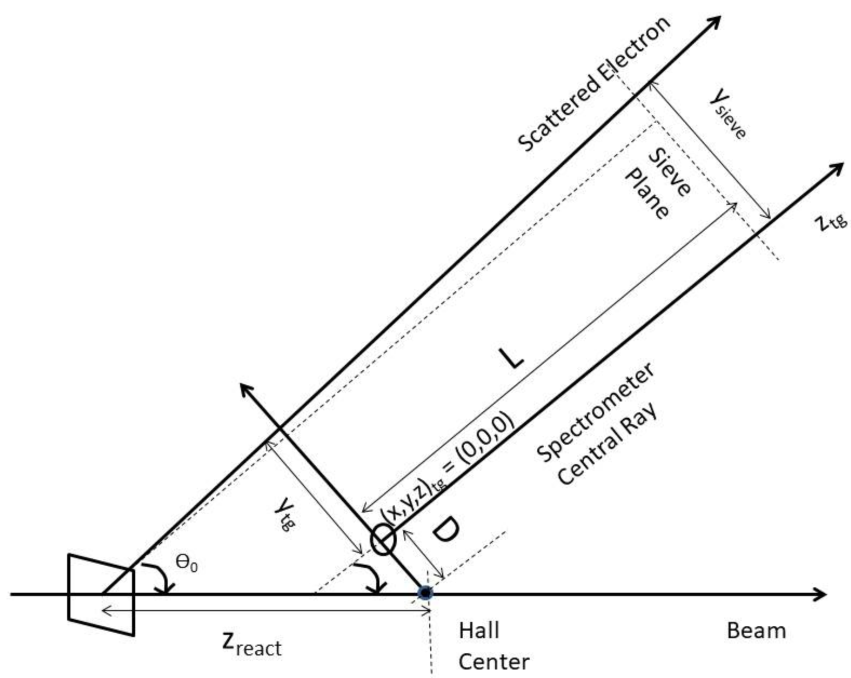

The θ_{tg} and ϕ_{tg} variables were related to the angular calibrations and the δ_{tg} variable was related to the momentum calibrations. The folding of these variables into the Q^2 calculation and interpretation is discussed in section 4.2.1.

During the angular and momentum calibrations, the thin Carbon target was used at low current with the counting-mode DAQ. The reference sieve slit collimators on the two spectrometer arms were necessary for these calibrations. Each hole in a sieve slit collimator (either on the right or left arm) corresponded to a unique set of values for the target variables.

Figure 4.5: Optics Reconstruction at Nominal Momentum for Left HRS. The sieve collimator has a few holes that are designed to be bigger in size compared to other holes. When the optics database is not optimized, the distribution coming through the sieve holes appears smeared when back-projected from the VDC plane. However, the intensity variation across different holes was picked up by an automated script that was using 2d-Gaussian fits to associate the reconstructed blobs with the correct physical sieve hole. Then by iteratively optimizing the optics database through minimization of the difference between the reconstructed and actual sieve hole positions, we can get a clear picture with no smearing as shown in this figure. Reprinted with permission of author [Jian and Liyanage, 2020].

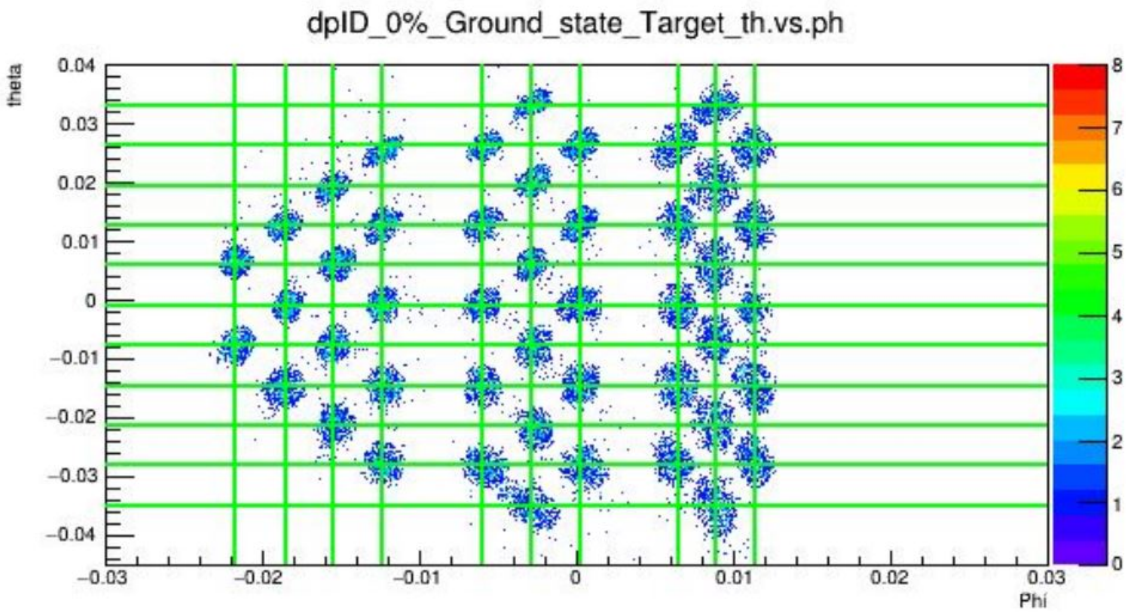

The expected values for target variables when scattered electrons passed through a sieve slit hole was calculated with the following equation [Kiadtisak, 2013],

$$\begin{bmatrix} \theta \\ \phi \\ y \end{bmatrix}_{tg} = \begin{bmatrix} \tan^{-1}\left(\frac{x_{sieve}}{L}\right) \\ \tan^{-1}\left(\frac{y_{sieve}-x_{beam}\cos(\theta_0)+D}{L-x_{beam}\sin(\theta_0)}\right) \\ y_{sieve} - L\left(\frac{y_{sieve}-x_{beam}\cos(\theta_0)+D}{L-x_{beam}\sin(\theta_0)}\right) \end{bmatrix} \tag{4.2}$$

Figure 4.6: Optics Reconstruction at Nominal Momentum for Right HRS. The process for the RHRS is the same as the LHRS. We need to ascertain if the LHRS and RHRS reconstructed plots show the same number of sieve holes to ensure proper optical alignment. Reprinted with permission of author [Jian and Liyanage, 2020].

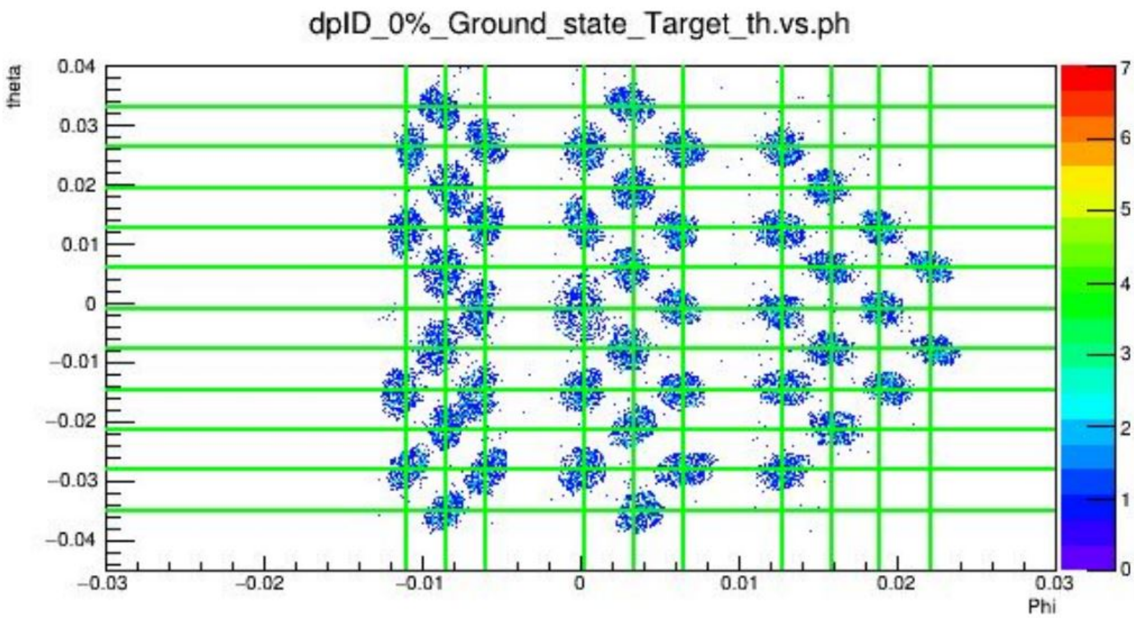

Note that x_{beam} and y_{beam} were measured in the hall coordinate system where the y-direction is the vertical direction and the x-direction is the horizontal direction. The convention is opposite in the target coordinate system.

For the angular calibrations, the scattered electron tracks passing through different sieve holes were reconstructed using our initial guess of the optics tensor from PREX-1. During commissioning, I developed one of the scripts to identify the sieve holes from a $2D$-plot of reconstructed θ_{tg} and ϕ_{tg} as shown in figures 4.5 and 4.6. 2-dimensional Gaussian fits with specific spread and height thresholds were used to automate the process of locating the intensity peaks on the $2D$-plot. This was compared with the expected values at the target obtained using equation 4.2. Then

Table 4.1: The calibration accuracies for θ, ϕ, and δ at the target. Reprinted with permission from the author [Jian and Liyanage, 2020].

HRS	θ deg(mrad)	ϕ deg(mrad)	δ (MeV)
Right	0.089 (1.566)	0.018 (0.32)	0.5
Left	0.042 (0.732)	0.028 (0.492)	0.3

the distance between the two sets of values of target variables were minimized. It produced slightly improved values for the optics transport tensor coefficients. This process was repeated iteratively until the optics tensor was optimized and the total uncertainty was minimized. For the momentum calibration, runs were taken at different spectrometer momenta [$Dp = -1\%, 0\%,$ and 1% compared to nominal momentum] to cover most of the focal plane. In each case, an iterative minimization of the distances between reconstructed and expected δ_{tg} were performed similar to the angular calibration [Jian and Liyanage, 2020; Kiadtisak, 2013]. The calibration accuracies achieved for the different target variables are shown in table 4.1 [Jian and Liyanage, 2020].

4.2 Analysis and Results

In this section, I summarize important analyses performed by fellow collaborators including the kinematic acceptance (Q^2) distribution calculation, calculation of dominant corrections, the final PREX-2 result for parity violating asymmetry, and the derived neutron matter properties.

4.2.1 The Q^2 Measurement and Acceptance Function Determination

The Q^2 measurement was performed to derive meaningful conclusions from the A_{PV} measurement. The data for this measurement was collected with the counting mode DAQ at low current in between production runs. According to equation 2.3, the quantities of interest to calculate the Q^2 are the initial beam energy (E), the final momentum of the scattered electrons (E') and the scattering angle (θ). Note that the experimentally measured A_{PV} and Q^2 are not absolute values rather averages over distributions that are determined by the acceptance function $\epsilon(\theta)$.

The first step in the Q^2 measurement was to determine the spectrometer central angles (θ_0) for both left and right HRS. For this, a pointing measurement was performed with the water cell target. As shown in figure 4.7, the technique exploited the difference between the peaks of scattered electron momentum (E') distributions for the oxygen and hydrogen in water [Kiadtisak, 2013],

$$\Delta E' = E'_O - E'_H = E\left(\frac{1}{1+\frac{2E\sin^2\left(\frac{\theta}{2}\right)}{M_O}} - \frac{1}{1+\frac{2E\sin^2\left(\frac{\theta}{2}\right)}{M_H}}\right) + \text{small correction} \quad (4.3)$$

Figure 4.7: The right HRS spectrum for a pointing measurement with the water cell target. Reprinted with permission of author [Jian and Liyanage, 2020].

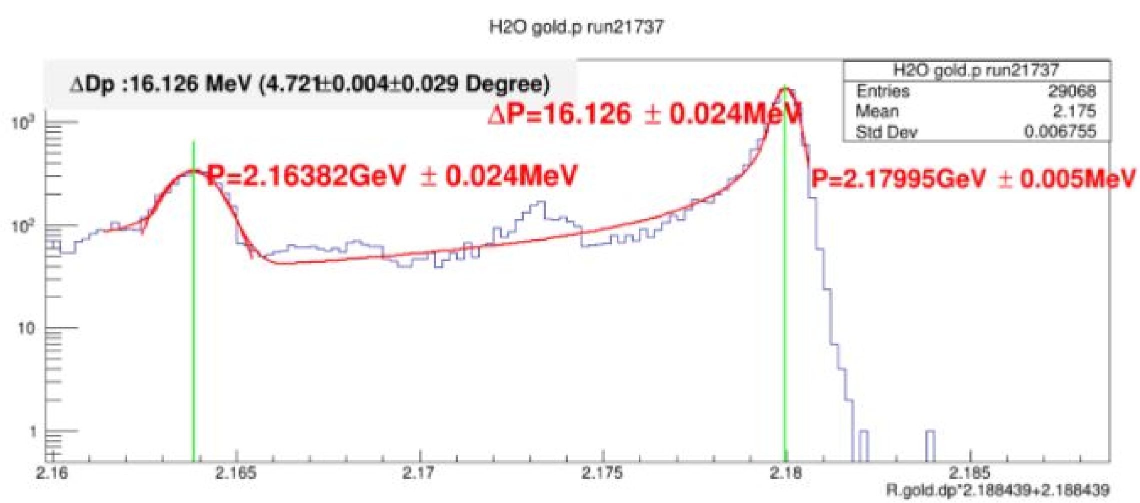

Only tracks passing through the central sieve hole slit were selected so that the θ in the equation 4.3 corresponds to θ_0. The initial beam energy was continuously mea-

Table 4.2: The measured values of the central angles for the two spectrometers [Jian and Liyanage, 2020].

HRS	θ_0 deg
Right	4.747 ± 0.018
Left	4.765 ± 0.016

sured using the non-invasive Tiefenbach method [Kiadtisak, 2013]. The masses $M_{O,H}$ were well known. Then the $\Delta E'$ was extracted for each of the spectrometers and final values of θ_0 were calculated for left and right HRS. A sample run for the right HRS is shown in figure 4.7. The final values of the spectrometer central angle for both HRS averaged over multiple runs are shown in the table 4.2. The pointing measurement was cross-checked with direct position surveys and found to be in good agreement. The scattering angle for all other tracks were calculated using the following equation [Kiadtisak, 2013],

$$\theta = \frac{\cos(\theta_0) - \phi_{tg}\sin(\theta_0)}{\sqrt{1 + \theta_{tg}^2 + \phi_{tg}^2}} \tag{4.4}$$

The target angular and momentum variables were given by the optics reconstruction procedures. After the spectrometer central angle was calculated, it was possible to get the full distributions of scattered angles and momenta. These distributions were then matched against Monte Carlo simulation results to determine the acceptance function ($\epsilon(\theta)$) as shown in figure 4.8. The final reported Q^2 is the average value over the acceptance function [Jian and Liyanage, 2020; Paschke et al., 2021],

$$\left\langle Q^2 \right\rangle = 0.00616 \pm 0.00005 \text{ GeV}^2.$$

The acceptance function was not unique in the sense that different simulation models could produce distributions with the same average scattering angle or $\langle Q^2 \rangle$ with slight differences in asymmetry. A small systematic uncertainty of 2.9 ppb was ascribed to the final asymmetry measurement to take this into account [Paschke et al., 2021].

Figure 4.8: The acceptance function for PREX-2 experiment. Reprinted with permission of author [PREX Collaboration, 2021].

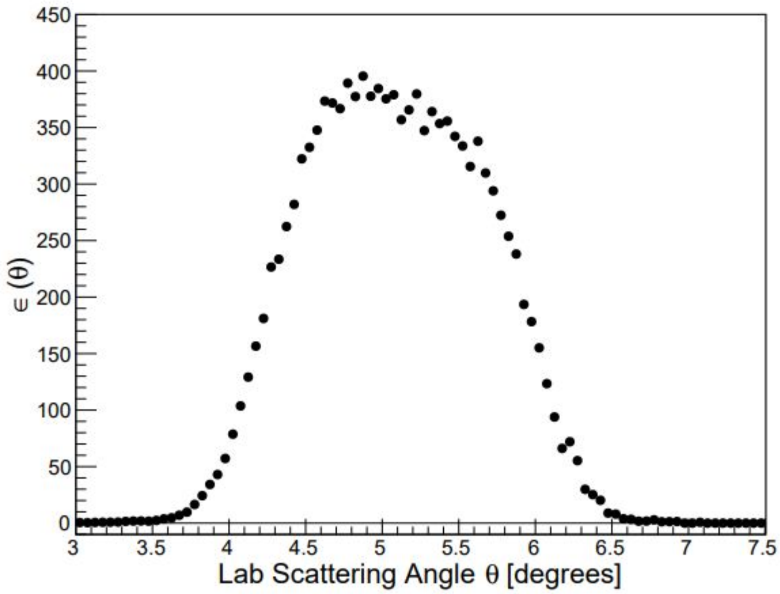

4.2.2 Charge Correction

Figure 4.9: Integrated charge asymmetry during PREX-2. Reprinted with permission of author [Premathilake, 2020]. The charge asymmetry was consistently suppressed during the different run periods in PREX-2 by varying the Pockels cell voltage with a charge feedback loop system.

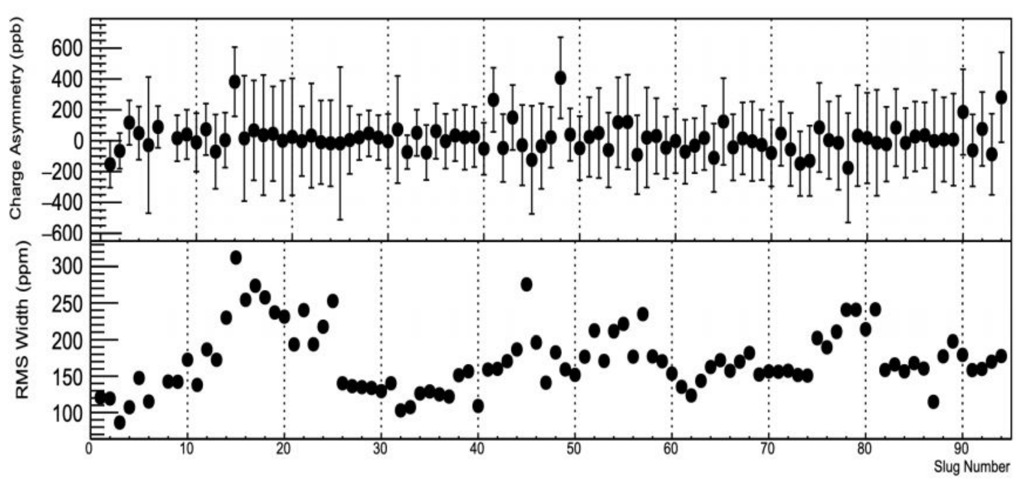

The difference in integrated charge over opposite helicity states may contribute a false asymmetry. During PREX-2, a feedback loop system was used to suppress the effect by varying the pockel cell voltage in the injector based on the measured integrated charge asymmetry between opposite helicity states every 7.5 seconds [Paschke et al., 2021; Premathilake, 2020]. Finally, the accumulated charge asymmetry that needed to be corrected out from the raw measured asymmetry was $A_q = 20.7 \pm 0.2$ ppb [Paschke et al., 2021]. The result was consistent across the different BCMs used in measurement and had very little systematic uncertainty compared to the statistical uncertainty for the experiment. Figure 4.9 shows the history of charge asymmetry during PREX-2.

4.2.3 Helicity-Correlated Beam Asymmetries Correction

The helicity-correlated beam asymmetries (HCBA) are an important correction on the final asymmetry measurement. The helicity-correlated laser spot size was measured in the injector with a linear array photodiode and an upper bound of $5-30$ ppm was found for the spot size asymmetry arising from the second moment of the polarization gradient. This was further suppressed $1-3$ times due to half wave plate cancellations to within a acceptable limit for PREX-2. A fast feedback system was used along with the BPMs to limit the average helicity-correlated position and energy differences in the hall to 1 nm and 1 ppb respectively over the entire experiment [Paschke et al., 2021; Premathilake, 2020]. The fluctuations in beam parameters (position, angle, energy, etc.) could still result in false measured asymmetries. The magnitude of the false asymmetry that needed to be corrected out is given by

$$A_{beam} = \sum_{i=\{x,\theta_x,y,\theta_y,E\}} \beta_i \Delta M_i \tag{4.5}$$

where $\beta_i = \frac{\partial A_{raw}}{\partial M_i}$ are the slopes of raw measured asymmetry (A_{raw}) with respect to the beam parameter (M_i) fluctuations recorded by the beamline sensors [Ye, 2020]. This was addressed by applying corrections combining two independent techniques.

Figure 4.10: An example of beam modulation. Reprinted with permission of author [Ye, 2020]. The dithering technique to correct out helicity correlated beam asymmetries involve deliberate modulation of the beam and recording the resulting beamline sensor and detector responses to quantify slopes of measured asymmetry with respect to beam parameter (position, angle, energy, etc.) fluctuations. For PREX-2, the modulation amplitude was $\sim$ 100 um which was an order of magnitude greater than natural fluctuations and sensor resolutions. The modulation was conducted in 15 Hz cycles to screen out electronic noise from the 60 Hz line. The systematic effect of beam parameter fluctuations was quantified by combining the dithering technique and regression over natural fluctuations. The combined approach is called the Lagrange multiplier method which was used in the PREX-2 analysis.

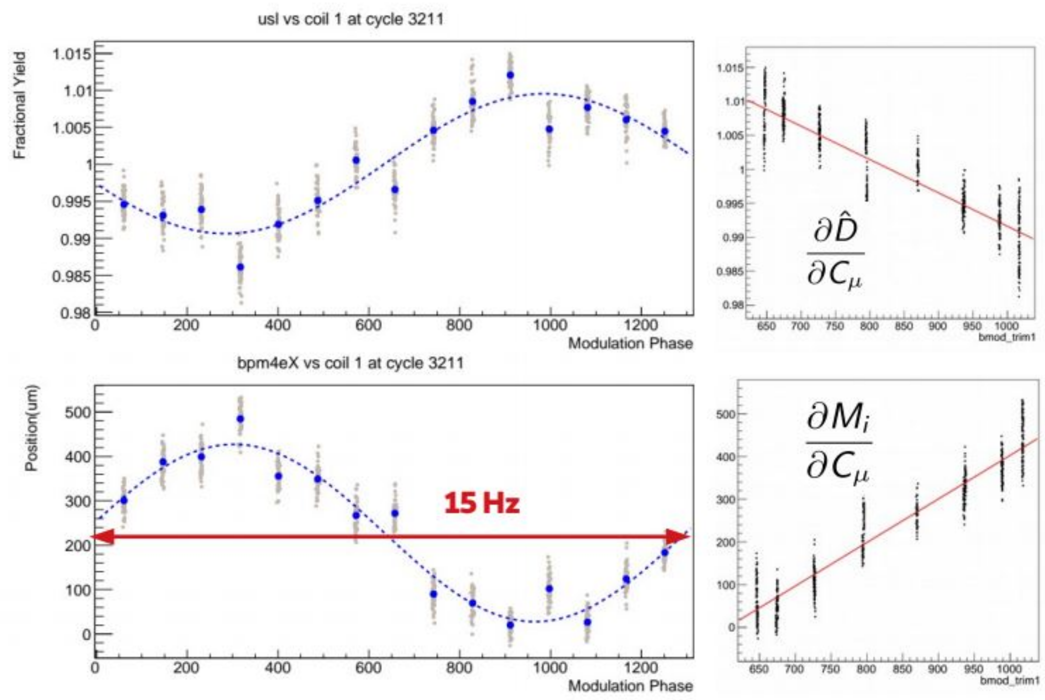

The first technique involved regression with respect to the fast natural fluctuations. In the regression technique, the following quantity is minimized to estimate the coefficients β_i and determine the correction,

$$\chi^2 = \sum (A_{raw} - \sum_i \beta_i \Delta M_i)^2, \ \frac{\partial \chi^2}{\partial \beta_i} = 0 \tag{4.6}$$

The drawbacks of this technique include possible strength sharing leading to variation in β_i, susceptibility to electronic noise, and slope dilution due to finite resolution of the sensors [Ye, 2020].

As shown in figure 4.10, the second technique involved slow and controlled driving of the beam by the beam modulation system called dithering and recording the detector response [Owen, 2020]. For PREX-2, the amplitude of the driven modulation was an order of magnitude higher than random beam noise and sensor resolution. The modulation was conducted at a 15 Hz frequency intermittently so that it was not susceptible to electronic noise from the 60 Hz line. In the dithering technique, the following system of equations needs to be solved:

$$\frac{\partial \hat{D}}{\partial C_\mu} = \sum_{i=1}^{N_{BPM}} \beta_i \frac{\partial M_i}{\partial C_\mu}, \ \beta_i = \frac{\partial \hat{D}}{\partial M_i} \tag{4.7}$$

where $\mu = 1, 2, \cdots, N_{coil}$, $\frac{\partial \hat{D}}{\partial C_\mu}$ are the slopes of the detector response with respect to the driving of the beam modulation coils and $\frac{\partial M_i}{\partial C_\mu}$ are the slopes of the sensor response with respect to the driving of the beam modulation coils [Ye, 2020]. The slopes of the detector response with respect to beam property fluctuations recorded by the sensors ($\beta_i = \frac{\partial \hat{D}}{\partial M_i}$) were extracted from the above set of equations to calculate the required corrections.

The limitations on precision from dithering and regression were overcome by using a combined approach called the Lagrange multiplier method. In this method, the following minimization problem needs to be solved:

$$\mathcal{L} = \chi^2 + \sum_\mu \lambda_\mu \left(\frac{\partial D}{\partial C_\mu} - \sum_i \beta_i \frac{\partial M_i}{\partial C_\mu} \right), \ \frac{\partial L}{\partial \beta_i} = 0, \ \frac{\partial L}{\partial \lambda_\mu} = 0 \tag{4.8}$$

For the Lagrange multiplier method in PREX-2 analysis, 12 beamline sensors were used, constrained by only 5 of the beam modulation coils. Confidence in the method

Figure 4.11: A histogram of octet asymmetries during PREX-2 with Gaussian fit. Reprinted image with permission [Ye, 2020; Paschke et al., 2021]. The histogram of $\sim$ 30 million average asymmetries over individual octets shows very good Gaussian behavior implying proper systematic suppression at short time scales. The data in the plot was taken at 240 Hz helicity flip rate and 70 μA beam current covering $\sim$ 62% of the total statistics.

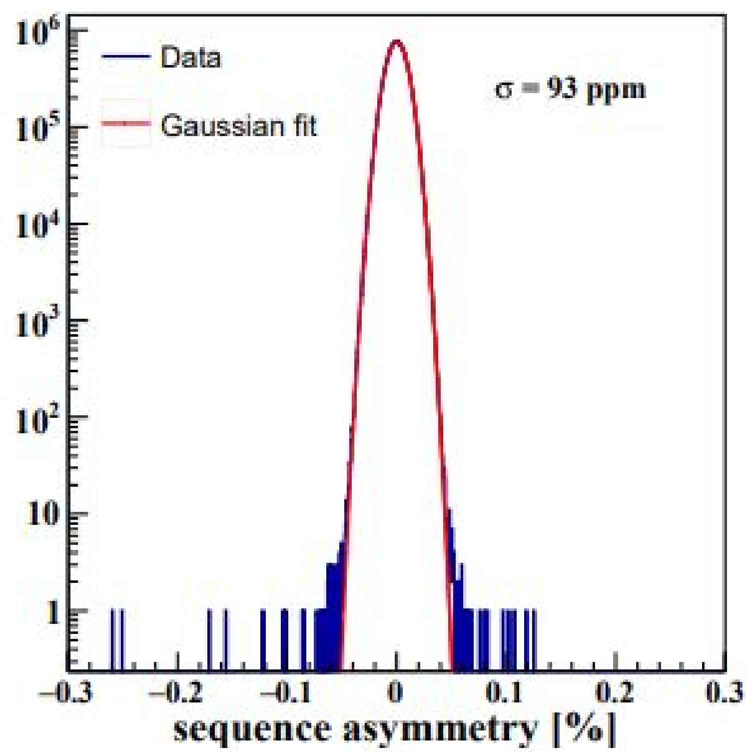

was affirmed by negligible post-analysis residual sensitivity for all the coils and agreement with the two component techniques individually. The figures 4.11 and 4.12 demonstrate that the systematic effects were sufficiently suppressed by the corrections at both short and long time scales. Through eigenvector analysis of the BPM covariance matrix, the contributions to the correction from different parameters were ranked and a 3 % uncorrelated uncertainty was assigned to each of the HCBA contributions. The final result for helicity correlated beam asymmetry averaged over all

Figure 4.12: Distribution of normalized difference of asymmetries recorded in 5 minute intervals from the grand average asymmetry for the experiment $\left(\frac{A_i - \langle A \rangle}{\sigma_i}\right)$. Reprinted image with permission of author [Ye, 2020; Paschke et al., 2021]. The corrected data again showed good fit with Gaussian curve implying systematic effect suppression at longer time scales.

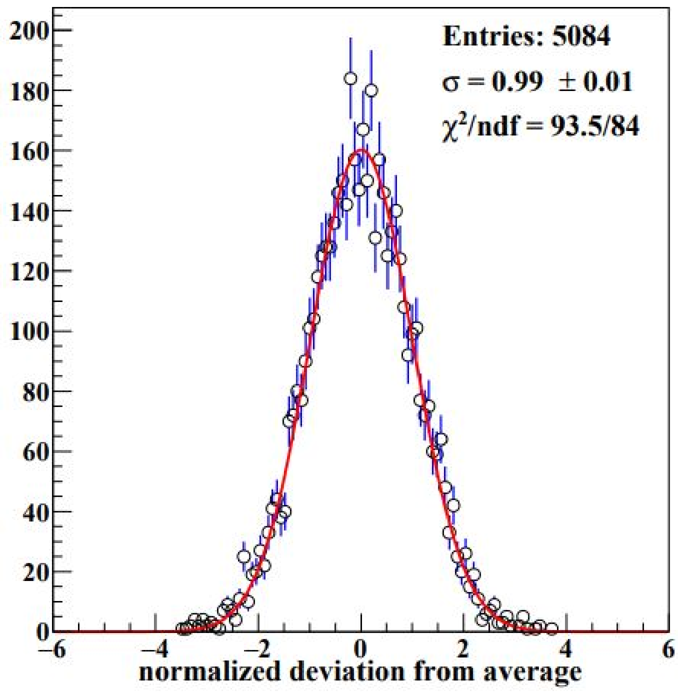

data was [Ye, 2020; Paschke et al., 2021],

$$A_{beam} = -60.38 \pm 2.5 \text{ ppb}.$$

The final reported A_{PV} had this correction baked in.

4.2.4 Polarization Measurement

The Mott polarimeter was used to optimize the degree of longitudinal electron beam polarization by measuring the polarization right after the injector at the beginning of the experiment [Paschke et al., 2021]. The main polarization measurement that goes into the final asymmetry calculation was conducted with the Møller polarimeter. The equation 3.2 was used to calculate the beam polarization by determining the terms on the right hand side. The Møller polarization measurements were done at low current and at a frequency of $\sim$ 30 Hz [Jones, 2020]. The main systematic contribution to the polarization measurements came from the correction needed to account for an unanticipated iron foil wrinkle, extrapolation of results to high current (PREX-2 main data was taken at 70 μA), sensitivity of analyzing power to beam orbit contribution, averaging data from different half-wave plate states which differed slightly due to suboptimal injector setup, and extrapolation of data from stable running period to earlier post-commissioning period where sparse measurements were available [King, 2020; Jones, 2020]. As shown in figure 4.13, the final polarization measurement after weighting the the results from different half-wave plate states by the error in A_{PV} for each state was,

$$P_z^{beam} = 89.7 \pm 0.8\%$$

Figure 4.13: Møller polarization measurement during PREX-2. Reprinted with permission of author [King, 2020; Jones, 2020]. After correcting for foil thickness anomaly, the polarization measurements in different half-wave plate states were roughly constant and within 1% of each other. Weighting the results by the error in A_{PV} for each state, gave a combined average value of $P_z^{beam} = 89.7 \pm 0.8\%$.

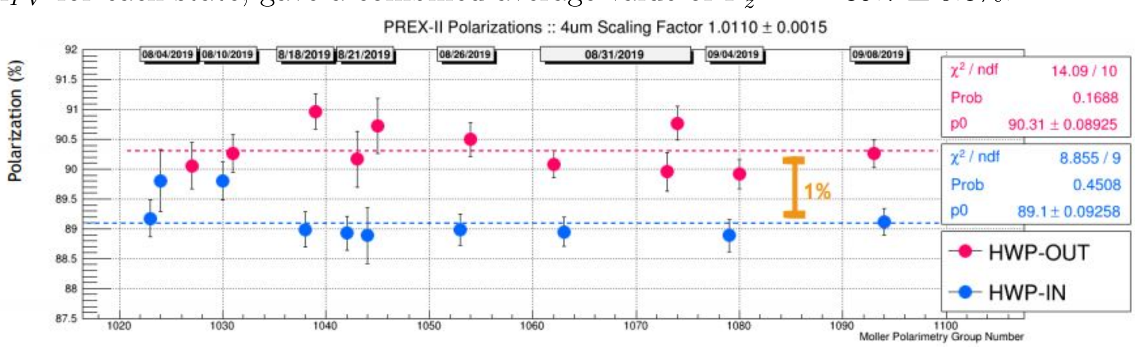

As shown in figure 4.14, the Compton polarimeter was used to cross-check the Møller polarimeter measurement. The photon calorimeter in the Compton setup recorded backscattered photons up to ~ 30 MeV [Zec, 2020]. For each pulse event at the detector, the integrated signal over pedestal was calculated. The Compton spectrum formed by the collection of integrated pulses showed good agreement with simulation. To get the terms necessary to calculate beam polarization, measurements for both laser states (on/off) and beam helicity states (+/−) were needed. Then, the helicity pattern differences (Δ) and sums (Y) were calculated [Zec, 2020],

$$\Delta^{ON/OFF} = S_{+}^{ON/OFF} - S_{-}^{ON/OFF} \tag{4.9}$$

$$Y^{ON/OFF} = S_{+}^{ON/OFF} + S_{-}^{ON/OFF} \tag{4.10}$$

The above information was used to calculate laser on and off asymmetries [Zec, 2020],

$$A^{ON/OFF} = \frac{\Delta^{ON/OFF}}{\langle Y^{ON} \rangle - \langle Y^{OFF} \rangle} \tag{4.11}$$

Then, the beam polarization was extracted from the rewritten equation 3.3,

$$P_z^{beam} = (\langle A_{ON} \rangle - \langle A_{OFF} \rangle) \cdot \frac{1}{P_\gamma < A_S >} \tag{4.12}$$

Figure 4.14: Comparison between Compton and Møller polarization measurement during PREX-2. Reprinted with permission from author [Zec, 2020]. The Møller polarization measurement is shown by the shaded regions and the Compton data points (statistical errors only) are overlaid on top. The results show good agreement but poorly understood features in Compton data prevented it from being averaged with the Møller measurement.

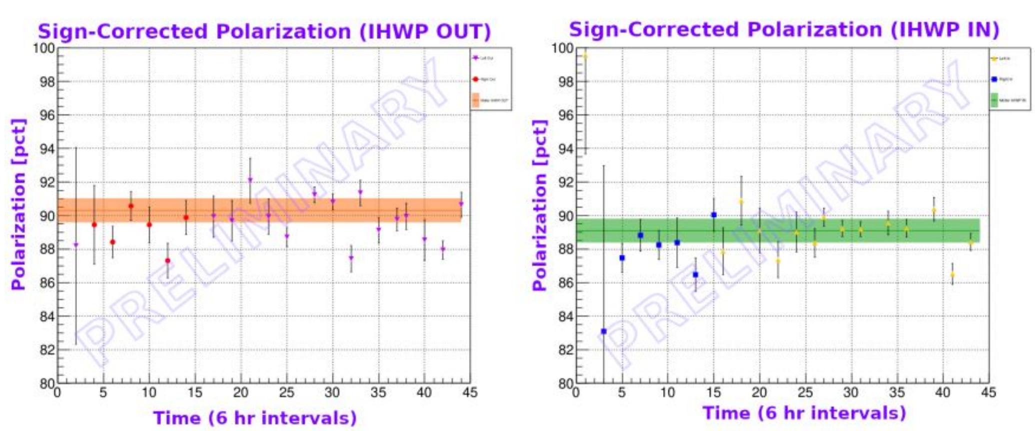

The compton data was collected in integrating mode because no energy calibration or deadtime correction was needed. However, small sensitivities were noticed with respect to pedestal noise and detector nonlinearities. Due to some poorly understood features in the Compton data, it was only used as a consistency check for Møller polarization measurement and not averaged together [Zec, 2020]. It still showed agreement within 0.8% of the systematic window of Møller polarization measurement.

4.2.5 Other Corrections

For correcting out contributions of background processes from the measured parity-violating asymmetry, both the dilution $\left(f_i = \frac{rate_i}{\sum_i rate_i}\right)$ and asymmetry of the individual processes were taken into account [See equation 4.13]. In addition, corrections were considered for detector nonlinearities and transverse asymmetry contributions. As shown in table 4.3, all of these corrections were very small or negligible enough to fold in as systematic uncertainties.

The carbon in the D-^{208}Pb-D target had a significant dilution ($f_C = 6.3 \pm 0.5\%$) factor [Zhang and Park, 2020; Paschke et al., 2021]. The carbon dilution factor was estimated with a benchmarked Geant4 simulation [PREX Collaboration, 2013] and cross-checked with other modes of calculation using form factor data tables or widths of detected asymmetries [Zhang and Park, 2020]. Effects of scattered momentum and target component thickness variations were examined and folded in as small systematic uncertainties. The asymmetry for carbon was also obtained from simulation and cross-checked with Standard Model prediction in the Born approximation [Zhang and Park, 2020]. Since the carbon asymmetry ($A_C = 539.36$) ppb was very similar to the ^{208}Pb asymmetry, the total correction due to carbon contamination was very small despite the large dilution factor. In the end, a correction of 0.7 ± 1.4 ppb was assigned to the final measured parity-violating asymmetry [Zhang and Park, 2020; Paschke et al., 2021].

Figure 3.9 demonstrated how the main detectors were positioned so that only the

Figure 4.15: Measurement of background rescattering probability with LHRS $\frac{dP}{P}$ scan. Reprinted with permission from author [Adhikari, 2020b].

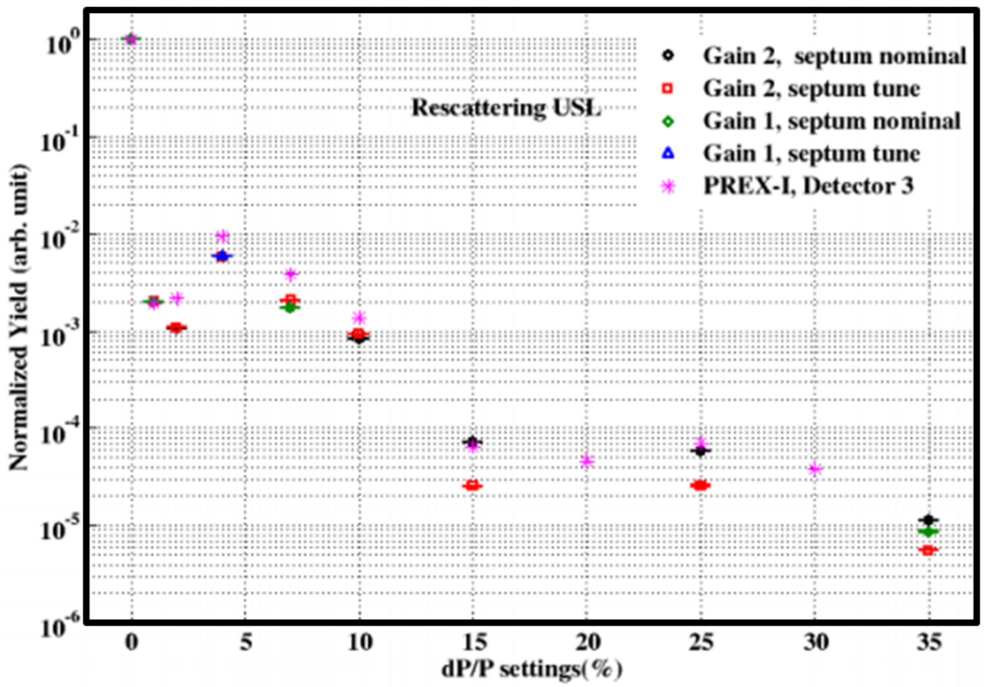

events in the elastic peak were accepted and the events in the radiative tail of the spectrum were not accepted by the main detector quartz. However, the electrons making up the radiative tail could rescatter off the HRS walls and make it into the quartz acceptance. As shown in figure 4.15, HRS magnet scans were performed to shift the elastic peak so that it traversed the same path as the electrons on the radiative tail and the ratio of the detector yields at offset setting to nominal setting gave the rescattering probability of electrons in the radiative tail. By combining the rescattering probability with the relative cross-section of events in the tail normalized by the elastic cross-section, the dilution factors were calculated. The asymmetry for events in the tail were approximated as a linear function of Q^2. Combining all the information, the total correction was found to be very small ($\sim 0.001\%$) relative to the final measured asymmetry. Another type of rescattering was pole tip scattering. It refers to the electrons that only made it into the quartz acceptance because of undergoing Møller scattering with electrons inside magnetized iron in the dipole magnet of the HRS. Since the dipole just had electrons polarized in the horizontal direction, the correction due to it simplifies to $dA = fP_{e1}P_{e2}A$ [Aniol et al., 2004]. The dilution factor, calculated with a combination of simulation and re-scattering study with different spectrometer tunes, was found to be $f = 4.5 \times 10^{-9}$. Spin precision in the septum gave the scattered electrons from target a horizontal polarization component of magnitude $P_{e1} = 0.26$ [Paschke et al., 2020]. The polarization of the electrons in the magnetized iron was $P_{e2} = 0.03$ [Aniol et al., 2004]. The associated analyzing power was calculated to be $A = 0.04$. So, the total correction due to this process was $dA = 4.5 \times 10^{-9} \times 0.26 \times 0.03 \times 0.04 \sim 1.4 \times 10^{-12}$ [Paschke et al., 2020]. This was still a conservative estimate since there would be a cancellation due to different precession directions in left and right arm septum. Lastly, the contributions of electrons scattering from the excited states of the ^{208}Pb were also considered. As shown in figure 4.16, the acceptance fraction for the first 4 excited states were calculated by taking the ratio of the scattered momentum spectra with and without the ADC cut used for pedestal subtraction. The acceptance fractions for the four excited states came out to be 30%, 20%, 10%, and 5% respectively [Adhikari, 2020b]. The relative cross-section for the first excited state was found to be 0.1% [Courtemanche, 1978; Adhikari, 2020b]. Combining the acceptance fraction and the relative cross-section for the first excited state, the dilution factor was found to be $30\% \times 0.1\% = 0.03\%$. The asymmetry for the first excited state was calculated to be $A_{\text{first excited state}} = 1.25 \times A_{\text{elastic}} \sim 685.6ppb$ [Adhikari, 2020b; Horowitz et al., 2001]. This translated to a negligible relative correction of the order of $\sim 0.01\%$ relative to the final measured asymmetry. Since the other excited states have far smaller dilution factors and the asymmetry associated with those are not significantly higher, those contribute far smaller corrections. To account for the spectrometer rescattering and excited state contributions, corrections of 0.0 ± 0.1 ppb were assigned in both cases

Figure 4.16: Fraction of accepted electrons scattered from excited states of ^{208}Pb relative to total number of events from excited states. Reprinted with permission from author [Adhikari, 2020b]. The ADC cut takes out the events contributing to detector pedestal. So, the ratio of the scattered momentum spectra with and without ADC cut gives us the acceptance fraction of events in the excited states. The acceptance fraction for the ground state (elastic peak) and the first 4 excited states were 100%, 30%, 20%, 10%, and 5% respectively.

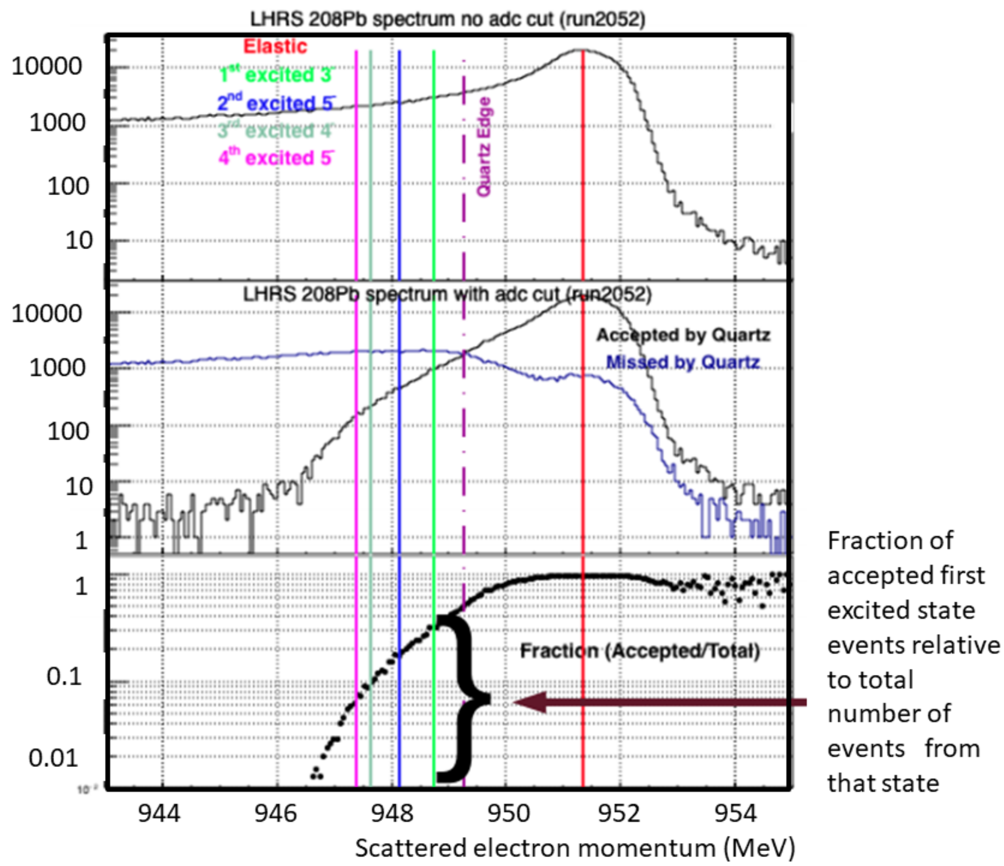

to the final measured asymmetry [Paschke et al., 2021].

The detector nonlinearity contributions were also very low for the asymmetry measurement. The non-linearity of response for each detector PMT was measured with a test stand consisting of two LED lights and a filter wheel before the experiment

Figure 4.17: PMT nonlinearity for each main detector at 10 **nA light level at different highvoltages**. Reprinted with permission from author [Adhikari, 2020a]. The operating voltages used during the experiment are highlighted. At those voltages, the nonlinearity for each PMT was under 0.5%.

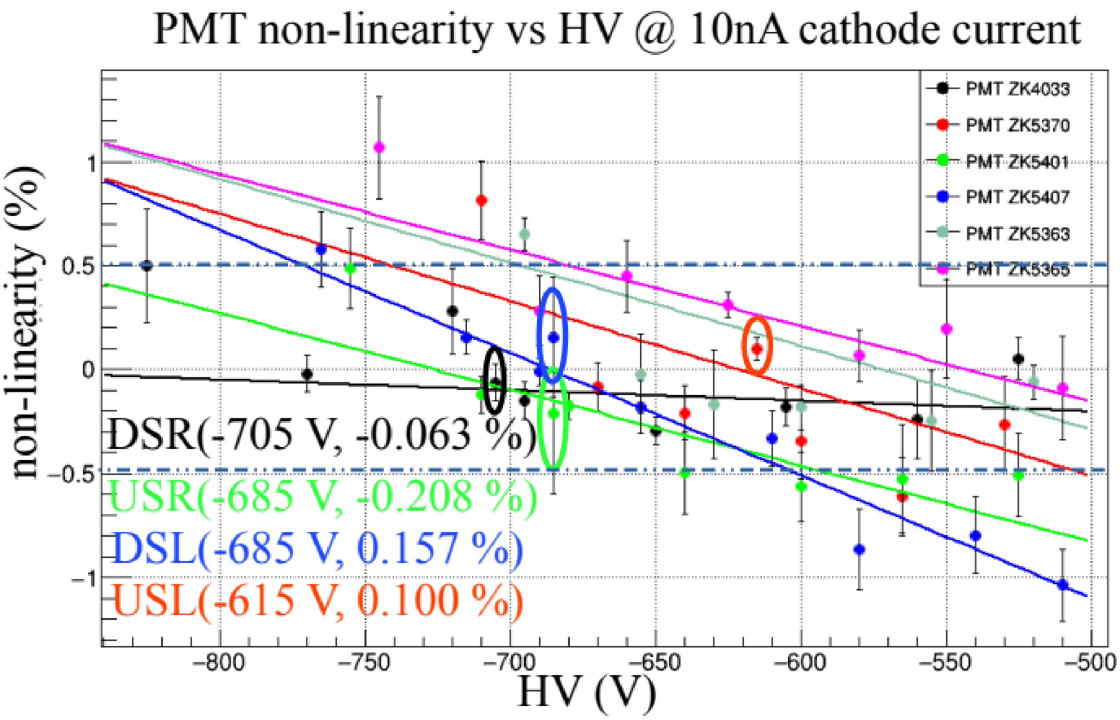

[Adhikari, 2020a]. The detector PMTs were first gain calibrated to operate in a region where the gain was linear with increase in high voltage. In the PMT nonlinearity test, one of the LEDs was subjected to different levels of filter and the other was pulsed at the helicity flip rate. If the PMT response was perfectly linear, the asymmetry measured by the detector would be independent of the filter level. So, the local slope of the change of asymmetry response with respect to the filter level gave a measure of the detector non-linearity. During the experiment, the mean photoelectron yield for each detector was 28 and each detector was exposed to 2.2 GHz of rate at the nominal 70 uA beam current [Adhikari, 2020a]. So, the current in the PMT cathode for each detector was about $2.2 \times 10^{-9} \times 28 \times 1.6 \times 10^{-19}$ nA ~ 10 nA. Figure 4.17 shows that nonlinearity for each PMT was well within 0.5% at the operating voltage and 10 nA light level (LL) [Adhikari, 2020a]. In addition to the above test, the non-linearity was also monitored during the experiment by looking at the detector response with respect to random changes in beam current as measured by the BCMs. In the end, the correction applied to the main measured asymmetry was 0.0 ± 2.7 ppb [Paschke et al., 2021].

The transverse asymmetry contribution arises due to residual polarization in the direction perpendicular to the scattering plane. There is a sinusoidal dependence of the transverse asymmetry on the scattering angle [Armstrong et al., 2007] and with the left-right symmetry of PREX-2, a large suppression of this contribution was obtained. Supplementary measurements were performed with the beam polarization vertical instead of longitudinal during PREX-2 to determine the transverse asymmetry amplitude (A_n) for the D-^{208}Pb-D target and it was found to be very small at the PREX-2 kinematics [Richards, 2020]. Considering the above points and the high degree of longitudinal polarization during PREX-2, the effect of the transverse asymmetry contribution was also considered negligible. The correction assigned to the measured asymmetry due to transverse contributions was 0.0 ± 0.26 ppb.

In the next section, the corrections described so far are summarized and a final value for the unblinded measured asymmetry is provided.

4.2.6 Unblinded Measured Asymmetry (A_{PV}^{meas})

After the helicity-correlated beam asymmetries [see section 4.2.2 and 4.2.3] were screened out, the corrected asymmetry A_{corr} was obtained. The final measured asymmetry (A_{PV}^{meas}) was obtained by correcting A_{corr} for the polarization (P_z^{beam}), and the

Figure 4.18: The measured asymmetry A_{PV}^{meas} over different HWP/Wien state. When segmented into four different periods based on half wave plate and double Wien states, the A_{PV}^{meas} from individual averaging periods still showed reasonable agreement with each other. Each averaging period is a collection of slugs which in turn are aggregates of data-taking runs. The (χ^2 value)/(number of slugs) for the In/Left, Out/Right, In/Right, and Out/Left periods were 46.9/27, 16.0/21, 18.3/19, and 31.6/29 respectively [Paschke et al., 2021]. So, the reduced χ^2 values were also acceptable. Overall, the systematic effects were sufficiently suppressed across the whole experiment.

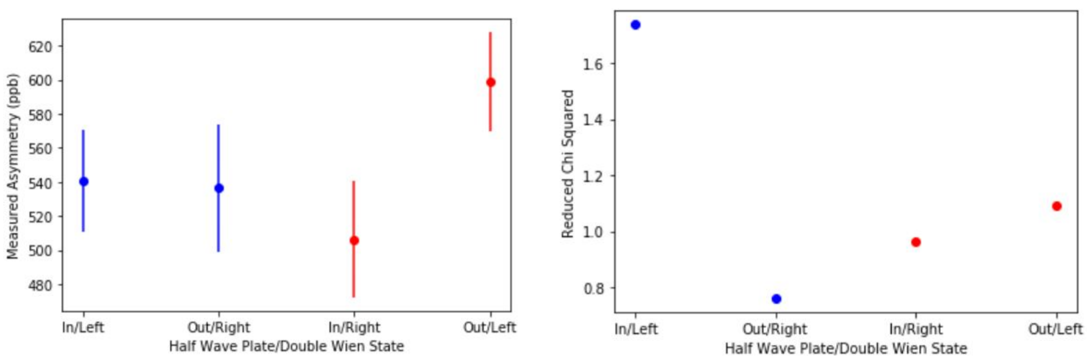

background dilutions (f_i) and asymmetries (A_i) using the following equation,

$$A_{PV}^{meas} = \frac{1}{P_z^{beam}} \frac{A_{corr} - P_z^{beam} \sum_i f_i A_i}{1 - \sum_i f_i} \tag{4.13}$$

The overall systematic correction from different sources is summarized in the table 4.3. The data for the whole experiment was segmented into four different periods based on the half wave plate and double Wien states to further verify that all systematic effects were sufficiently suppressed. The results are summarized in figure 4.18. The final measured blinded asymmetry from the entire PREX-2 data set was [Paschke et al., 2021],

$$A_{PV}^{meas} = 550 \pm 16 \text{ (statistical)} \pm 8 \text{ (systematic) ppb}$$

Table 4.3: Corrections and associated systematic uncertainty for the measured asymmetry (A_{PV}^{meas}) compared with statistical uncertainty. Reprinted with permission from the PREX collaboration [Paschke et al., 2021]. The table shows the total correction required to extract A_{PV}^{meas} and the associated systematic uncertainty with breakdown from different contributions along with the A_{PV}^{meas} and statistical error. The last column shows the relative % of the quantities listed in the middle column when weighted by the A_{PV}^{meas}.

Correction	Absolute [ppb]	Relative [%]
Beam asymmetry	-60.4 ± 3.0	11.0 ± 0.5
Charge correction	20.7 ± 0.2	3.8 ± 0.0
Beam polarization	56.8 ± 5.2	10.3 ± 1.0
Target diamond foils	0.7 ± 1.4	0.1 ± 0.3
Spectrometer rescattering	0.0 ± 0.1	0.0 ± 0.0
Inelastic contributions	0.0 ± 0.1	0.0 ± 0.0
Transverse asymmetry	0.0 ± 0.3	0.0 ± 0.1
Detector nonlinearity	0.0 ± 2.7	0.0 ± 0.5
Angle determination	0.0 ± 3.5	0.0 ± 0.6
Acceptance function	0.0 ± 2.9	0.0 ± 0.5
Total correction	17.7 ± 8.2	3.2 ± 1.5
A_{PV}^{meas} and statistical error	550 ± 16	100.0 ± 2.9

An additive blinding factor was included during data analysis in JAPAN. The blinding box was about 20 times bigger than the expected statistical error. When finally unblinded, a small blinding factor of 0.5313 ppb was found. So, essentially there was no difference between the blinded asymmetry and the final unblinded asymmetry.

4.2.7 The Calculation of ^{208}Pb Neutron Skin and Matter Density

The final measured asymmetry with the acceptance function $\epsilon(\theta)$ shown in figure 4.8 and $\langle Q^2 \rangle = 0.00616$ GeV^2 was,

$$A_{PV}^{meas} = 550 \pm 16 \text{ (statistical)} \pm 8 \text{ (systematic) ppb}$$

Figure 4.19: Comparing constraints on nuclear structure models from PREX-2, neutron star radii measurement, and gravitational wave observation. Reprinted with permission from author [Paschke et al., 2021]. The predictions of the weak charge radius (R_W) and the neutron skin ($R_n - R_p$) from a range of non-relativistic and relativistic DFT models as functions of the parity-violating asymmetry show a highly linear correlation. The asymmetry measured by PREX-2 along with the 1σ uncertainty is represented by the vertical green band. The resulting constraint on the weak charge radius and the neutron skin is shown by the horizontal green band. So, it was found that $R_W = 5.795 \pm 0.082$ (experimental) ± 0.013 (theoretical) fm and $R_n - R_p = 0.278 \pm 0.078$ (experimental) ± 0.012 (theoretical) fm.

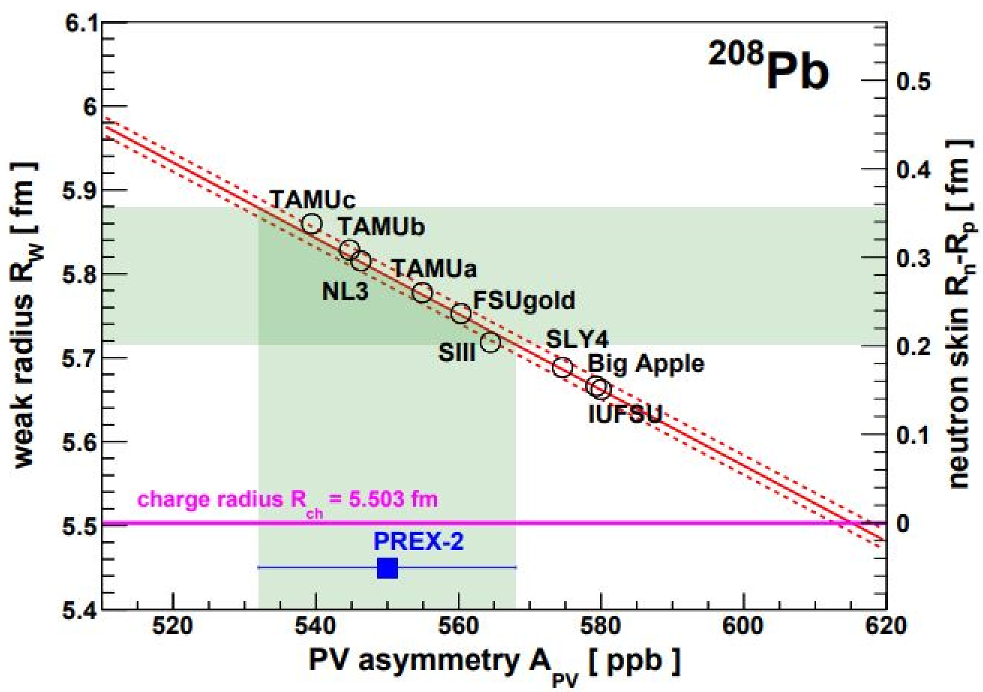

Using equation 1.2, the value of the weak form factor was calculated to be

$$F_W\left(\langle Q^2 \rangle = 0.00616\ \text{GeV}^2\right) = 0.368 \pm 0.013\ (\text{experimental}) \pm 0.001\ (\text{theoretical})$$

Model predictions for R_W is obtained for several relativistic and non-relativistic nDFT models by a two-parameter fit to the function shown in equation 2.7. Since the

Table 4.4: Combined Results of PREX-1 and PREX-2. Reprinted with permission from the PREX collaboration [Paschke et al., 2021].

^{208}Pb Parameter	Value
Weak radius (R_W)	5.800 ± 0.075 fm
Interior weak density (ρ_W^0)	-0.0796 ± 0.0038 fm^{-3}
Interior baryon density (ρ_b^0)	0.1480 ± 0.0038 fm^{-3}
Neutron Skin ($R_n - R_p$)	0.283 ± 0.071 fm

neutron and proton distributions closely approximate the nuclear weak and electric charge distributions, an estimate of the neutron skin ($R_n - R_p$) could be extracted for any particular model by taking the difference between R_W and the known electric charge radius R_{ch} with small corrections. When the R_W and $R_n - R_p$ are plotted as functions of the asymmetry, it demonstrates a highly linear relationship and the constraint from the measured asymmetry was used to constrain the above values as shown in figure 4.19. It was found that [Paschke et al., 2021],

$$R_W = 5.795 \pm 0.082 \text{ (experimental)} \pm 0.013 \text{ (theoretical) fm}$$

and

$$R_n - R_p = 0.278 \pm 0.078 \text{ (experimental)} \pm 0.012 \text{ (theoretical) fm}$$

The normalization constant ρ_W^0 could be identified as the interior weak density. It was concluded that [Paschke et al., 2021],

$$\rho_W^0 = -0.0798 \pm 0.0038 \text{ (experimental)} \pm 0.0013 \text{ (theoretical) fm}$$

With this knowledge and the knowledge of the interior charge density, the interior baryon density based on PREX-2 data was determined to be [Paschke et al., 2021],

$$\rho_b^0 = 0.1482 \pm 0.0040 \text{ fm}^{-3}$$

A more constrained estimate of all the measured quantities was obtained by combining the PREX-1 and PREX-2 measurements as outlined in table 4.4

Chapter 5

MOLLER

In this chapter, the software framework used for simulating experimental conditions and some critical design decisions made for various MOLLER subsystems are discussed. I highlight my particular contributions to the development of the software framework and results of notable studies that were used to optimize the spectrometer system, the integrating detector system, the shielding system, etc.

5.1 Research Methods

In this section, I describe my contributions towards development of simulation tools that are dedicated towards optimization of the MOLLER experimental design. I also describe how they are used in our simulation studies.

5.1.1 Remoll-A Geant4 Monte Carlo Simulation for MOLLER

Remoll is a Monte Carlo simulation [Riordan et al., 2013] developed with the Geant4 software toolkit for simulating passage of particles through matter. The advantage of using Geant4 is the flexibility to define any custom experimental geometry with Geometry Description Markup Language (GDML) and simulating particle

Figure 5.1: Visualization of the MOLLER experimental geometry in Remoll. The image shows the current status of implemented experimental geometry in Remoll. I made direct contributions towards implementation of the components highlighted in green.

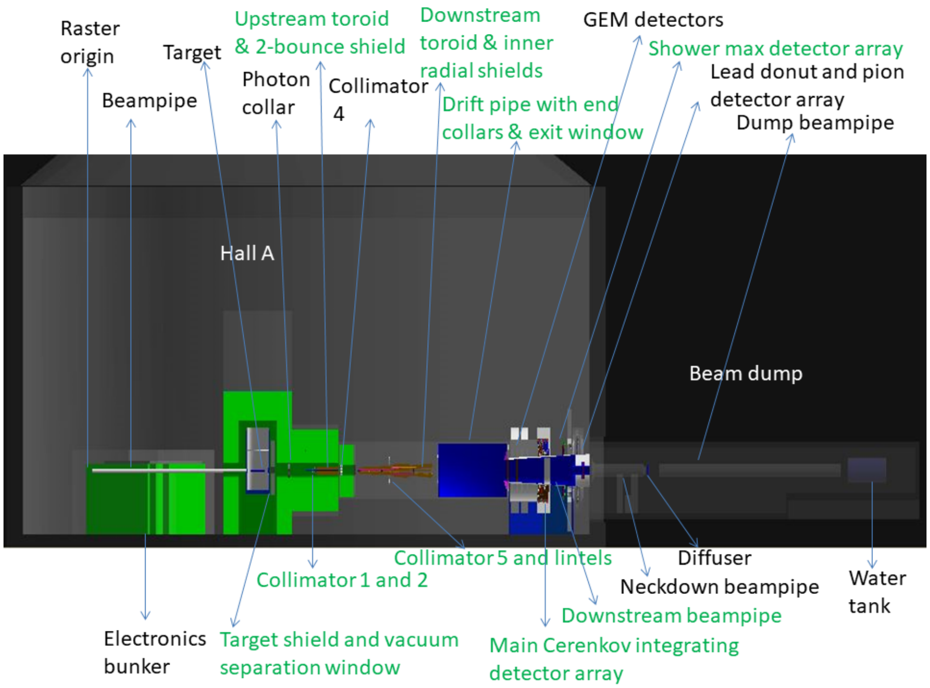

navigation through the geometry subject to user-defined force fields and realistic interactions modeled within Geant4 physics lists [Apostolakis and Wright, 2007]. The results of the simulation are stored in a ROOT (an object-oriented framework for data analysis [Brun and Rademakers, 1997]) tree data structure. I contributed to the parametrized implementation of important components within the simulation geometry including the main detector array, the shower max detector array, the toroidal spectrometers, etc. I also contributed to the post-processing of magnetic field maps, developed by fellow collaborators, to a format that is readable by Remoll. In addition, I developed scripts to analyze the output ROOT trees for various studies.

The figure 5.1 shows the current simulation geometry implemented within Remoll. Most of the critical experimental components are shown including the target chamber, the collimators, the spectrometers, the detector arrays, the beampipes in various regions, and the beam dump. However, the simulation geometry still lacks description of engineering support structures. In addition to real components, virtual detector planes may be used along the beamline to track particle distributions depending on the study.

Figure 5.2: Remoll GDML generator of the main detector array. The image shows the parametrization framework of the main detector array generator [Clarke et al., 2017]. A CSV file with ring-level parametrization is fed into a perl script that produces a CSV file with individual detector-level parametrization and a text file that can be read into CAD. The CSV file is then fed into the main GDML generator which produces the GDML and XML files that need to be copied into the Remoll geometry folder to load in the simulation. The advantages of the framework are simplicity of GDML description requiring less compute resource and time, flexibility of use in complimentary applications such as optical physics simulations, and uniformity with CAD model. A notable limitation is the absence of realistic support structure in the parametrized model.

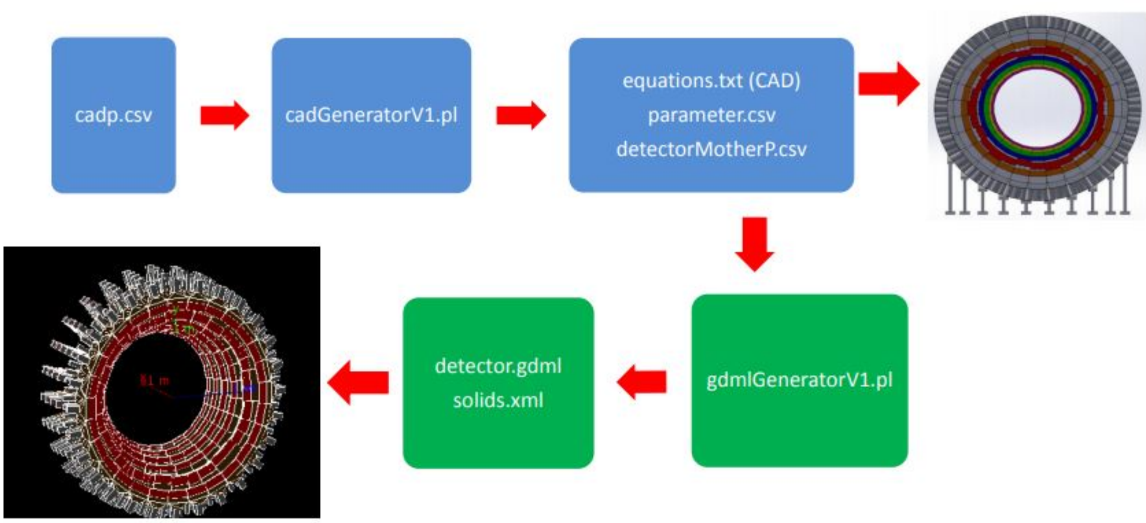

Till now, we have used a virtual plane at the location of the main detector for most main detector-related studies. I significantly contributed towards implementing a generator [Clarke et al., 2017] that can be used to produce a detector array for more advanced studies in the future such as determining the level of cross-talk between individual detectors and more realistic background simulations. The generator was written in perl programming language. As shown in figure 5.2, the generator framework can take a CSV file with a list of parameters as input and produce a GDML file readable by Remoll and a text file readable by CAD. This approach was taken to maintain uniformity between the CAD model of the detector array and the simulation geometry. Other approaches of translating geometries directly to GDML from CAD were not viable due to the anticipated large compute resource usage and long simulation times. The added advantages of the generator approach include the flexibility to turn on optical physics functionality when necessary and the ability to make changes at the level of individual detectors to understand the effect of detector offsets.

I also implemented a similar generator in python for the shower max detector array with only ring-level parametrization and the scope to add additional functionality in the future [Rahman et al., 2021a]. The shower max detectors can be a significant source of backscattered background radiation on the main detector. Hence, it was necessary to have a realistic description with a close approximation of the total material budget for this component.

Another important contribution was the development of the parametrized spectrometer magnet coil generators [Rahman et al., 2021b]. Figure 5.3 shows examples of generated coils in simulation. An accurate description of the coils is required in simulation because we want to estimate the heat load and radiation dose for different field configurations and apply constraints to avoid failures during experimental running. The parametrization allows us to move the coil physically in simulation and change dimensions easily for the above purpose. A notable limitation of the current parametrization is the inability to separate the coil insulation from inner support even though they are slightly different materials. There is a plan to implement this feature in the near future.

Figure 5.3: Visualization of the upstream toroid (left) and the downstream toroid (right) generated with Remoll coil generator.

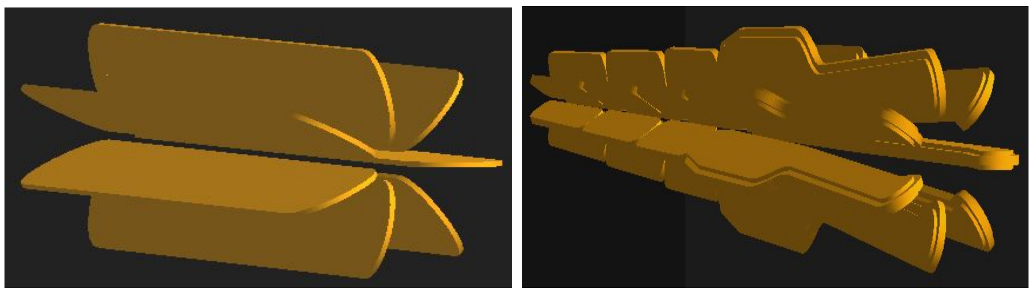

Apart from the above components, I also contributed to the implementation of different beampipes, shielding, and collimators along the beamline in Remoll geometry. An equally important task was the post-processing of magnetic field maps developed in TOSCA (software package to design 3D electromagnetic fields [Vector Fields Inc, 2012]) to a text format that is readable in Remoll. The field maps are necessary to simulate accurate particle navigation. We tested many different spectrometer configurations for various sensitivity and design optimization studies. I contributed towards making the field maps quickly available for use in Remoll [Rahman et al., 2021c]. Lastly, I developed many analysis scripts for various studies to visualize particle distributions at specific locations. For each event in the simulation, a collection of hits is recorded across the sensitive detectors and stored in the output ROOT tree. A hit is a snapshot of a particle at a moment of time containing information like current position, momentum, unique track id, etc. and similar information at its origin. We can extract the information of interest by looping through the events and hits and applying specific cuts or conditions. The basic structure of a remoll analysis macro is shown below.

```
// Load remoll output file and get tree containing simulation results.
TFile *fileName = new TFile("remollout.root");
```

```
TTree *Tree = (TTree*) fileName->Get("T");
// Initialize a collection of hits and link it to the hit branch.
std::vector < remollGenericDetectorHit_t > *fHit = 0;
Tree->SetBranchAddress("hit", &fHit);
// Loop through all events.
// Each event corresponds to a primary particle and all associated secondary tracks.
for (size_t j = 0; j < Tree->GetEntries(); j++){
// Load the hit collection corresponding to event j
// and loop through all hits in the collection.
  Tree->GetEntry(j);
  for (size_t i = 0; i < fHit->size(); i++){
// Load the hit i corresponding to event j.
// The hit is the snapshot of a particle at a sensitive detector.
    remollGenericDetectorHit_t hit = fHit->at(i);
    if (hit.pid == 11 && hit.mtrid == 1){
// Perform tasks like filling custom histograms subject to cuts or conditions.
    }
  }
}
```

So far, I have described my contribution towards addition of important features in the Remoll simulation. In the next section, I describe my contribution towards developing an efficient workflow for actually running the simulation on parallel clusters. This was helpful to increase productivity and useful for new members in the collaboration to get started without thinking about simulation intricacies.

5.1.2 Simulation Parallelization and High Performance Computing

One of the requirements to get accurate results with Monte Carlo simulation is the accumulation of large amount of statistics. A single iteration of Remoll for 100 million events consumes ≤ 3 core years (CYs) and ≤ 8 TB storage. This can fluctuate depending on the complexity of the geometry and the number of sensitive detectors in the simulation. Multi-threading in Remoll allows us to use the parallelization offered by high performance computing (HPC) clusters that can meet those resource requirements. I contributed towards the procurement of compute resources by developing a parallel job submission workflow and helping to complete the Compute Canada Resource Allocation Competition application by providing estimates of compute resources required for our studies. MOLLER has received $\sim$ 170 Core Years (CYs) allocation on the Compute Canada Beluga cluster for both 2020 and 2021. The allocation on Beluga has been instrumental in fast-tracking our design process as we can perform many iterative design studies simultaneously. Apart from the Beluga cluster, we also use the legacy GREX cluster at the University of Manitoba and the Ifarm cluster at the Jefferson Lab. Slurm is the common workload manager and scheduling software used for parallel job submissions on these HPC clusters. I developed python scripts to submit slurm array jobs for Remoll simulation and analysis on the clusters [Rahman, 2021].

The simulation results need to be anchored to real world data. In the next section, a couple of studies are described that confirm the veracity of various aspects of our simulation.

5.1.3 Simulation Benchmarking

A single detector generated with the main detector generator was used to run optical simulations with the Cherenkov process turned off and to observe the scintillation light yield with the electron beam being incident at various angles on the light guide. As shown in figure 5.4, the results were compared with a similar angular scan using Qsim [Clarke, 2020a], a standalone Geant4 optical physics simulation, benchmarked against a beam test at the Mainz Mikrotron [Riordan et al., 2018]. Figure 5.5 shows the simulated photoelectron yield spectrum for a single electron hitting the Quartz that was also compared with data from a beam test at the Stanford Linear

Figure 5.4: Comparison of average photoelectron yield from light guide angular scans between Remoll and benchmarked Qsim simulation. Reprinted with permission from author [Clarke, 2020a]. With the Cherenkov process turned off, only the scintillation yield in air light guides from angular scans were compared between Remoll and Qsim [Clarke, 2020a], a Geant4-based optical physics simulation benchmarked against a beam test at the Mainz Mikrotron [Riordan et al., 2018]. No appreciable differences were found for a range of reflectivity values of the light guide material, taking into account small differences in geometric design.

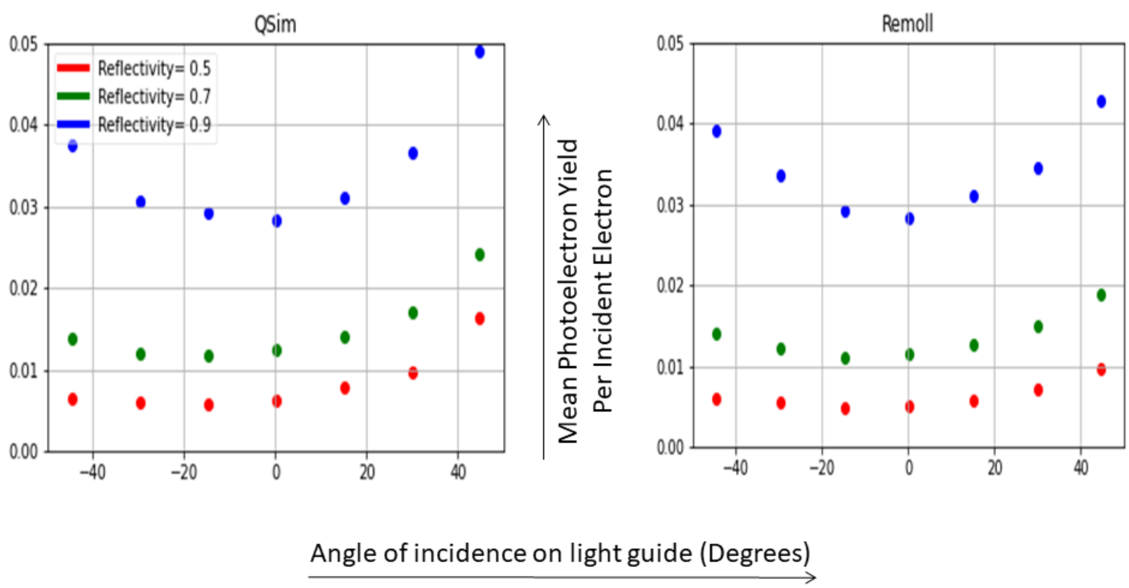

Accelerator (SLAC) [Clarke, 2019]. No appreciable differences were found in either case with minimal difference in detector geometry which gives us confidence in the current simulation implementation of the main detector in Remoll. As mentioned before, the advantages of using the parametrized detector model in Remoll is that the detector parameters are easily modifiable and the simulation is scalable to the full detector array. This requires no recompilation of Remoll.

In terms of radiation dose calculations, a useful crosscheck can come from the

Figure 5.5: Simulated photoelectron yield spectrum for a single electron hitting the quartz of a generated Remoll main detector. Reprinted with permission from author [Clarke, 2019]. Preliminary results from a beam test at the Stanford Linear Accelerator showed good agreement with the simulated spectrum [Clarke, 2019].

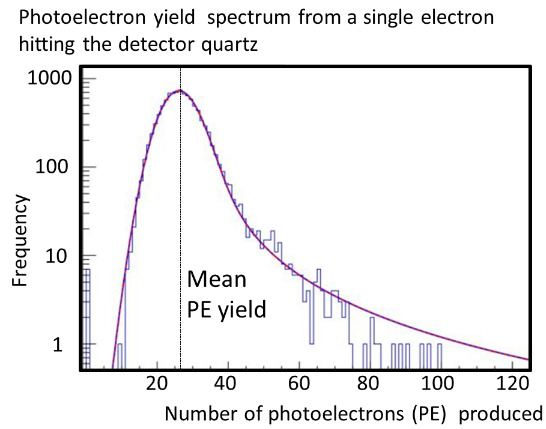

hall boundary high-energy neutron dose estimates done for PREX-2. The simulation estimate for high-energy neutron dose exiting through the roof of the experimental hall A was $0.9 - 2.2$ mrem/yr for PREX-2. Over the course of the experiment, a dose of 1.24 mrem/yr was measured with radiation monitors surrounding the hall [Rahman, 2020]. Since Remoll uses the same Geant4 framework for dose estimates, the estimates for MOLLER can be considered reliable.

Since Geant4 physics libraries are continuously updated to fit the latest experimental results from various sources and apply bug-fixes to the engine, we perform checks to monitor any significant changes in remoll output when a new Geant4 version comes out. We have noticed virtually no changes in our detector rate estimates transitioning from Geant4/10.4 to Geant4/10.6. However, Geant4 ≥ 10.6 should be used for optical physics simulations with Remoll because of a limitation in previous versions which prevented parallel world geometry and optical physics features from being used simultaneously. We use virtual planes in the parallel world for particle tracking in our simulations and optical physics simulations are an important part of our detector studies. So, the choice of the Geant4 version does matter.

5.2 Critical Design Optimization Studies and Results

In this section, I describe the results of some critical design optimization studies that I performed for various MOLLER subsystems using some of the tools described in section 5.1.

5.2.1 Spectrometer System

Figure 5.6: Sectorwise 1D radial rate distributions at the detector plane 26.5 m from target. The image shows the radial rate distributions for ee and ep in open, closed and transition sectors overlaid along with the distributions for all sectors combined. The spectrometer aims to provide sharp focus for the individual ee and ep peaks and good separation between them.

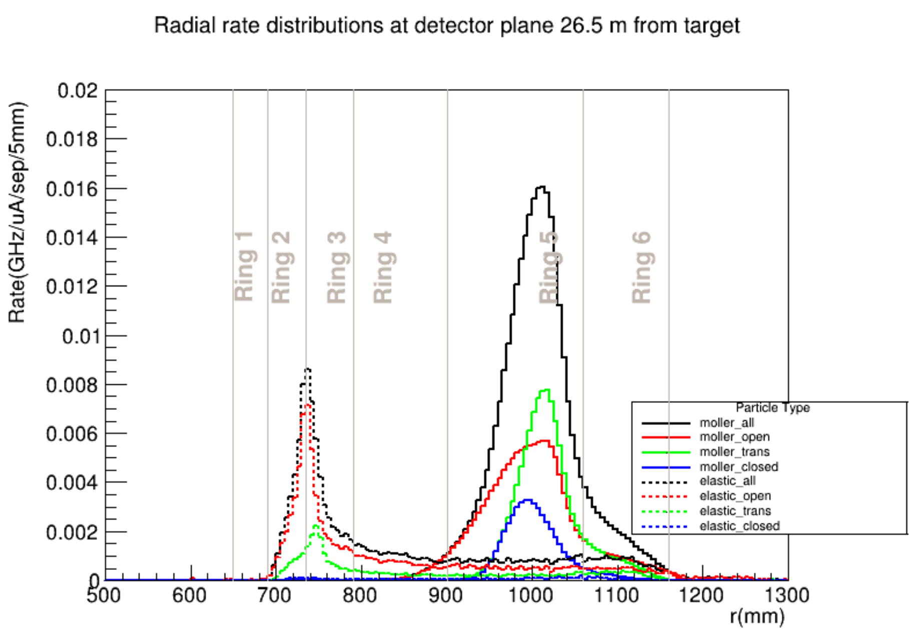

Figure 5.7: Main electron-electron (ee) scattering signal and elastic electron-proton (ep) scattering background distributions at the detector plane 26.5 m from target. The image shows that the spectrometer system focuses the main electron-electron scattering signal onto ring 5 of the main detector array which has 6 rings in total. The elastic electron-proton scattering background distribution is also shown centered around ring 2 and 3 to demonstrate the kinematic separation provided by the system. Each ring can be divided into seven azimuthal septants since the spectrometers have seven-fold symmetry. In all rings, each azimuthal septant is divided into 3 sectors while ring 5 has additional segmentation. The center of the septant belong the open sector (red), the edges close to the conductors belong to the closed sector (blue) and the remaining regions belong to the transition sector (green).

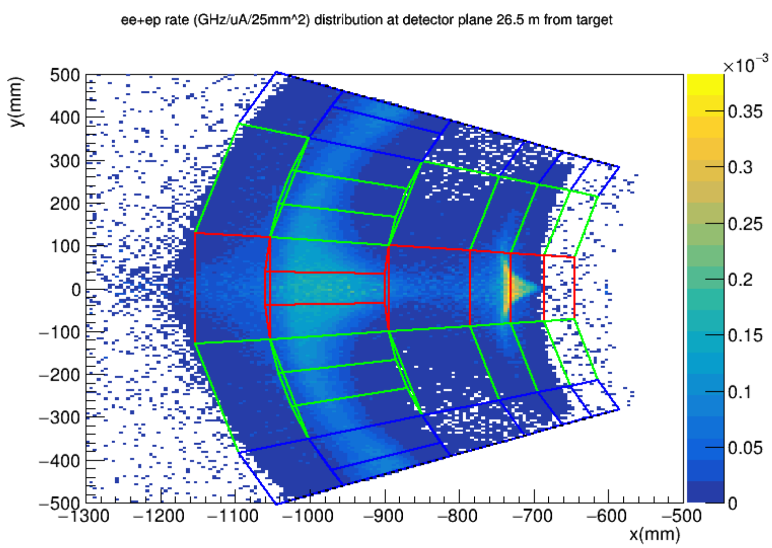

The spectrometer system performs the important task of separating the main electron-electron (ee) scattering signal for MOLLER from backgrounds such as electron-proton scattering in the liquid hydrogen target, electron-Al nucleus scattering in the target can, photons, pions, neutrons, etc. As shown in figure 5.7, the spectrometer focuses the particles onto 6 rings of the main detector array, with the ee peak centered on ring 5. In contrast, the elastic electron-proton background (ep) distribution is centered around ring 2 and 3. Figure 5.6 shows the 1D radial distributions of the ee and ep in different azimuthal sectors. The other backgrounds are not shown. I performed studies to define various types of design tolerances for the spectrometer system.

Figure 5.8: Radial position tolerance of a single coil in the downstream toroid. The tolerance is calculated by multiplying the inverse of the slope of change in the ee mean asymmetry in ring 5 with various offsets from nominal radial position (estimated with Bayesian analysis) and 0.1 ppb allowed uncertainty in asymmetry. Controlling the uncertainty to 0.1 ppb for each type of offset including the radial offset will make it possible to constrain the total uncertainty to be under 0.7 ppb.The image implies that an individual coil in the downstream toroid can be offset by $\pm\|\frac{0.1}{-0.03}\| \sim \pm 3$ mm radially without affecting the optics alignment. However, the tolerance on the inner radius is smaller due to space constraints.

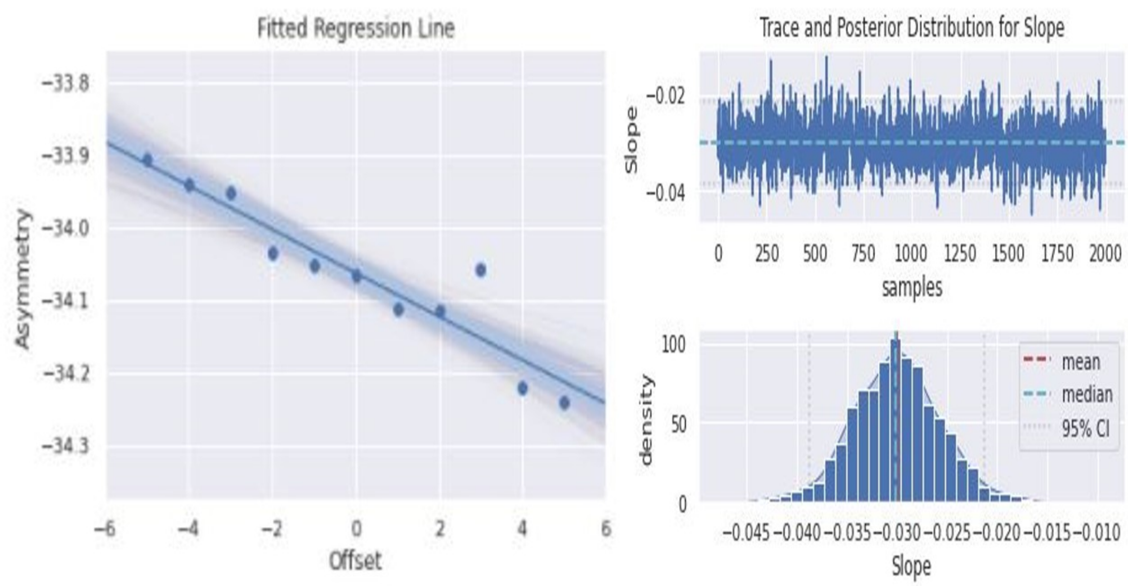

Firstly, I discuss the position tolerances which are defined by the asymmetry distribution corresponding to the ee rate in ring 5. Assuming a fixed detector tiling, I determined the position tolerances for the spectrometer coils with regards to optics. As shown in figure 5.8, I first calculated the slopes of the change in mean asymmetry for ee in ring 5 with respect to various values of offsets in radial position, azimuthal position, position along the beam line, roll angle, pitch angle, and yaw angle of a single coil in the upstream and downstream toroid separately. To control the total uncertainty in asymmetry to under 0.7 ppb for single-coil offsets, we allow 0.1 ppb uncertainty in asymmetry for each type of offset. The tolerances were calculated by multiplying the inverse of the slopes with the allowed uncertainty of 0.1 ppb in the mean asymmetry. It was found that the most stringent constraint came from radial offset tolerance in the hybrid coil. The following set of constraints were adopted as the optics tolerances for both upstream and hybrid coils:

± 25 **mm in position along the beamline,** 3 **mm radially outward and** 1 **mm radially inward,** ± 3 **mm azimuthally on the outer radius and** ± 1 **mm azimuthally on the inner radius.**

Within these deviations from nominal coil positions, the optical alignment provided by the spectrometer system will not be affected significantly. Worst case iterations of the toroid configurations, simulated to test multiple coil offsets, did not show a change in mean asymmetry beyond the bounds set by the tolerance. This hints at cancellation from anti-correlated slopes of different coils in the toroids.

The optical alignment is not the only aspect that could be affected by offset coils. Only a small portion of the electron beam actually interacts in the target and the rest needs to be propagated safely down to the beam dump. This is to prevent irradiation of any component that unintentionally interacts with the beam. Offset coils can result in significant dipole fields at the center of the spectrometers, more prominently in the downstream case. This can cause the central beam to be steered radially outward in any particular direction. A possible location of interference could be the neckdown beampipe in the dump which has a radius of 200 mm. As shown in figure 5.9, I tested a few different coil configurations within the optical tolerances and calculated the incident power at the dump entrance.

Figure 5.9: Incident power distributions at the beam dump entrance for nominal and offset coil configurations. Dipole field at the center of spectrometers enhanced by offset spectrometer coils can steer the beam radially outward. A possible location of unintended irradiation could be the neckdown beampipe in the dump with 200 mm radius. I tested a few different configurations and demonstrated that a significant amount of power was not incident at the dump entrance above 200 mm radius in any case. The case 3 is the most likely deviation from nominal and case 1 is the hypothetical very worst case scenario.

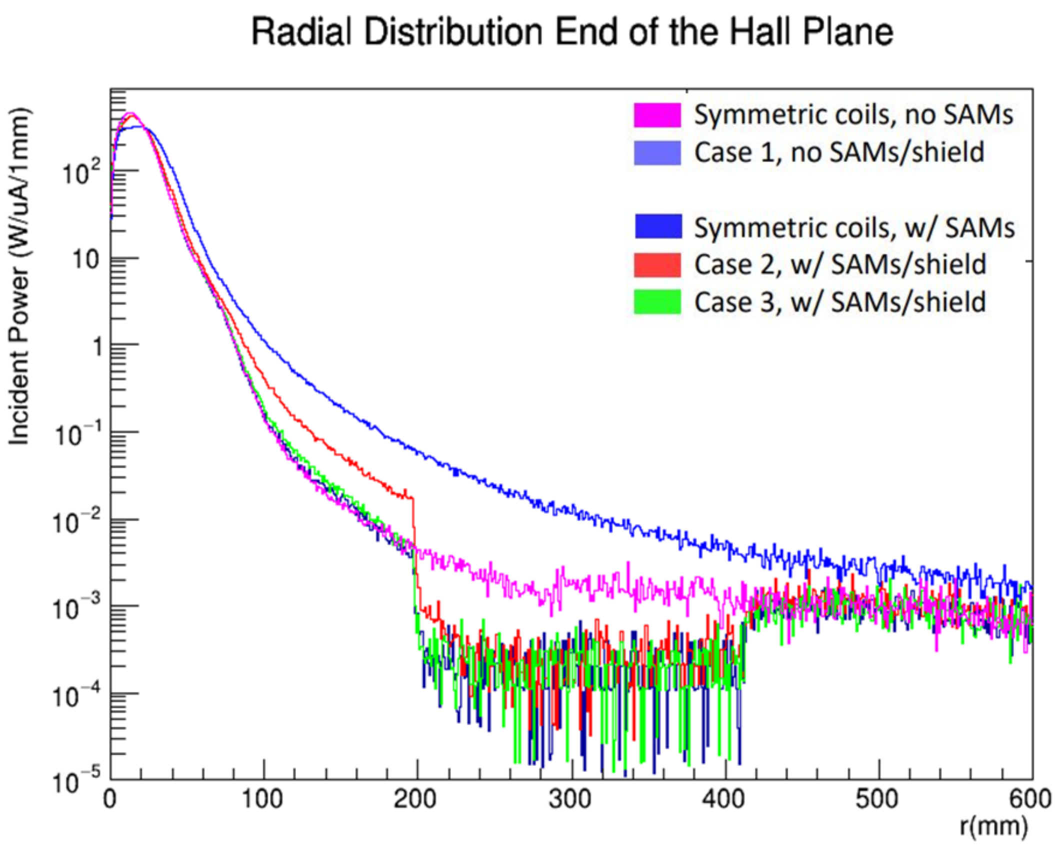

The most realistic offset configuration which includes some cancellation due to the randomness of dipole orientation in different septants only deposits around 14.2 W between 200 and 600 mm radius at the dump entrance compared to 13.4 W in the nominal case. It should be noted that power is somewhat suppressed by a lead shield near the dump that protects small angle monitors (SAMs). Without this shield, the incident power in the symmetric case is around 39.3 W in the $200 - 600$ mm radius region. In the very unrealistic case where this shield is taken out and the dipoles in all the septants are maximized in one particular direction, the incident power in that region is 260 W. So, only a negligible fraction of the total beam power of 715 kW affects that region. Most of the beam stays well within the 200 mm radius of the neckdown beampipe. So, the defined tolerances also ensure clean transport of the beam to the dump.

Figure 5.10: Power deposited in the copper conductor of individual coils in the upstream (left) and downstream (right) spectrometers. The total power deposited in a single upstream spectrometer conductor is 4 W. The total power deposited in each of the 4 segments of a single downstream spectrometer conductor is 1.4 W, 0.4 W, 0.6 W and 0.9 W respectively. The total power deposited in all the conductors of the spectrometer system is 51.1 W. Although this is below the threshold of 100 W, further detailed studies are necessary to ascertain whether we need a closed cooling system that provides continuous cooling for the conductors.

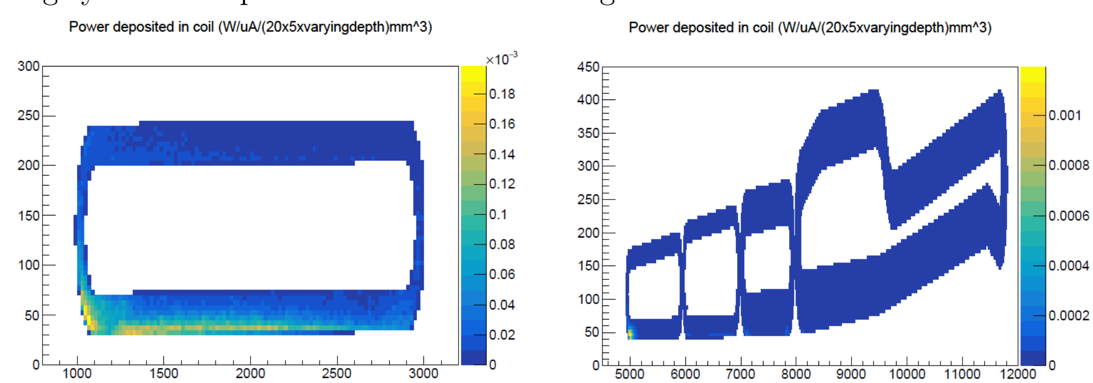

As shown in figure 5.10, I also determined the power deposited in the copper conductors of the spectrometer system for the nominal case to estimate the cooling requirements. If the total power deposited in all the copper conductors of the spectrometer system is more than 100 W, a closed cooling system may be necessary which provides continuous cooling for the conductors. The total power deposited in all the conductors was found to be 51.1 W for the nominal case. However, preliminary studies with the hypothetical very worse case scenario showed a power deposition of ~ 60 W in the downstream spectrometer alone. So, further studies are required to assess the cooling requirements of the conductors.

Figure 5.11: Power deposited in the epoxy insulation and inner G10 support of the individual coils of the upstream (left) and downstream (right) spectrometers. The deposited energy over the life time of the experiment is divided by the mass of the material in any particular pixel to obtain the radiation dose at that point. The maximum doses in an upstream coil epoxy and the four segments of an downstream coil epoxy are 51, 70, 34, 41, and 22 MGy respectively. Again, although these values are below the 100 MGy threshold for safety in nominal case, additional studies need to be performed to ensure that they are under control for the offset coil case as well. The maximum dose in the inner G10 support for the upstream coil is about 24 MGy and for the downstream coil is about 7.4 MGy. These also need to be suppressed with further optimization such as better shielding and less area coverage for the supports.

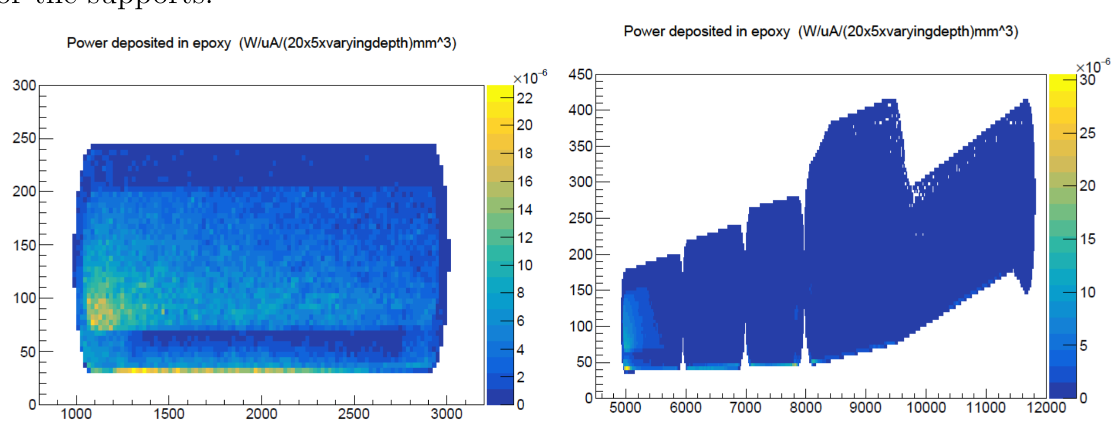

Figure 5.12: Radial dose calculation for a downstream toroid coil epoxy insulation and inner G10 support. The deposited power assuming a 65 μA current is multiplied by the duration of the experiment (344 days) to get the total deposited energy and then divided by the mass of the material in any particular pixel to obtain the radiation dose at that point. To calculate the mass, I assume a density of 1.3 g/cm^3 for the insulation and support although they are both slightly different materials. The volume mapping in the bottom left shows that the insulation is a shallow covering wrapping the conductor while the support region in the middle is as thick as the conductor at any point. So, the mass per pixel varies as well.

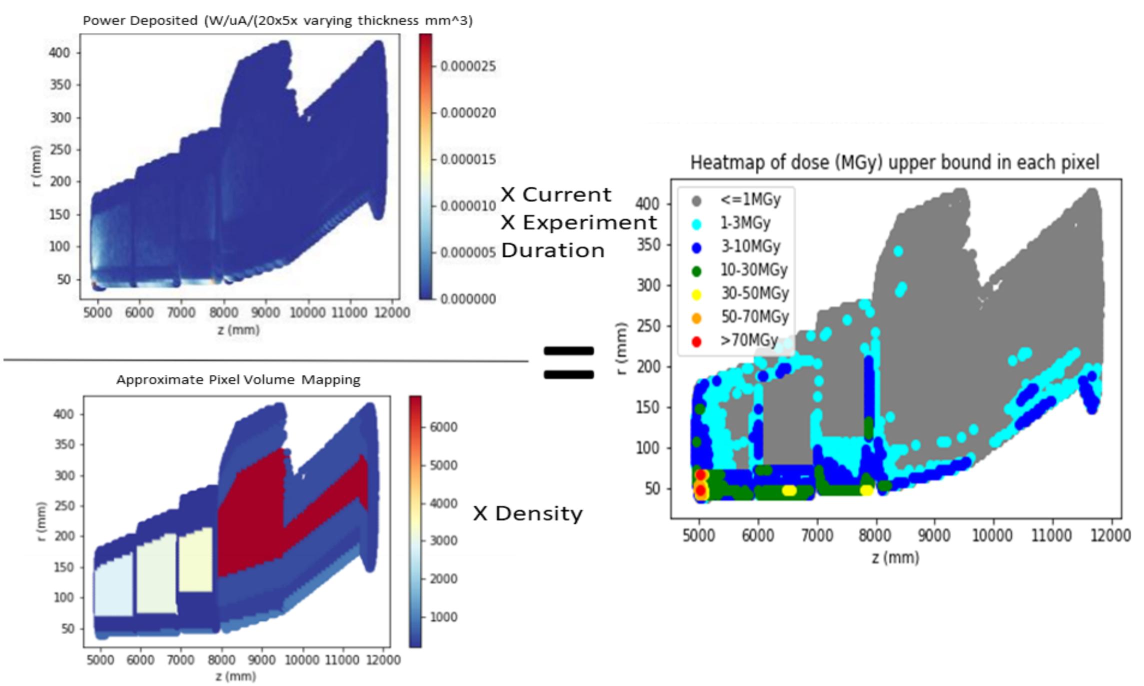

In addition, I calculated the radiation dose deposited in the epoxy insulation and G10 inner coil support to assess the probability of radiation damage. The threshold for damage in the epoxy insulation is about 100 MGy and the threshold for damage in the inner support is about 10 MGy. The radiation dose is calculated by dividing the energy deposition over the life time of the experiment at any particular pixel by the mass within that pixel. I show a sample calculation for the downstream toroid in figure 5.12. The doses per coil are summarized along with the power deposition for both spectrometers in figure 5.11. The radiation doses are mostly under control for the nominal coil configuration. However, further studies are needed to optimize the shielding to handle offset coil cases.

Apart from these studies, I also performed a phase space study to determine the optimal field strength required in the spectrometer coil segments [Mammei, 2019]. In another study, I compared the capacity to extract the physical asymmetry when using the current segmented coil design versus a hybrid coil design for the downstream case and demonstrated that they are equivalent from a physics perspective. The segmented design was chosen for ease of construction [Fair et al., 2020b]. In the next subsection, I discuss in depth the design studies that I performed for the main detector system and the analytical technique of deconvolution which we use to extract the physical asymmetry.

5.2.2 Main Detector System

In this subsection, I discuss the main background processes that effect the Møller (ee) asymmetry measurement. I also discuss the deconvolution analysis method to extract the signal and background contributions to measured asymmetry in all the detectors in the main detector array simultaneously with a least squares fitting method and demonstrate an example calculation. The code for the deconvolution analysis was developed by Yuxiang Zhao and Ciprian Gal from Stonybrook University [Zhao, 2015]. I developed a technique to come up with an initial optimal guess for the detector tiling in the main detector array that has a direct impact on the deconvolution analysis.

The distribution of the physics backgrounds that most concern us are shown in figure 5.13. Neutral backgrounds like neutrons are sufficiently suppressed by shielding and although there is a considerable photon flux at the detector plane, it does not amount to a significant background in terms of photoelectrons produced in the main detectors [Lee, 2021]. For now, the background contributions from particles hitting the lightguides are also ignored.

Figure 5.13: Radial signal and main background distributions at detector plane 26.5 **m from the target**. The target region is the dominant source of backgrounds that effect the Møller asymmetry extraction using deconvolution. The neutral backgrounds (neutrons, photons, etc.) are not shown because they do not significantly effect the asymmetry extraction via deconvolution.

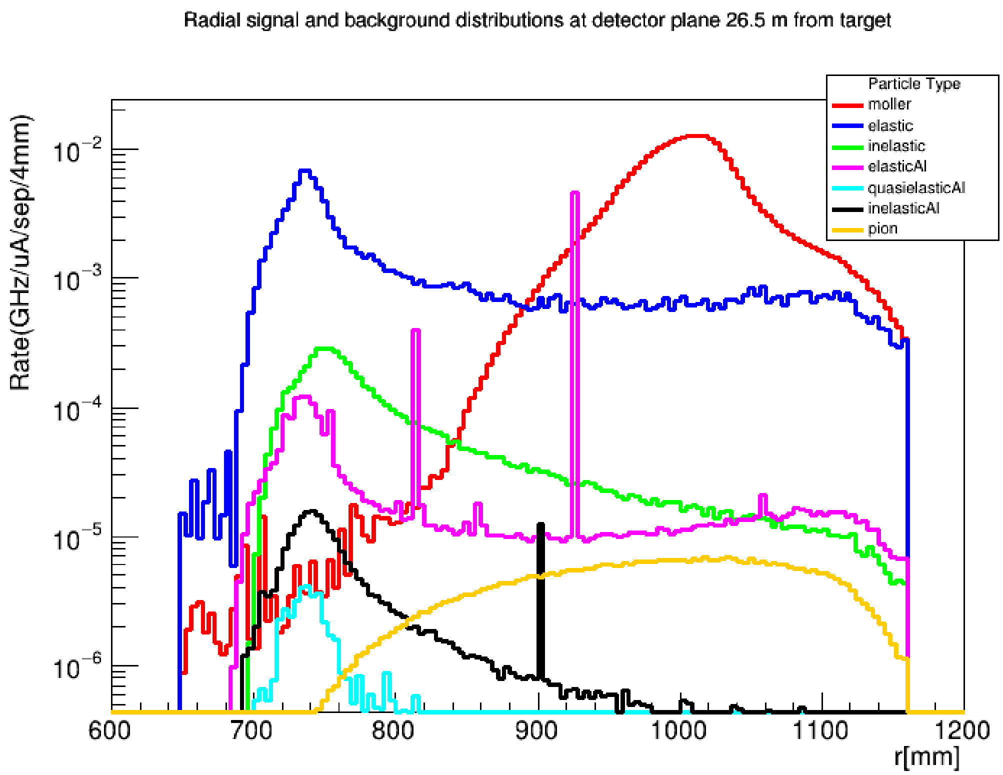

With these assumptions, the total asymmetry that is measured in any detector i in the main detector array is actually a sum of the dilution weighted asymmetries of all the different types of particles in the quartz tile as shown below

$$A_i^{meas} = \sum_j f_{ij} A_{ij} \tag{5.1}$$

where $f_{ij} = \frac{rate_{ij}}{\sum_j rate_{ij}}$ is the dilution in the tile i with respect to particle $j =$ ee, elastic ep, inelastic ep (from three different kinematic regions), elastic eAl, etc.

Figure 5.14: Dilution weighted signal and main background asymmetry distributions at detector plane 26.5 **m from the target**. Although the inelastic processes have less rate, they have a higher associated asymmetry. The three different kinematic regions of the inelastic distribution also contribute different asymmetries which needs to be taken into account in our choice of detector ring boundaries.

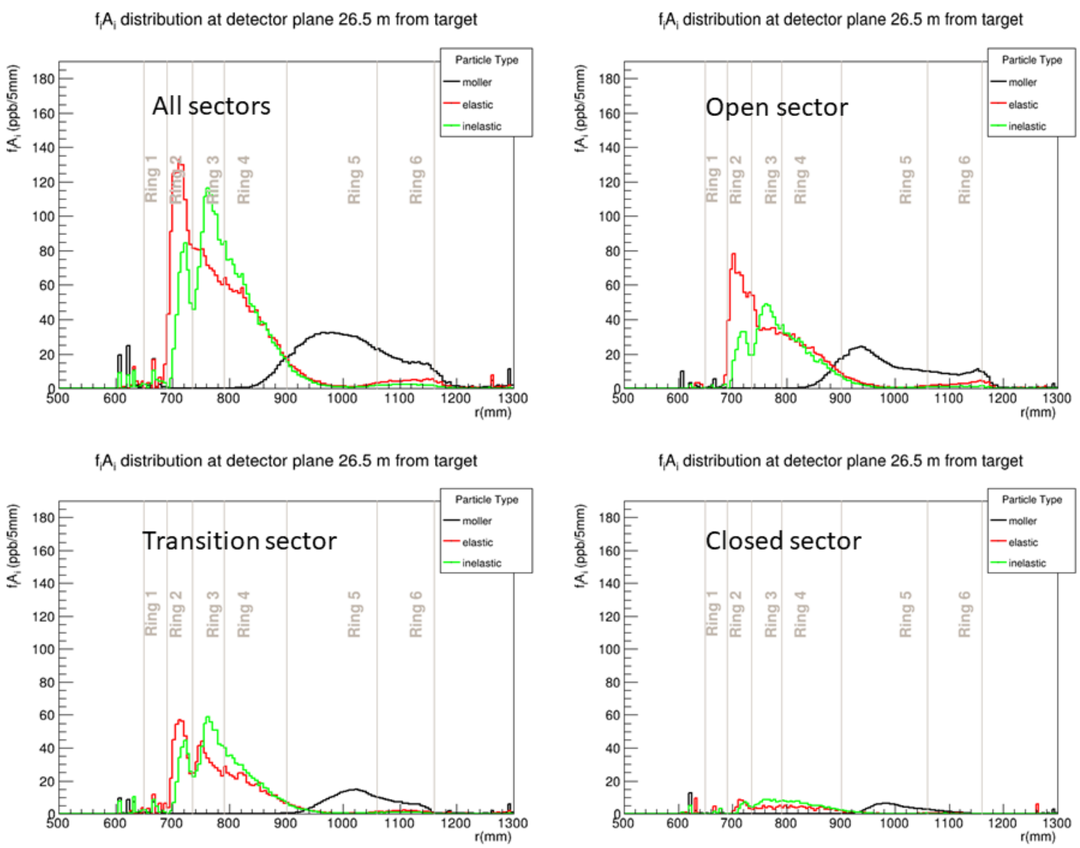

Table 5.1: Main detector ring boundaries used for deconvolution analysis.

Ring	Lower Radius (mm)	Upper Radius (mm)
1	650	690
2	690	735
3	735	790
4	790	900
5	900	1060
6	1060	1160

Table 5.2: Extracted asymmetry and uncertainty with the deconvolution technique in ring 5 **open sector.**

Name	Asymmetry [ppb]	Uncertainty [ppb]	Relative Uncertainty [%]
ee	-34.86	0.75	2.16
ep elastic	-22.27	1.43	6.42
ep inelastic $W = 1 - 1.4$ GeV	-614.26	94.95	15.46
ep inelastic $W = 1.4 - 2.5$ GeV	-596.50	52.91	8.87
ep inelastic $W = 2.5 - 6$ GeV	-462.68	113.97	24.63

To apply the deconvolution technique and extract individual asymmetries, I chose a detector tiling configuration by looking at the dilution weighted asymmetries for the Møller, elastic ep, and inelastic ep distributions. As shown in fig 5.14, the basic principles of choosing tile definitions are designing ring 1 to have minimal contribution which will be used as a large angle monitor for alignment, adjusting the ring 2,3, and 4 boundaries to sufficiently segment the inelastic ep distribution into three distinct kinematic regions with two peaks and a continuous tail, and tweaking the ring 5 boundary to maximize the dominance of ee peak. For the purpose of the deconvolution study, the additional segmentation in ring 5 is ignored and I choose a consistent tile definition across all azimuthal bins in a certain ring. Future studies will be aimed at studying the benefits of azimuthal staggering of detectors. The current detector ring

Table 5.3: Contribution of dilution weighted signal and main background asymmetries to measured asymmetry in each detector. The charged secondaries (positrons and pions) generated after the target region are also included in this analysis. Only the asymmetries corresponding to Møller (ee), ep elastic(ep), ep inelastic $W = 1 - 1.4$ GeV (inW1), ep inelastic $W = 1.4 - 2.5$ GeV (inW2), and ep inelastic $W = 2.5 - 6$ GeV (inW3) are used as free parameters in our deconvolution analysis. The rest of the backgrounds are constrained by previous experimental results.

i	ee $\frac{f_i * A_i}{A_i^{meas}}$ [%]	ep $\frac{f_i * A_i}{A_i^{meas}}$ [%]	inW1 $\frac{f_i * A_i}{A_i^{meas}}$ [%]	inW2 $\frac{f_i * A_i}{A_i^{meas}}$ [%]	inW3 $\frac{f_i * A_i}{A_i^{meas}}$ [%]	eAl $\frac{f_i * A_i}{A_i^{meas}}$ [%]	quasiAl $\frac{f_i * A_i}{A_i^{meas}}$ [%]	inAl $\frac{f_i * A_i}{A_i^{meas}}$ [%]	pion $\frac{f_i * A_i}{A_i^{meas}}$ [%]
1C	31.0	40.1	15.2	13.6	2.5	-5.0	0.0	-1.1	3.8
1T	30.5	39.3	17.7	14.2	2.6	-6.3	0.0	-1.2	3.3
1O	31.7	42.4	15.1	18.5	2.6	-11.9	0.0	-1.6	3.2
2C	3.4	51.8	30.7	17.3	0.2	-2.0	0.0	-1.9	0.5
2T	1.1	57.8	31.7	14.5	0.1	-3.2	0.0	-2.0	0.1
2O	0.6	82.0	24.8	10.6	0.0	-15.8	0.0	-2.2	0.1
3C	3.0	36.2	23.7	36.9	2.7	-1.9	0.0	-1.8	1.1
3T	1.0	50.0	26.1	29.8	1.1	-6.2	0.0	-2.1	0.4
3O	0.5	61.5	26.8	25.5	0.7	-13.1	0.0	-2.2	0.2
4C	8.4	35.6	14.1	20.1	15.9	-3.9	0.0	-1.1	11.0
4T	5.2	43.7	14.0	26.6	12.2	-6.1	0.0	-1.3	5.7
4O	12.4	49.8	12.1	26.4	7.8	-10.3	0.0	-1.3	3.2
5C	79.1	7.9	2.6	2.7	2.0	-1.3	0.0	-0.2	7.1
5T	81.2	8.9	2.3	2.6	2.3	-1.7	0.0	-0.2	4.7
5O	86.0	8.5	1.6	1.8	1.9	-2.0	0.0	-0.2	2.3
6C	55.8	20.4	6.3	6.1	2.6	-3.6	0.0	-0.5	13.0
6T	62.7	17.6	4.6	4.4	2.6	-3.8	0.0	-0.4	12.3
6O	67.8	19.1	3.4	3.5	3.0	-5.2	0.0	-0.3	8.7

boundaries used for this calculation are shown in table 5.1. With the boundaries of 18 (6 rings and 3 azimuthal sectors per ring) tiles on the detector plane well-defined, the simulation gives us the relative contributions of different processes to measured asymmetry for all the tiles as shown in table 5.3. After that, I perform a least squares fit using the deconvolution algorithm [Zhao, 2015] to extract the unknown asymmetries in each tile. The technique assumes that the kinematic evolution of the asymmetry for a process is known as a function of detector location. The result for ring 5 open sector is presented in table 5.2 where the Møller peak is dominant. The relative uncertainties quoted are actually constant for all tiles although the absolute values may change across tiles. The 2.16% relative uncertainty on the ee asymmetry implies a 2.16% relative uncertainty on the electron weak charge measurement. So, the technique shows promise in meeting our precision goals although further optimization needs to be done.

So far I have limited the discussion to the optimizations needed to deal with backgrounds that effect the asymmetry extraction by main detector. In the next subsection, I discuss the overall radiation mitigation strategy in the experimental hall that effects personnel and equipment.

5.2.3 Other Systems

In this subsection, I discuss the optimization studies for a few other systems and support infrastructure. I helped to perform these studies to ensure the safety of personnel and equipment from damages that can be caused by excessive radiation and heat during MOLLER experimental running.

An example of such a study would be the designing of the chamber for the downstream spectrometer. It should be noted that even in the nominal configuration, there is a stray field at the center of the spectrometer which affects the central beam. This drove the choice of a vacuum chamber over a helium-filled chamber to house the downstream spectrometer [Fair et al., 2020a]. The helium-filled chamber would have been cheaper but required a narrow central Aluminum beam pipe. But the central beam deflected by the stray magnetic field at the center of spectrometer causes excess showering in the pipe. As shown in figure 5.15, this increases the background levels at the main detector assembly reducing our ability to deconvolve the main signal

Figure 5.15: Background levels at the detector plane for helium-filled (left) vs vacuum (right) chamber for downstream spectrometer. An alternate design for the downstream spectrometer chamber was considered to save financial cost where it was filled with helium instead of maintaining a vacuum inside. This would necessitate a narrow central Aluminum beam pipe compared to a wider beam pipe for the vacuum case. However, the stray field at the center of the spectrometer even in a nominal spectrometer configuration deflects the halo of the central beam onto the beam pipe. So, the vacuum chamber was deemed worth the extra cost to avoid systematic issues due to the enhanced background from showering in the pipe.

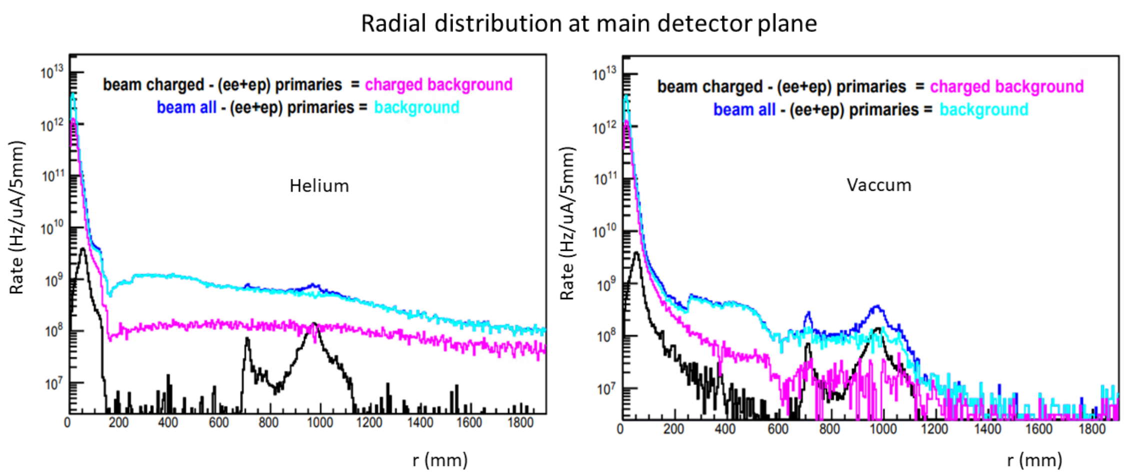

from backgrounds. It also results in enhanced prompt radiation and chronic dose in the experimental hall that can cause problem for sensitive equipment and electronics as well as complicating crew entry into the hall for necessary maintenance over the course of the experiment. So, the extra cost incurred for the vacuum chamber is offset by the physics and radiation safety advantage.

From an instrumental safety point, the PMT region of the main detector assembly, the GEM tracking region, and the electronics bunkers are very important regions. To ensure that they are adequately shielded, I helped to run remoll simulations to

Figure 5.16: Types of radiation damage that could affect MOLLER instruments [Rahman, 2020].

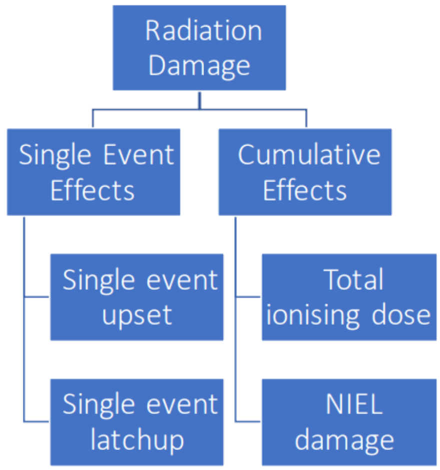

estimate various types of radiation damage that MOLLER instruments in those areas are susceptible to. Figure 5.16 shows the typical classification of radiation damages. For the detector PMTs, cumulative ionizing dose was estimated to be 60 kRad, a factor of 5 below the safety level [Rahman, 2020]. Ionizing radiation is not a big concern for the heavily shielded electronics bunkers. The damage from non-ionizing energy loss (NIEL) was calculated for the detector PMTs, GEM region and bunkers to be $1e12$, $4e12$ and $1e9$ n 1MeV eq respectively [Rahman, 2020]. The NIEL dose safety limit for commercial electronics is $1e13$ n 1MeV eq, an order of magnitude higher than the estimates. So, the instruments should be insensitive to NIEL damage. Finally, the single event effects are estimated to be inconsequential since the simulated flux at different locations are similar to previous experiments [Rahman, 2020].

As shown in figure 5.17, human safety concerns for MOLLER include high energy (> 30 MeV) neutrons traveling through the roof of the experimental hall and showering in the surrounding area. This is called skyshine radiation. The radiation is measured by meters spread around the Jefferson Lab facility. The dose measured by the radiation meters is proportional to the high energy neutron flux reaching the roof. The proportionality constant is known from the PREX data. So, by simulating

Figure 5.17: Visualization of high energy (> 30 MeV) neutron radiation hitting the hall A roof [Rahman, 2020]. The high energy neutrons hitting the roof of the experimental hall showers on the surrounding area and is referred to as skyshine radiation. Radiation meters spread around the Jefferson Lab facility measure the radiation to check if it is in compliance with USDOE/Jefferson Lab limit for human safety of 100/10 mrem/yr. An estimate of 2.4 mrem/yr was obtained for MOLLER skyshine radiation using remoll [Rahman, 2020]. Recent studies with simplified target design found the dose increasing to 4.6 mrem/yr.

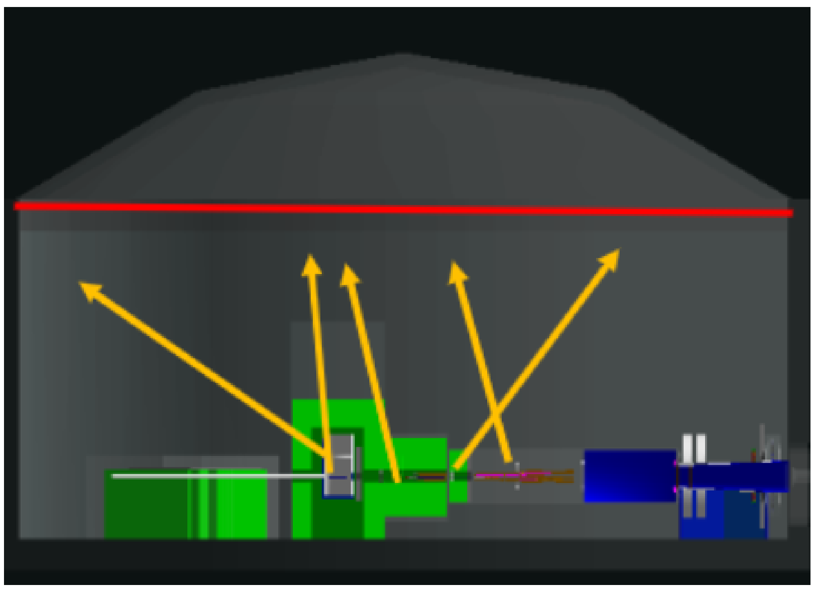

the MOLLER high energy neutron flux at the roof, I helped to estimate a dose of 2.4 mrem/yr for MOLLER skyshine radiation [Rahman, 2020]. Recent modifications to target shielding has increased this dose estimate to 4.6 mrem/yr. However, this is well under the USDOE/Jefferson Lab limit for human safety of 100/10 mrem/yr. Preliminary crosschecks with FLUKA (a Monte Carlo simulation package used for radiation dose and activation studies) by Jefferson Lab Radiation Control group yield similar conclusions.

To make it easier to cool the target and the collimators absorbing radiation from the target, the Møller target design was shortened from an initial 1.5 m to 1.25 m. The

Figure 5.18: Example of Møller figure of merit calculation for ring 5 main detectors [Rahman, 2019]. To calculate the figure of merit for ring 5 main detectors, sector-wise plots of Møller radial distribution weighted by rate$\times$ Asymmetry^2 were made. Then the distribution was integrated over the radial extent of the quartz in ring 5. The inverse of the square root of the integral was used as a figure of merit (FOM). So, to compare a new (n) design with an older (o) one, the FOM ratio $\sqrt{\frac{r_o A_o^2}{r_n A_n^2}}$ is calculated. If the FOM ratio is ≥ 1, that indicates a loss of statistical power [Rahman, 2019].

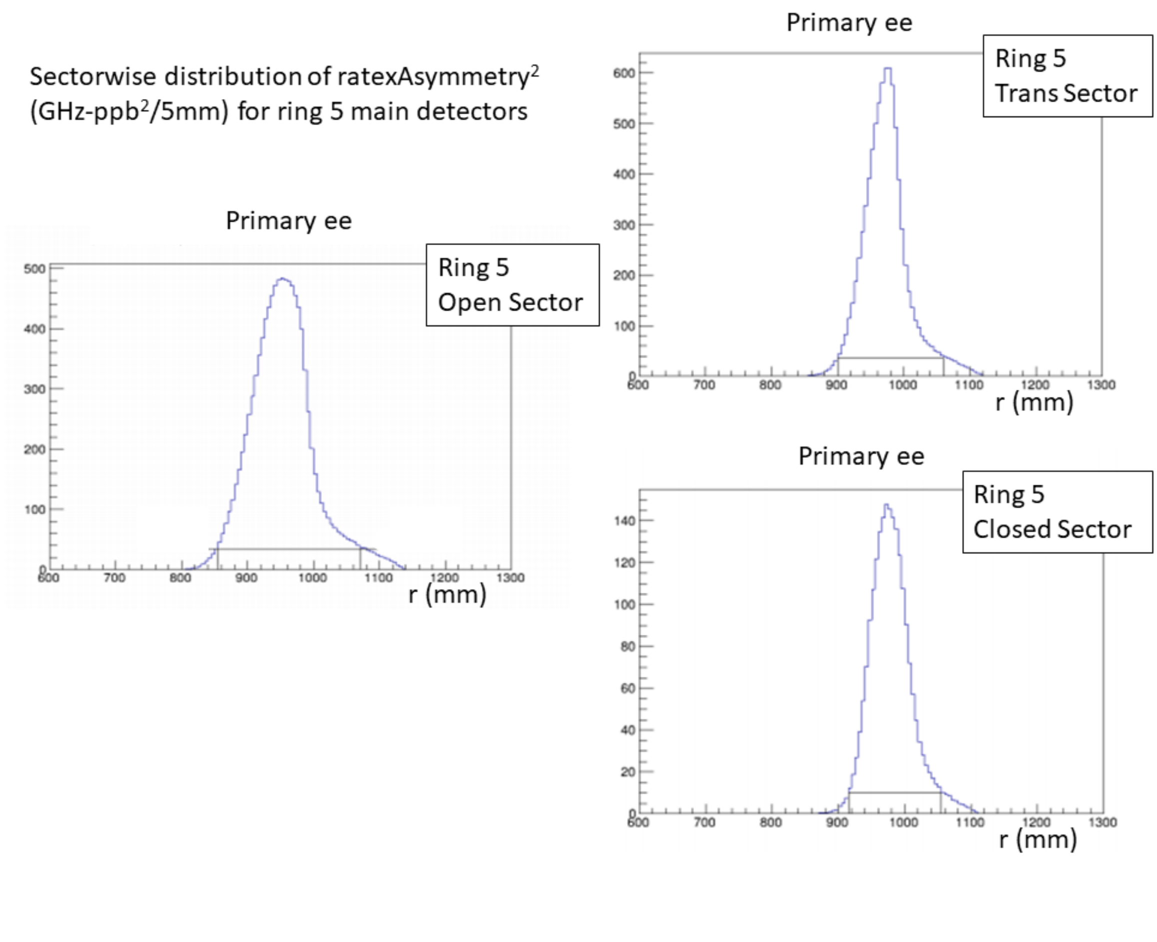

position of the collimators were also adjusted, and the distance between the target and the main detector assembly was reduced to the current length of 26.5 m to meet space constraints and preserve optics [Rahman, 2019]. To compensate for the loss in statistics due to shorter target, I tested the effect of enlarging the acceptance holes of the acceptance defining collimator 2 with a number of design iterations. The figure of merit (FOM) and percentage of background elastic ep rate compared to total rate in ring 5 were calculated in each case. A sample FOM calculation is shown in figure 5.18 and the elastic ep background percentage could be easily calculated from simple radial plots like that shown in 5.6. Initially, the collimator 2 acceptance inner and outer radii were increased from 35.3 mm and 98 mm to 35 mm and 103 mm respectively. However, a more conservative radial range of 35 mm to 101 mm was chosen for the acceptance holes in the end [Rahman, 2019]. Figure of merit analysis showed that there was a net loss of 4% statistical power going from the previous design to the current shortened experiment with new collimator dimensions but that was offset by a reduction of ep background percentage from $\sim 17\%$ to $\sim 11\%$ [Rahman, 2019]. So, the target design could be shortened without losing too much physics advantage.

In conclusion, huge progress has been made in the design of different experimental subsystems of MOLLER. I played a key part in multiple design optimization studies by helping to develop the remoll simulation framework and to analyze simulation outputs. The simulation results have been integral in the progress of MOLLER to CD-1 status as a USDOE project.

Chapter 6

Conclusion

6.1 Summary of Results

The PREX and MOLLER experiments use parity-violating electron scattering to improve our understanding of dense neutron matter and Physics Beyond the Standard Model respectively.

By scattering polarized electrons from unpolarized ^{208} Pb nucleus, the PREX-2 experiment measured the parity violating asymmetry [Paschke et al., 2021]

$$A_{PV}^{meas} = 550 \pm 16 \text{ (statistical)} \pm 8 \text{ (systematic) ppb.}$$

Combining the PREX-2 data with the PREX-1 data, we get robust constraints on the interior baryon density [See figure 6.1] and the neutron skin (0.283 ± 0.071 fm). The interior baryon density is closely connected to the nuclear saturation density, an important quantity for chiral EFT calculations of forces among nucleons [Horowitz et al., 2020]. On the other hand, by using the model correlations between the neutron skin and the density dependence of the symmetry energy (L) we find that [Paschke et al., 2021]

$$L = 106 \pm 37 \text{ MeV},$$

implying that the symmetry energy is quite stiff near the nuclear saturation density.

Figure 6.1: The interior baryon density for ^{208}Pb, extracted from combined PREX-1 and PREX-2 data sets. A 2.5% error band is also shown. Reprinted figure with permission from author [Paschke et al., 2021]. The baryon density is obtained by adding the measured interior weak charge density with the previously known electric charge density [de Vries et al., 1987]. The interior baryon density for the stable and neutron-rich ^{208}Pb is expected to be close to the nuclear saturation density, a benchmark quantity in nuclear structure studies. Precise knowledge of the nuclear saturation density will facilitate chiral EFT calculations of forces among nucleons [Horowitz et al., 2020].

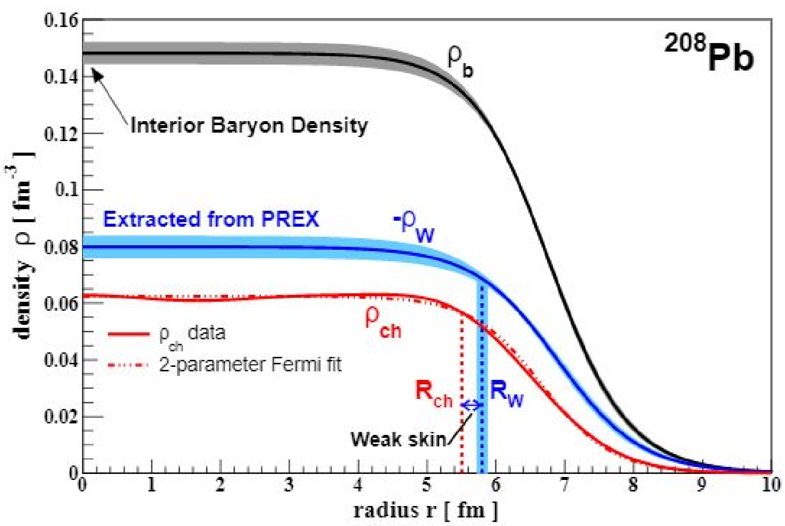

This is in reasonable agreement with constraints on L from diffusion data in heavy ion collision experiments, and finite nuclei ground state properties and giant monopole resonances [Yue et al., 2021]. The PREX result also has implications for neutron star studies. It adds to the understanding of cooling mechanism for neutron stars. In addition, using the model-predicted relationship between tidal deformability of $1.4M_{\odot}$ neutron stars ($\Lambda_*^{1.4}$), the neutron skin of ^{208}Pb ($R_n - R_p$), and the radii of $1.4M_{\odot}$ neutron stars ($R_*^{1.4}$) along with the PREX and the Neutron Star Interior Composition Explorer (NICER) measurements, the following combined set of constraints is obtained [Reed et al., 2021]:

$$0.21 \lesssim R_n - R_p(\text{fm}) \lesssim 0.31,$$

$$13.25 \lesssim R_*^{1.4}(\text{km}) \lesssim 14.26,$$

$$642 \lesssim \Lambda_*^{1.4} \lesssim 955.$$

It should be noted that the above constraint on tidal deformability is in 1-sigma tension with the LIGO GW170817 gravitational wave measurement which predicts [Abbott et al., 2018]

$$\Lambda_*^{1.4} \lesssim 580.$$

The MOLLER experiment will leverage the experience and technical improvements gained during PREX-2 and past parity-violating electron scattering experiments, including but not limited to reduction of systematic errors arising from the polarized electron source, improved monitoring of beam quality, improved understanding of shielding requirements, improved detector capabilities, and improved analysis framework. This is a significant advantage on top of the high quality of research and development done solely for MOLLER, including but not limited to the development of a comprehensive simulation framework to assess various aspects of the experimental design and the advances in hardware technology such as the development of a novel spectrometer with full azimuthal coverage [Kumar et al., 2020]. MOLLER is expected to measure the parity-violating asymmetry in polarized electrons scattering from unpolarized atomic electrons in the liquid hydrogen target to a precision of 0.8 ppb. This will result in a measurement of the weak charge of the electron to a precision of 2.4% at $Q^2 \sim 0.0056$ GeV^2. Since the weak charge of the electron is related to the $\sin^2\theta_W$, direct comparisons can be made to the Standard Model prediction. The test will also be sensitive to new MeV and TeV-scale interactions because the measurement will detect interaction amplitudes as small as $1.5 \times 10^{-3}\ G_F$. MOLLER will complement the high-energy searches for new physics at colliders with a highly precise measurement at low energy.

6.2 Future Work

The results from PREX and MOLLER will be important in the context of other recent and future planned experiments [See figure 6.2]. The significance of the tension between combined PREX+NICER and gravitational wave measurements can only be confirmed by more precise determination of the neutron skin planned at the MESA facility in Mainz along with more precise neutron star radii measurements by NICER and more gravitational wave observations by LIGO-Virgo-KAGRA facilities at higher detector sensitivity. Persistent tensions may indicate exotic phase transitions at the core of neutron stars [Reed et al., 2021].

Additionally, the CREX (Calcium Radius Experiment) experiment completed just after PREX-2 at JLAB falls within the theoretical reach of both ab initio and DFT theories. The precision measurement of ^{48}Ca neutron skin by CREX will be compared against coupled cluster calculations. It will illuminate the role of 3 neutron forces in nuclear structure and also help to anchor density functional theories [Horowitz et al., 2014; Yue et al., 2021]. Thus, predictions can be made with more confidence. Significant disagreement between the CREX result and coupled cluster predictions may indicate limitations of the ab initio theories, such as, ill-convergence of chiral expansions due to large Δ resonance contributions [Horowitz et al., 2014]. The MREX experiment at the MESA facility will improve on the PREX-2 result by measuring the neutron distribution radius in ^{208}Pb up to a fractional accuracy of 0.5%, providing tighter constraints on L [Becker et al., 2018]. Furthermore, the PREX and CREX experiments will also guide the strong probe measurements of the neutron distributions of exotic nuclei at the Facility of Rare Isotope Beam (FRIB) [Piekarewicz and Fattoyev, 2019] and help reduce systematic uncertainties in atomic parity violation experiments [Wieman and Derevianko, 2019]. In terms of Standard Model tests similar to MOLLER, the MESA-P2 and MESA-12C experiments will use parity-violating electron-proton scattering in liquid Hydrogen and Carbon targets respectively to pro-

Figure 6.2: Current and future parity experiments. The PREX-2 and MOLLER experiments push the precision frontier in neutron radius measurement and tests of the SM respectively. Reprinted figure with the kind permission of the European Physical Journal (EPJ) [Becker et al., 2018; Gal, 2020]. The recently concluded CREX experiment along with PREX will provide input to bridge the gap between ab initio and density functional theories of nuclear structure. They will also provide handles to tune the strong probe measurements of neutron distributions and skins at the Facility of Rare Isotope Beam (FRIB) [Piekarewicz and Fattoyev, 2019]. The MREX (Mainz Radius Experiment) experiment at the Mainz Energy-Recovering Superconducting Accelerator (MESA) facility plans to improve on the precision of the PREX-2 neutron skin measurement of ^{208}Pb. Standard Model tests (MESA-P2 and MESA-12C with physics reach of up to 50 and 60 TeV respectively) similar to MOLLER are also being planned to be conducted at MESA [Becker et al., 2018]. SOLID-PVDIS is another experiment planned at Jefferson Lab that will be sensitive to new physics at the $10 - 20$ TeV scale [Gal, 2020].

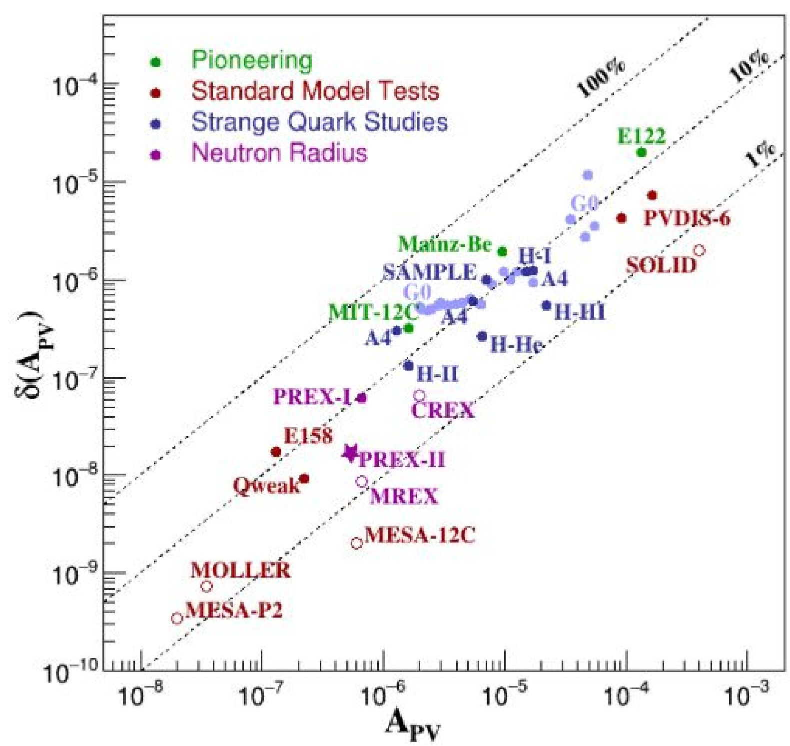

vide high precision measurements of $\sin^2\theta_W$ at low Q^2. MESA-P2 will be sensitive to new physics at the scale of 70 MeV to 50 TeV and MESA-12C can reach mass scales up to 60 TeV [Becker et al., 2018]. The planned SOLID-PVDIS experiment, employing parity-violating electron-deuteron and proton scattering, at JLAB will be sensitive to new physics at the $10-20$ TeV scale [Gal, 2020]. MOLLER will be the first indirect probe near the 10 TeV scale and thus will be a pioneer for these next generation experiments. MOLLER is uniquely positioned in terms of experimental readiness as demonstrated by its current CD-1 project status under the US Department of Energy and completion of significant research and development of key experimental components.

In conclusion, PREX and MOLLER are part of a family of parity-violating electron scattering experiments that will complement developments in a range of other fields including nuclear physics, atomic physics, and nuclear astrophysics. We look forward to new measurements and theoretical developments in this field and the related ones to provide further constraints on important fundamental quantities and discover limitations of existing theories.

Appendix A

Supplementary Information for MOLLER

A.1 Standard Diagnostic Plots

I developed the standard diagnostic plots that were used in the design optimization studies to compare different configurations of the spectrometer[Rahman, 2021]. A short history of the many iterations of the spectrometer is provided in the next section. For each iteration, I adjusted the detector tiling using the methodology described in section 5.2.2. The plots presented in this appendix section correspond to the latest iteration of the spectrometer as of April 26, 2021. The particle hit distributions on the detector plane provide information to optimize tiling (see figure A.1 to A.5). The scattering angle, energy, and Q^2 distributions provide information about the underlying acceptance (see figure A.6 to A.10). The expected asymmetry distributions (figure A.11) in each detector depend on the kinematic acceptance defined by the collimators, focusing properties of the spectrometer magnets, and the geometric acceptance of the specific quartz tile.

Figure A.1: Radial distribution at the main detector plane.

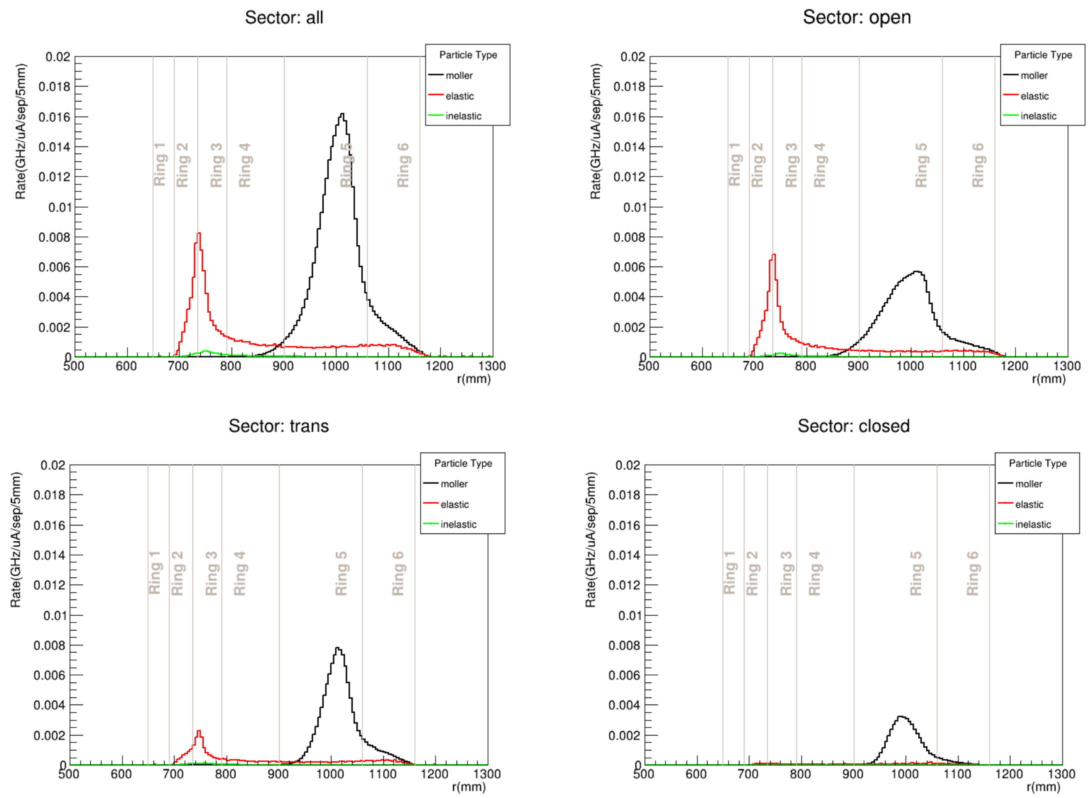

Figure A.2: XY distribution at the main detector plane.

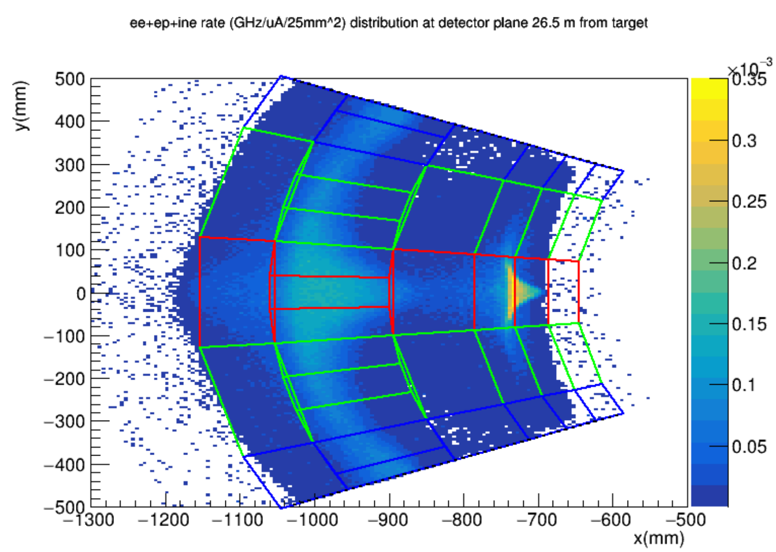

Figure A.3: All particles at the main detector plane.

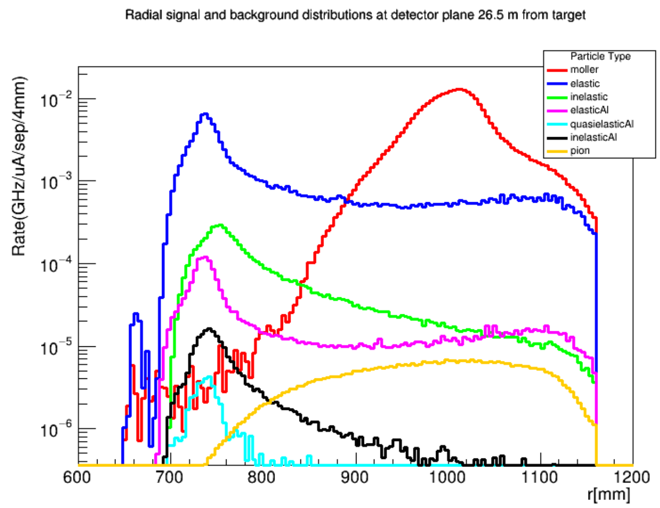

Figure A.4: Dilution weighted asymmetry (f_iA_i) distribution at the main detector plane.

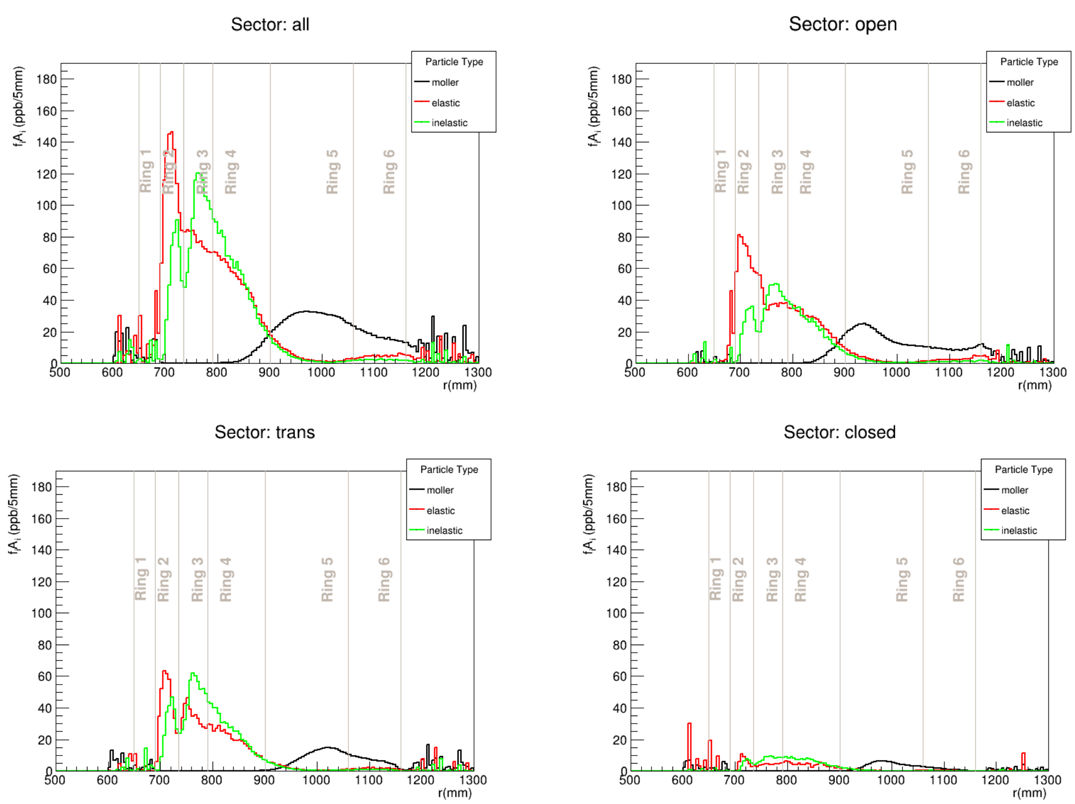

Figure A.5: Azimuthal angle distribution at the main detector plane.

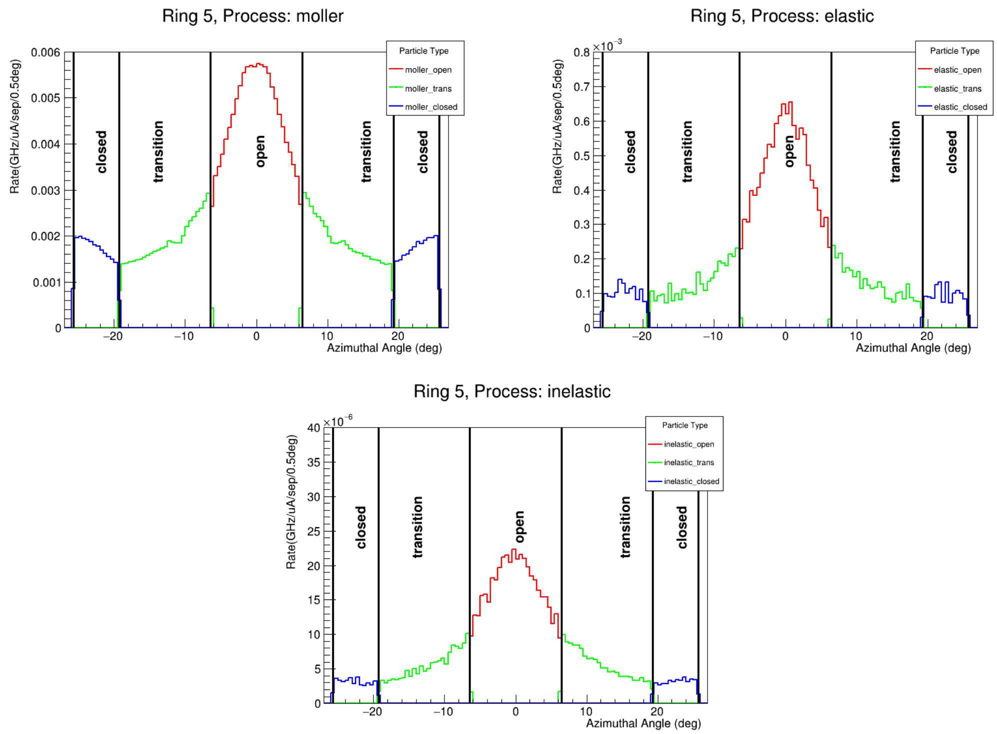

Figure A.6: Center-of-mass scattering angle distribution (θ_{COM}) for hits on the main detector plane.

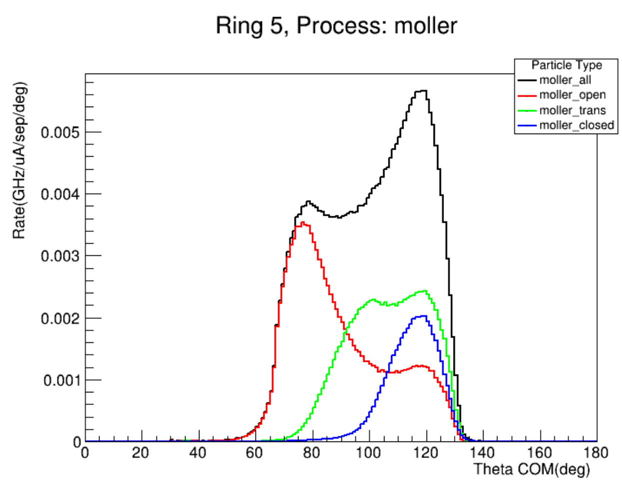

Figure A.7: Lab scattering angle distribution (θ_{lab}) for hits on the main detector plane.

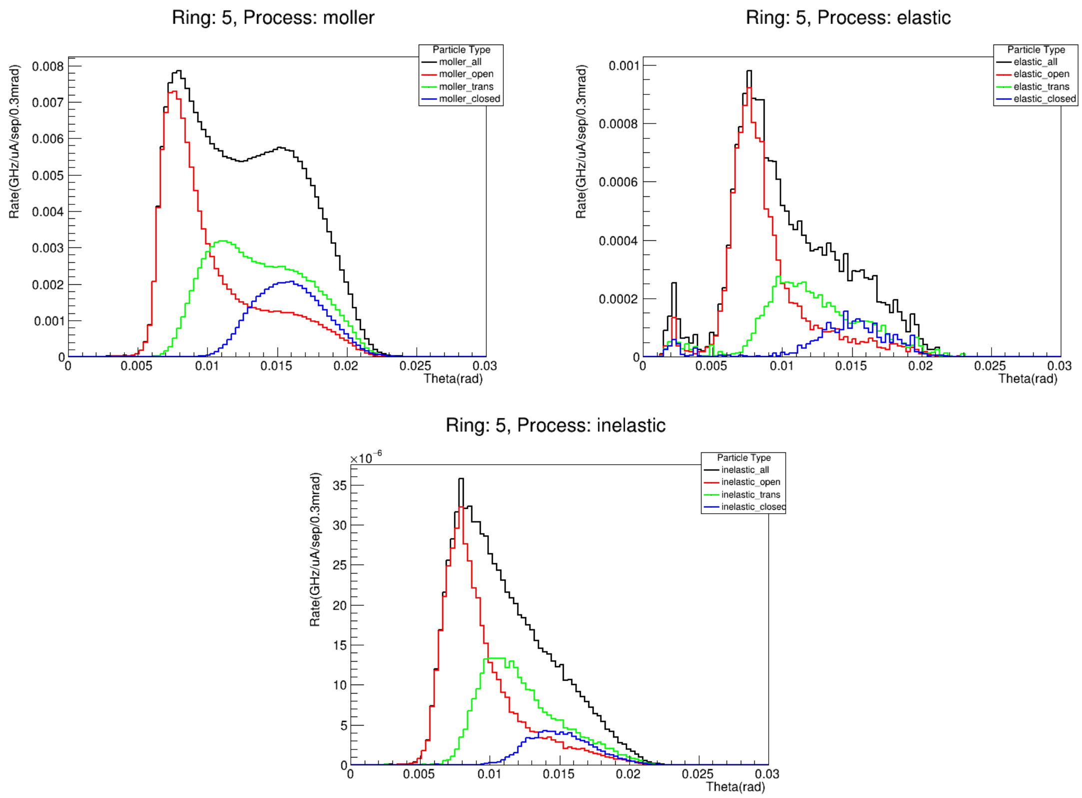

Figure A.8: Rate-weighted distribution of lab scattering angle vs radial position at the main detector plane.

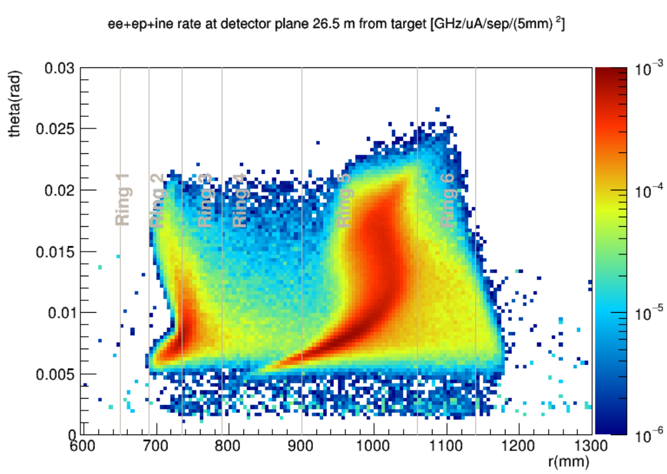

Figure A.9: Incident energy distribution at the main detector plane.

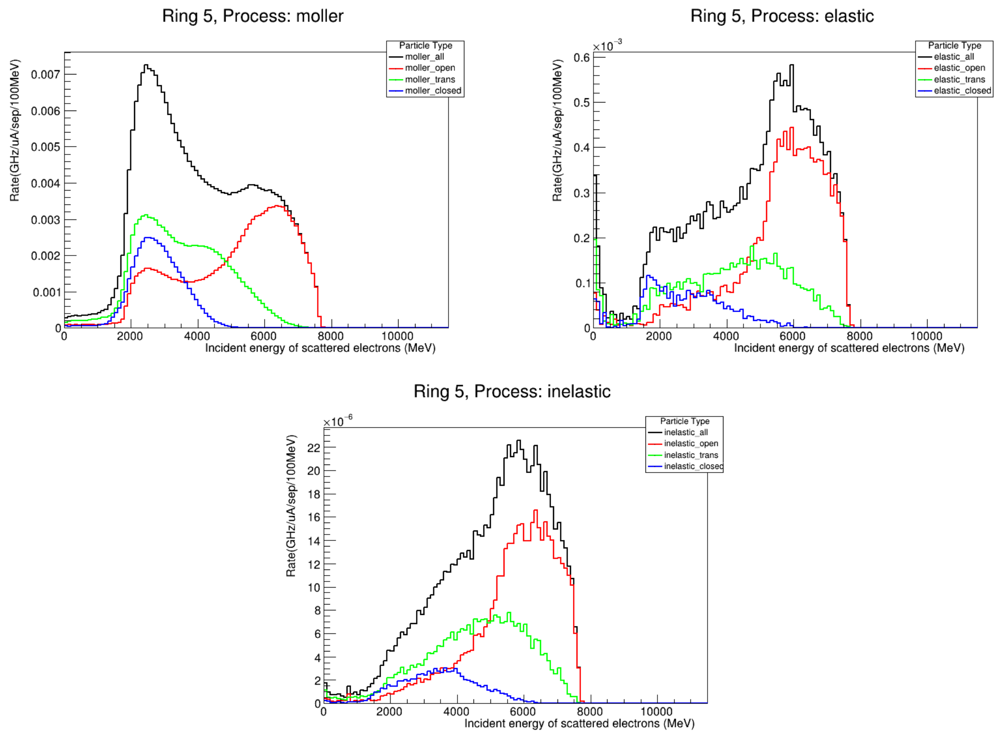

Figure A.10: Q^2 distribution at the main detector plane.

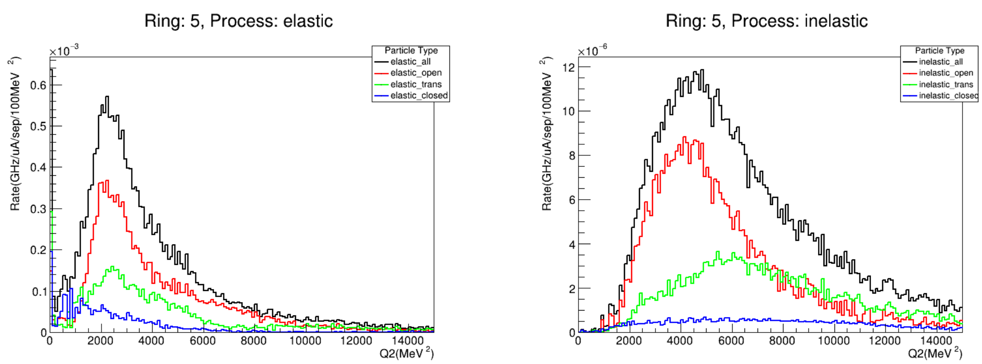

Figure A.11: Asymmetry distribution at the main detector plane.

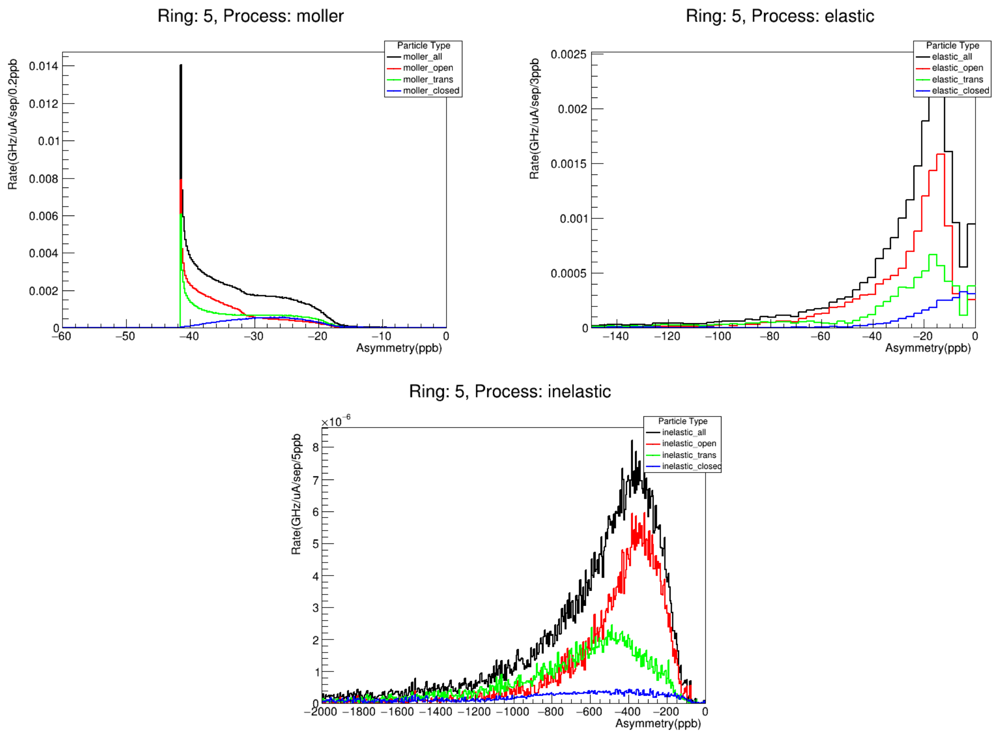

A.2 A brief history of the MOLLER spectrometer system

Initially, the MOLLER spectrometer system was conceived to have an upstream spectrometer and a downstream hybrid spectrometer. Each spectrometer consisted of 7 water-cooled Copper magnet coils spaced equally over the full azimuth as shown in figure A.12. A prototype coil was even developed for the downstream hybrid design as a proof of concept [Mammei, 2018]. Around 2018, I started working with physics collaborators as well as the JLAB engineering group to develop a practical spectrometer design for the experiment taking into account both physics and engineering constraints. The segmented design, where each of the downstream coils were divided into 4 segments, was first tested in simulation as an alternative to the hybrid

Figure A.12: Azimuthal positioning of magnet coils of the spectrometers. The view is from the perspective of the beam moving downstream.

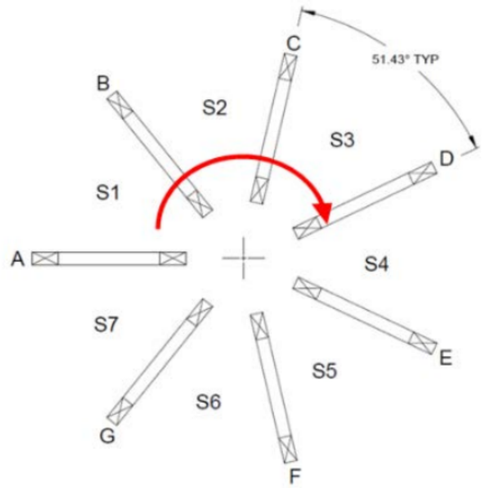

Figure A.13: Hybrid prototype manufactured by Everson-Tesla and delivered to MIT-Bates. Reproduced with permission from author [Mammei, 2018]

design in 2019. Since then, many iterations of the segmented and hybrid design of the downstream coil were tested. The engineering group came up with a comprehensive method to manage risks (ex: electrical shorts, overheating etc.) associated with any design [Ghoshal et al., 2020]. I worked on ensuring that the optics did not change significantly enough across iterations to effect the ability to extract the

Figure A.14: Hybrid and segmented magnet conceptual conductors overlaid (left) and comparison of field profiles as a function of radius at a particular location for the two concepts (right). Reproduced with permission from author [Mammei, 2021].

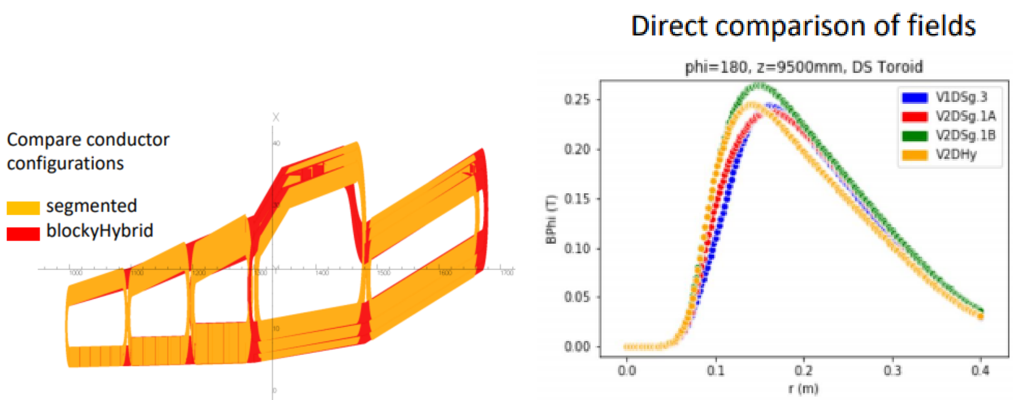

Møller asymmetry via deconvolution. The magnetic field profile generated by the hybrid and segmented iterations were very similar by design. The radial distributions at the detector plane were similar and the uncertainty associated with extracted Møller asymmetry was also very similar. There was no physics reason for choosing one spectrometer concept over the other. The segmented design was selected at the end after a comprehensive Pugh matrix analysis [Fair et al., 2020b]. The finalizing of the downstream segmented single coil design was a significant milestone for the experiment. In terms of the collective configuration, a minor tweak was made since then so that each upstream magnet coil and the first three segments of each downstream magnet coil are placed parallel to the beam axis instead of having a very shallow angle. This had no effect on the optics [Mammei, 2021]. Further details remain to be finalized and understood, such as, the details of the upstream single coil, the optimal shielding, the tolerable vacuum level in spectrometer chambers, and the effects of spectrometer coil offsets and deformation.

A.3 Potential shielding improvement to mitigate known backgrounds and radiation effects

Figure A.15: Dipole field inside downstream spectrometer in symmetric and offset coil case. Reproduced with permission from author [Mammei, 2021].

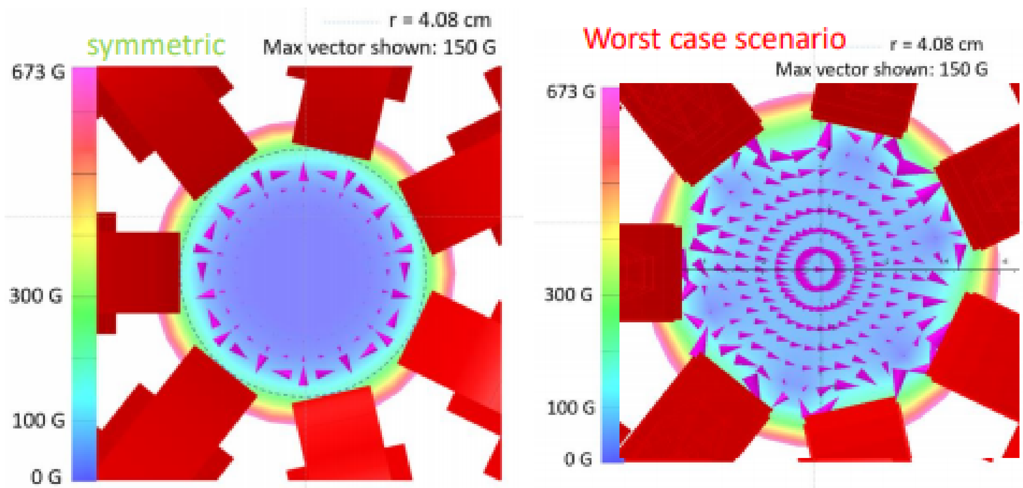

One of the known concerns for the MOLLER experiment is the effect of stray dipole field inside the downstream spectrometer even when the coils are perfectly positioned. This dipole field causes charged particles traveling down the beamline to bend into the coils or bend into the detector contaminating the acceptance. The problem is exacerbated when the detector coils are offset or deformed even within defined optical tolerance. The solution was found to be placing two tungsten tubes to protect the hot zones on the downstream coil to mitigate the radiation dose and a third tungsten tube further downstream to stop particles bending into detector acceptance (see figure 3.10). There is already some noticeable improvement. For example, some of the low radius eps that were making it into the detectors were blocked. Comparing the deconvolution result tables A.1 and 5.2 [case with no W tubes], it can be seen that the ep asymmetry was being pulled down towards 0 in the case with no tungsten tubes. This is what we would observe if unwanted beamline

Table A.1: Extracted asymmetry and uncertainty with the deconvolution technique in ring 5 open sector with downstream tungsten tubes.

Name	Asymmetry [ppb]	Uncertainty [ppb]	Relative Uncertainty [%]
ee	-34.87	0.74	2.13
ep elastic	-28.69	1.78	6.20
ep inelastic $W = 1 - 1.4$ GeV	-613.86	88.44	14.41
ep inelastic $W = 1.4 - 2.5$ GeV	-596.22	51.50	8.64
ep inelastic $W = 2.5 - 6$ GeV	-463.20	112.26	24.24

elastic eps were making it into the detectors. The use of the W tubes helps to improve the fractional uncertainty in extracted asymmetries slightly as well. Similarly, the coil doses for the downstream magnet has been mostly tuned down with the help of the tubes but further improvements may be possible especially at the nose of the coils. Currently, work is being done to optimize these tubes so that they offer the protection to the coils and suppresses the beamline ep backgrounds for both symmetric and offset coil cases.

A.4 List of Collaborators

M. Abdullah Mamun, P. Adderley, E. Becker, J. Benesch, P. Brindza, J. Brock, D. Bullard, J. Butler, R.D. Carlini, J-P. Chen, E. Chudakov, S. Covrig, M.M. Dalton, P. Degtiarenko, A. Deur, A. DiPette, R. Fair, J. Fast, H. Fenker, E. Folts, D. Gaskell, A. Gavalya, P. Ghoshal, J. Grames, J. Gomez, S. Gopinath, O. Hansen, L. Harwood, W. Henry, C. Hernandez-Garcia, D.W. Higinbotham, A. Hofler, C. Hutton, D. Kashy, R. Kazimi, C. Keith, C. Keppel, P. Kessler, K. Krug, S. Malace, D. Meekins, R. Michaels, J. Miller, B. Moffit, D. Moser, M. Poelker, Y. Roblin, J. Segal, C. Soova, M. Stutzman, R. Suleiman, E. Trovatore, Y. Wang, R. Wilson, R. Wines, B. Wojtsekhowski, S. Wood, L. Zana, S. Zhang, C. Zorn

Thomas Jefferson National Accelerator Facility

X. Bai, G. Cates, D. Day, D. Di, K. Gnanvo, N. Liyanage, V. V. Nelyubin, H. Nguyen, C. Palatchi, K. D. Paschke, S. Premathilake, A. Zec

University of Virginia

F. Araiza-Gonzalez, K. Dehmelt, C. Clarke, A. Deshpande, C. Feldman, C. Gal, C. Ghosh, T. K. Hemmick, S. Park, R. Richards, T. Ye, J. Zhang, W. Zhang

Stony Brook University, SUNY

P. Blunden, W. Deconinck, M. T. W. Gericke, J. Mammei, C. Match, H. S. Lee, J. Pan, P. Pandey, S. Rahman, W. T. H. van Oers,

University of Manitoba

V. Bellini, V. Brio, F. Mammoliti, C. Sutera, F. Tortorici

INFN Sezione di Catania and Università di Catania

K. Aulenbacher, D. Becker, S. Baunack, F. Maas, V. Tioukine, M. Wilfert

Johannes Gutenberg Universitaet Mainz

G. De Cataldo, R. De Leo, D. Di Bari, L. Lagamba

INFN, Sezione di Bari and Università di Bari

R. S. Beminiwattha, K. Johnston, N. Simicevic, S. Wells

Louisiana Tech University

D.S. Armstrong, T.D. Averett, V.F. Owen, E.W. Wertz

College of William & Mary

K. S. Kumar [Contact*], R. Miskimen, M. J. Ramsey-Musolf

University of Massachusetts, Amherst

Yu. G. Kolomensky, Y. Mei, E. Sichtermann

Lawrence Berkeley National Laboratory and University of California, Berkeley

D. Adhikari, T. A. Forest, D. McNulty

Idaho State University

J. Bessuille, E. Ihloff, J. Kelsey

Massachusetts Institute of Technology

J. A. Dunne, D. Dutta, L. El Fassi

Mississippi State University

B. Jamieson, R. Mammei, J. W. Martin

University of Winnipeg

D. Jones, J. Napolitano, D. Nikolaev

Temple University

E. King, P. Souder

Syracuse University

A. Lee, M. L. Pitt

Virginia Polytechnic Institute and State University

P. M. King, J. Roch *Ohio University*

F. Meddi, G. M. Urciuoli

Dipartimento di Fisica dell´Università la Sapienza and INFN Sezione di Roma

E. Cisbani, F. Garibaldi

INFN Gruppo Collegato Sanità and Istituto Superiore di Sanità

J. C. Cornejo, B. Quinn

Carnegie Mellon University

A. Ahmidouch, S. Danagoulian

North Carolina A&T State University

O. Glamazdin, R. Pomatsalyuk

NSC Kharkov Institute of Physics and Technology

A. Aleksejevs, S. Barkanova

Memorial University, Grenfell

R. Gilman, R. Ransome

Rutgers University

T. Holmstrom

Longwood University

J. Erler

Universidad Nacional Autónoma de México

K. A. Aniol

California State U.(Los Angeles)

W. D. Ramsay

TRIUMF

E. Korkmaz

University of Northern British Columbia

D. T. Spayde

Hendrix College

F. Benmokhtar

Duquesne University

A. Del Dotto

INFN, Laboratori Nazionali di Frascati

R. Perrino

INFN Sezione di Lecce

J. Singh

NSCL and Michigan State University

C. Annasiwatta

Muskingum University

*kkumar@physics.umass.edu

Appendix B

Supplementary Information for PREX-2

B.1 List of Collaborators

S. Barcus, J. F. Benesch, A. Camsonne, S. Covrig Dusa, D. Gaskell, J.-O. Hansen, C. Keppel, S. Malace, M. McCaughan, D. Meekins, R. Michaels, Y. Roblin, L. Tang, B. Wojtsekhowski

Thomas Jefferson National Accelerator Facility

D. Adhikari, D. McNulty

Idaho State University

H. Albataineh

Texas A & M University

D. Androic

University of Zagreb

K. Aniol

California State University

D. S. Armstrong, T. Averett, C. Ayerbe Gayoso, Q. Campagna, C. Metts, V. Owen,

E. W. Wertz, B. Yale

College of William & Mary

V. Bellini

Istituto Nazionale di Fisica Nucleare

R. S. Beminiwattha, D. Bhatta Pathak, Y. Chen

Louisiana Tech University

H. Bhatt, D. Bhetuwal, D. Dutta

Mississippi State University

S. Rahman, B. Blaikie, M. Gericke, I. Halilovic, G. Leverick, J. Mammei, J. Pan

University of Manitoba

C. Clarke, A. Deshpande, C. Feldman, C. Gal, C. Ghosh, T. Kutz, M. M. Mondal, S. Park, M. Petrusky, T. Ye, R. Richards, W. Zhang, J. Zhang

Stony Brook University

J.C. Cornejo, B. Quinn

Carnegie Mellon University

P. Datta, E. Fuchey, A. J. R. Puckett, S. Seeds

University of Connecticut

T. Gautam, N. Lashley-Colthirst, B. Pandey

Hampton University

C. Ghosh, S. Johnston, K.S. Kumar, H. Liu

University of Massachusetts Amherst

F. Hauenstein, M. N. H. Rashad

Old Dominion University

W. Henry, D. C. Jones, J. Napolitano, D. Nikolaev

Temple University

C. J. Horowitz, B. T. Reed

Indiana University

K. D. Paschke [Contact*], C. Jantzi, S. Jian, S. Katugampola, N. Liyange,

C. Palatchi, S. Premathilake, A. Rathnayake, A. Zec, X. Zheng

University of Virginia

B. Karki, P. M. King, R. Radloff

Ohio University

D. E. King, P. Souder, Y. Tian

Syracuse University

M. Knauss

Duquesne University

R. Mammei

University of Winnipeg

A. Narayan

Veer Kunwar Singh University

M. L. Pitt

Virginia Tech

P. E. Reimer, S. Riordan

Argonne National Laboratory

A. Shahinyan

A. I. Alikhanyan National Science Laboratory (Yerevan Physics Institute)

M. Thiel

Institut für Kernphysik, Johannes Gutenberg-Universität

G. M. Urciuoli

INFN - Sezione di Roma

A. Yoon

Christopher Newport University

*paschke@virginia.edu

Appendix C

List of Terms and Abbreviations

A list of commonly used terms and abbreviations used in this document is provided below:

- **MOLLER**: Measurement of a Lepton-Lepton Electroweak Reaction
- **PREX**: Lead (^{208}Pb) Radius Experiment
- $\mathbf{A_{PV}}$: Parity-Violating Asymmetry
- $\mathbf{A_{PV}^{meas}}$: Measured Parity-Violating Asymmetry
- $\mathbf{Q^2}$: Four-Momentum Transfer Squared
- **MeV, GeV, TeV**: Mega (1 million) Electron Volt, Giga (1 billion) Electron Volt, Tera (1 trillion) Electron Volt
- **JLab**: Jefferson Lab or Thomas Jefferson National Accelerator Facility
- **CEBAF**: Continuous Electron Beam Accelerator Facility
- $\mathbf{G_F}$: Fermi Constant
- α: Fine Structure Constant

- $\mathbf{Q_W}$: Weak Charge
- $\rho_{\mathbf{W}}$: Weak Charge Density
- $\rho_{\mathbf{b}}$: Baryon Density
- $\mathbf{F_W}$: Weak Form Factor
- $\mathbf{F_{ch}}$: Electromagnetic Form Factor
- $\mathbf{R_{ch}}$: Electric Charge Radius
- $\mathbf{R_n}$: Radius of Neutron Distribution
- $\mathbf{R_p}$: Radius of Proton Distribution
- $\mathbf{R_n - R_p}$: Neutron Skin
- **nDFT**: Nuclear Density Functional Theory
- **NN Potential, NNN Potential**: Two/Three Nucleon Interaction Potential
- **QMC**: Quantum Monte Carlo
- **EOS**: Equation of State
- $\mathbf{E_{sym}}$: Nuclear Symmetry Energy
- **L**: Nuclear Symmetry Pressure
- $\theta_{\mathbf{W}}$: Electroweak Mixing Angle or Weinberg Angle
- **stat.**: Statistical Uncertainty
- **sys.**: Systematic Uncertainty
- **exp.**: Experimental Uncertainty
- **theo.**: Theoretical Uncertainty

- **CM**: Cryomodule
- **RF**: Radiofrequency
- **RTP**: Rubidium Titanyl Phosphate
- **PPLN**: Periodically Poled Lithium Niobate
- **GSO**: Gadolinium Orthosilicate
- **HRS**: High Resolution Spectrometer
- **LHRS**: Left-sided High Resolution Spectrometer
- **RHRS**: Right-sided High Resolution Spectrometer
- **VDC**: Vertical Drift Chamber
- **GEM**: Gas Electron Multiplier
- **BPM**: Beam Position Monitor
- **diff_bpm**: BPM Double Difference
- **BCM**: Beam Current Monitor
- **HWP**: Half Wave Plate
- **RHWP**: Rotating Half Wave Plate
- **IHWP**: Insertable Half Wave Plate
- **SAM**: Small Angle Monitor
- **DAQ**: Data Acquisition System
- **CODA**: CEBAF On-line Data Acquisition System
- **JAPAN**: Just Another Parity Analyzer

- **ROC**: Read Out Controller
- **HDPE**: High-Density Polyethylene
- **EPICS**: Experimental Physics and Industrial Control System
- $\mathbf{\frac{dP}{P}}$: Fractional change with respect to central momentum of spectrometer
- **HCBA**: Helicity Correlated Beam Asymmetry
- **LED**: Light-emitting Diode
- **ADC**: Analog-to-Digital Converter
- **SM**: Standard Model
- **GUT**: Grand Unification Theory
- **LHC**: Large Hadron Collider
- **SLAC E**158: First experiment measuring the weak charge of the electron
- **CL**: Confidence Level
- **LH2**: Liquid Hydrogen
- **PMT**: Photomultiplier Tube
- **AT Detector**: Auxiliary Transverse Detector
- **MD**: Main Detector
- **NIEL**: Non-Ionizing Energy Loss
- **CW95**: Alloy of 95% Copper and 5% Tungsten
- **GDML**: Geometry Description Markup Language
- **GEANT**: Geometry and Tracking toolkit

- **CAD**: Computer Aided Design
- **HPC**: High Performance Computing
- **SLAC**: Stanford Linear Accelerator
- $\theta_{\mathbf{COM}}$: Center-of-Mass Scattering Angle
- $\theta_{\mathbf{lab}}$: Laboratory Scattering Angle
- $\mathbf{f_i}$: Dilution or fractional rate of process i with respect to total rate
- **MGy**: Mega (1 million) Gray [A unit of absorbed radiation dose]
- **FOM**: Figure of Merit
- **EFT**: Effective Field Theory
- $\mathbf{M}_{\odot}$: Solar Mass
- **NICER**: Neutron Star Interior Composition Explorer
- **LIGO**: Laser Interferometer Gravitational-Wave Observatory
- **MESA**: Mainz Energy-Recovering Superconducting Accelerator
- **KAGRA**: Kamioka Gravitational Wave Detector
- **CREX**: Calcium (^{48}Ca) Radius Experiment
- **MREX**: Mainz Radius Experiment
- **FRIB**: Facility of Rare Isotope Beam
- **SOLID-PVDIS**: Solenoidal Large Intensity Device- Parity Violation in Deep Inelastic Scattering

Bibliography

B. P. Abbott, ⋯, and LIGO Scientific Collaboration and Virgo Collaboration. GW170817: Measurements of neutron star radii and equation of state. *Phys. Rev. Lett.*, 121(16):161101, Oct. 2018. URL `https://journals.aps.org/prl/abstract/10.1103/PhysRevLett.121.161101`.

B. Abi, C. Yoshikawa, ⋯, and Muon $g-2$ Collaboration. Measurement of the positive muon anomalous magnetic moment to 0.46 ppm. *Phys. Rev. Lett.*, 126(14):141801, Apr. 2021. doi: 10.1103/PhysRevLett.126.141801. URL `https://link.aps.org/doi/10.1103/PhysRevLett.126.141801`.

D. Adhikari. Integrating quartz Cherenkov detectors for PREX-2/CREX. In *2020 Fall Meeting of the APS Division of Nuclear Physics*. American Physical Society, Oct. 2020a. URL `https://drive.google.com/file/d/1sKF5RBSaF226C-Q1OvGiBHhFivw_czl5/view?usp=sharing`.

D. Adhikari. Rescattering and inelastic backgrounds. `https://prex.jlab.org/cgi-bin/DocDB/private/ShowDocument?docid=461`, 2020b.

K. A. Aniol, C. Zhang, ⋯, and HAPPEX Collaboration. Parity-violating electroweak asymmetry in $\vec{e}p$ scattering. *Phys. Rev. C Nucl. Phys.*, 69(6):065501, June 2004. doi: 10.1103/PhysRevC.69.065501. URL `https://link.aps.org/doi/10.1103/PhysRevC.69.065501`.

J. Apostolakis and D. H. Wright. An overview of the Geant4 toolkit. *AIP Conf.*

Proc., 896(1):1–10, Mar. 2007. URL https://aip.scitation.org/doi/abs/10.1063/1.2720452?journalCode=apc.

D. S. Armstrong, V. Zeps, ⋯, and G0 Collaboration. Transverse beam spin asymmetries in forward-angle elastic electron-proton scattering. *Phys. Rev. Lett.*, 99(9):092301, Aug. 2007. doi: 10.1103/PhysRevLett.99.092301. URL https://link.aps.org/doi/10.1103/PhysRevLett.99.092301.

D. Becker, S. Rahman, ⋯, and P2 collaboration. The P2 experiment: A future high-precision measurement of the weak mixing angle at low momentum transfer. *Eur. Phys. J. A*, 54(11), Nov. 2018. URL https://link.springer.com/article/10.1140/epja/i2018-12611-6.

J. A. Behr and G. Gwinner. Standard model tests with trapped radioactive atoms. Mar 2009. URL http://www2.physics.umanitoba.ca/u/gwinner/wikis/pmwiki/pmwiki.php?n=Main.Francium?action=download&upname=behr-jpg-2009.pdf.

R. Brun and F. Rademakers. ROOT: An object oriented data analysis framework. *Nucl. Instrum. Meth. A*, 389:81–86, 1997. doi: 10.1016/S0168-9002(97)00048-X. URL https://doi.org/10.1016/S0168-9002(97)00048-X.

M. Cadeddu, N. Cargioli, F. Dordei, C. Giunti, and E. Picciau. Muon and electron $g-2$, proton and cesium weak charges implications on dark Z_d models. Apr. 2021. URL https://arxiv.org/abs/2104.03280v1.

C. Clarke. Benchmarking air light-guide Cherenkov detectors at SLAC ESTB. In *APS April Meeting 2019*. American Physical Society, Apr. 2019. URL https://indico.jlab.org/event/282/contributions/4136/attachments/3284/4016/Benchmarking_SLAC_GHP_short.pdf.

C. Clarke. MOLLER air-lightguides' backgrounds simulation with benchmarked G4 optical physics: Progress update. https://moller.jlab.org/cgi-bin/DocDB/public/ShowDocument?docid=623, July 2020a.

C. Clarke. High luminosity ^{208}Pb targets for the PREX-2 experiment. In *2020 Fall Meeting of the APS Division of Nuclear Physics*. American Physical Society, Nov. 2020b. URL https://drive.google.com/file/d/1iisTtqbDfF4HFbCfXiwGt7PC2_u9YwXU/view?usp=sharing.

C. Clarke, S. Rahman, $\cdots$, and MOLLER Simulation Group. Generator of GDML detector description of the main detector array in the Jefferson Lab 12 GeV MOLLER experiment. https://github.com/JeffersonLab/remoll-detector-generator, 2017.

Controls Software Group. EPICS control system. https://www.jlab.org/accelerator/controls, 2017. Accessed: 2021-1-29.

A. N. Courtemanche. *Electron scattering from the lead nuclei*. PhD thesis, University of Virginia, 1978. URL http://inis.iaea.org/search/search.aspx?orig_q=RN:12590743.

H. Davoudiasl, H.-S. Lee, and W. J. Marciano. Muon anomaly and dark parity violation. *Phys. Rev. Lett.*, 109(3):031802, July 2012. doi: 10.1103/PhysRevLett.109.031802. URL https://link.aps.org/doi/10.1103/PhysRevLett.109.031802.

H. de Vries, C. W. de Jager, and C. de Vries. Nuclear charge-density-distribution parameters from electron scattering. *At. Data Nucl. Data Tables*, 36:495, Jan. 1987. URL https://doi.org/10.1016/0092-640X(87)90013-1.

D. Dominguez. The Standard Model. https://home.cern/science/physics/standard-model, 2020. Accessed: 2020-12-28.

S. C. Dusa. PREX2-CREX target design update. `https://prex.jlab.org/cgi-bin/DocDB/private/ShowDocument?docid=55`, 2018.

J. Erler, P. Langacker, S. Munir, and E. Rojas. Z´ bosons from E(6): Collider and electroweak constraints. Aug. 2011. URL `https://arxiv.org/abs/1108.0685v1`.

R. Fair, J. Mammei, and K. Kumar. MOLLER experiment scattering medium considerations. `https://moller.jlab.org/cgi-bin/DocDB/public/ShowDocument?docid=585`, 2020a.

R. Fair, S. Rahman, J. Mammei, and C. Gal. Hybrid vs. segmented downselect. `https://moller.jlab.org/cgi-bin/DocDB/public/ShowDocument?docid=660`, 2020b.

K. G. Fissum, W. Bertozzi, · · · , and J. Zhao. Vertical drift chambers for the Hall A high-resolution spectrometers at Jefferson Lab. *Nucl. Instrum. Methods Phys. Res. A*, 474(2):108–131, Dec. 2001. URL `https://hallaweb.jlab.org/publications/Talks/2001/Publications/vcd-fissum-01.pdf`.

C. Gal. New precision measurements of the neutral weak form factor of ^{208}Pb. In *2020 Fall Meeting of the APS Division of Nuclear Physics*. American Physical Society, Oct. 2020. URL `https://prex.jlab.org/cgi-bin/DocDB/private/ShowDocument?docid=473`.

S. Gandolfi and A. W. Steiner. Neutron matter, symmetry energy and neutron stars. *Journal of Physics: Conference Series*, 665:012063, Jan 2016. doi: 10.1088/1742-6596/665/1/012063. URL `https://doi.org/10.1088/1742-6596/665/1/012063`.

C. Ghosh. Experience with GEM detectors during the PREX-II physics run. In *2020 Fall Meeting of the APS Division of Nuclear Physics*. American Physical Society, Nov. 2020. URL `https://drive.google.com/file/d/1h362gWw6DJoM8m-1tthGmZ7Lp7OXzojN/view?usp=sharing`.

P. K. Ghoshal, R. J. Fair, $\cdots$, and S. Rahman. General failure modes and effects analysis for accelerator and detector magnet design at jlab. *IEEE Transactions on Applied Superconductivity*, 30(8):1–11, 2020. doi: 10.1109/TASC.2020.3022993.

D. J. Griffiths. *Introduction to elementary particles.* Wiley, New York, 1987.

D. J. Gross. The role of symmetry in fundamental physics. *Proc. Natl. Acad. Sci. U. S. A.*, 93(25):14256–14259, Dec. 1996. URL `https://doi.org/10.1073/pnas.93.25.14256`.

D. W. Higinbotham, T. Keppel, and Hall A Collaboration. Jefferson Lab Hall A standard equipment manual. `https://hallaweb.jlab.org/github/halla-osp/version/Standard-Equipment-Manual.pdf`, 2017. Accessed: 2021-1-17.

C. J. Horowitz, S. J. Pollock, P. A. Souder, and R. Michaels. Parity violating measurements of neutron densities. *Phys. Rev. C Nucl. Phys.*, 63(2):025501, Jan. 2001. URL `https://doi.org/10.1103/PhysRevC.63.025501`.

C. J. Horowitz, K. S. Kumar, and R. Michaels. Electroweak measurements of neutron densities in CREX and PREX at JLab, USA. *The European Physical Journal A*, 50(2):48, Feb. 2014. URL `https://doi.org/10.1140/epja/i2014-14048-3`.

C. J. Horowitz, J. Piekarewicz, and B. Reed. Insights into nuclear saturation density from parity-violating electron scattering. *Phys. Rev. C*, 102(4):044321, Oct 2020. doi: 10.1103/PhysRevC.102.044321. URL `https://link.aps.org/doi/10.1103/PhysRevC.102.044321`.

J. Alcorn et al. Basic instrumentation for Hall A at Jefferson Lab. *Nucl. Instrum. Methods Phys. Res. A*, 522(3):294–346, Apr. 2004. URL `https://doi.org/10.1016/j.nima.2003.11.415`.

Jefferson Lab Communications Office. Jefferson Lab completes 12 GeV upgrade. https://www.jlab.org/news/releases/jefferson-lab-completes-12-gev-upgrade, Oct. 2017. Accessed: 2021-3-22.

S. Jian and N. Liyanage. Jefferson Lab HRS optimization measurement for the PREX-II experiment. In *2020 Fall Meeting of the APS Division of Nuclear Physics*. American Physical Society, Oct. 2020. URL https://drive.google.com/file/d/1PI34kQ25yHBk4DCEIGmYvAKbgBwOdtz5/view?usp=sharing.

JLAB Data Acquisition Group. Run control. https://coda.jlab.org/drupal/content/introduction-1, 2017. Accessed: 2021-2-9.

JLAB Hall A Møller Polarimeter Group. Hall A Møller Polarimeter. https://hallaweb.jlab.org/equipment/moller/OSP/20190219_moller_manual.pdf, 2019.

D. Jones. Møller polarimetry for the neutron skin experiments at Jefferson Lab. In *2020 Fall Meeting of the APS Division of Nuclear Physics*. American Physical Society, Oct. 2020. URL https://drive.google.com/file/d/1W_xXSbibWOBEi-6HAxzA6ZKeXNKPHhPl/view?usp=sharing.

S. Kiadtisak. *Measurement of the Neutron Radius of ^{208}Pb Through Parity Violation In Electron Scattering*. PhD thesis, University of Virginia, 2013. URL https://www.osti.gov/biblio/1079207.

E. King. Key Møller polarimetry systematics for the PREX-2/CREX experiments. In *2020 Fall Meeting of the APS Division of Nuclear Physics*. American Physical Society, Oct. 2020. URL https://drive.google.com/file/d/1RPJ4FeIz7XKjKyKNhLQH8KNjha1UWOXV/view?usp=sharing.

K. S. Kumar, J. Erler, $\cdots$, and MOLLER Collaboration. The MOLLER experiment: An ultra-precise measurement of the weak mixing angle using Møller scattering, 2011. URL https://hallaweb.jlab.org/12GeV/Moller/downloads/DOE_Proposal/DOE_Moller.pdf. Accessed: 2021-2-10.

K. S. Kumar, J. Singh, $\cdots$, and MOLLER Collaboration. The MOLLER experiment: An ultra-precise measurement of the weak mixing angle using møller scattering. Nov. 2014. URL https://arxiv.org/abs/1411.4088v2.

K. S. Kumar, S. Rahman, $\cdots$, and MOLLER Collaboration. The MOLLER project conceptual design report, 2020. URL https://moller.jlab.org/cgi-bin/DocDB/public/ShowDocument?docid=630. Accessed: 2021-2-10.

H. S. Lee. *Fused silica Cherenkov detector response to MeV photons*. PhD thesis, University of Manitoba, 2021. URL https://mspace.lib.umanitoba.ca/xmlui/handle/1993/35272.

H. Liu. *Measurement of the Ratio of the Neutron to Proton Structure Functions, and the Three-Nucleon EMC Effect in Deep Inelastic Electron Scattering Off Tritium and Helium-3 Mirror Nuclei*. PhD thesis, Columbia University, 2020. URL https://www.osti.gov/biblio/1673608.

N. K. Liyanage, R. Michaels, and K. Saenboonruang. Q^2 measurement for PREX. https://hallaweb.jlab.org/parity/prex/qsq/Q2_PREX.pdf, 2011.

J. Mammei. Spectrometer overview. https://moller.jlab.org/cgi-bin/DocDB/public/ShowDocument?docid=446, 2019.

J. Mammei. MOLLER spectrometer update. https://moller.jlab.org/cgi-bin/DocDB/public/ShowDocument?docid=368, 2018.

J. Mammei. April 2021 MOLLER forum spectrometer update. https://moller.jlab.org/cgi-bin/DocDB/public/ShowDocument?docid=719, 2021.

R. Michaels. Data acquisition status. https://prex.jlab.org/cgi-bin/DocDB/private/ShowDocument?docid=252, 2018.

V. Owen. Correcting for helicity correlated beam parameters in the parity-violating electron scattering experiment of PREX-2 at Jefferson Lab. In *2020 Fall Meeting of the APS Division of Nuclear Physics*. American Physical Society, Nov. 2020. URL https://drive.google.com/file/d/1KD79GOBlvQgsmLTb-i9vdHFqgLWwFyDv/view?usp=sharing.

C. Palatchi. *Laser and Electron Beam Technology for Parity Violating Electron Scattering Measurements*. PhD thesis, University of Virginia, May 2019. URL https://www.osti.gov/biblio/1574125.

K. Paschke, P. Rossi, $\cdots$, and PREX Collaboration. PREX-II: Precision parity-violating measurement of the neutron skin of lead, 2011. URL https://hallaweb.jlab.org/parity/prex/prexII.pdf.

K. D. Paschke, K. Kumar, and C. Gal. Dipole poletip scattering estimation. https://prex.jlab.org/cgi-bin/DocDB/private/ShowDocument?docid=457, 2020.

K. D. Paschke, S. Rahman, $\cdots$, and PREX Collaboration. An accurate determination of the neutron skin thickness of ^{208}Pb through parity-violation in electron scattering. *Phys. Rev. Lett.*, 126:172502, Apr. 2021. doi: 10.1103/PhysRevLett.126.172502. URL https://link.aps.org/doi/10.1103/PhysRevLett.126.172502.

J. Piekarewicz and F. J. Fattoyev. Neutron-rich matter in heaven and on earth. *Phys. Today*, 72(7):30–37, July 2019. URL https://doi.org/10.1063/PT.3.4247.

B. Povh, K. Rith, C. Scholz, F. Zetsche, and W. Rodejohann. *Particles and Nuclei: An Introduction to the Physical Concepts*. Springer, June 2015.

S. Premathilake. Polarized source setup and helicity correlated beam asymmetry results for PREX-2. In *2020 Fall Meeting of the APS Division of Nuclear Physics*.

American Physical Society, Oct. 2020. URL https://drive.google.com/file/d/1XD3lch7OKIw2F5lndttUDm6m6Y5LO3BI/view?usp=sharing.

PREX Collaboration. Supplementary material on model uncertainty in R_W and acceptance function. https://drive.google.com/file/d/1Si1OMlOCYce8WzzAf-FSK16U6efZdNbn/view, 2021.

PREX Collaboration. PREX/CREX design document version 3.0. https://prex.jlab.org/cgi-bin/DocDB/private/ShowDocument?docid=2, 2017.

PREX Collaboration. PREX/CREX/HRS simulation with ray tracking optics. https://github.com/sbujlab/g4hrs, 2013.

PREX Collaboration. Just another parity analyzer. https://github.com/JeffersonLab/japan, 2018.

S. Rahman. Simulation and performance of radiation shielding for recent and future parity-violating electron scattering experiments at Jefferson Lab. In *2020 Fall Meeting of the APS Division of Nuclear Physics*. American Physical Society, Nov. 2020. URL https://moller.jlab.org/cgi-bin/DocDB/public/ShowDocument?docid=646.

S. Rahman. FOM analysis for shortening the target. https://moller.jlab.org/cgi-bin/DocDB/public/ShowDocument?docid=584, 2019.

S. Rahman. Scripts for submitting slurm array jobs for remoll simulation and analysis. https://github.com/JeffersonLab/remoll-job-submission, 2021.

S. Rahman, W. Deconinck, $\cdots$, and MOLLER Simulation Group. Generator for producing GDML file for remoll showermax detectors. https://github.com/JeffersonLab/remoll-showermax-generator, 2021a.

S. Rahman, W. Deconinck, ···, and MOLLER Simulation Group. Code for generating GDML file of spectrometer magnets in remoll. `https://github.com/JeffersonLab/remoll-coil-generator`, 2021b.

S. Rahman, J. Mammei, ···, and MOLLER Simulation Group. Code to post-process field map files for remoll. `https://github.com/JeffersonLab/remoll-fieldmap-processor`, 2021c.

B. T. Reed, F. J. Fattoyev, C. J. Horowitz, and J. Piekarewicz. Implications of PREX-2 on the equation of state of neutron-rich matter. *Phys. Rev. Lett.*, 126(17): 172503, Apr 2021. doi: 10.1103/PhysRevLett.126.172503. URL `https://link.aps.org/doi/10.1103/PhysRevLett.126.172503`.

R. Richards. Vector analyzing power measurements for PREX-II. `https://drive.google.com/file/d/1ztzUvSni7X7dOx-d5uXtMcTwq71VE04_/view?usp=sharing`, 2020.

S. Riordan, S. Rahman, ···, and MOLLER Simulation Group. Simulations for the MOLLER experiment at Jefferson Lab. `https://github.com/JeffersonLab/remoll`, 2013.

S. Riordan, Y. X. Zhao, ···, and S. Rahman. Study of light backgrounds from relativistic electrons in air light-guides. *Nucl. Instrum. Methods Phys. Res. A*, 896: 96–102, July 2018. URL `https://doi.org/10.1016/j.nima.2018.04.029`.

X. Roca-Maza, M. Centelles, X. Viñas, and M. Warda. Neutron skin of ^{208}Pb, nuclear symmetry energy, and the parity radius experiment. *Phys. Rev. Lett.*, 106(25):252501, June 2011. doi: 10.1103/PhysRevLett.106.252501. URL `https://journals.aps.org/prl/abstract/10.1103/PhysRevLett.106.252501`.

C. H. Rode. Jefferson Lab 12 GeV CEBAF upgrade. *AIP Conf. Proc.*, 1218(1):26–33, Apr. 2010. URL `https://aip.scitation.org/doi/pdf/10.1063/1.3422362`.

E. Rojas and G. Erler. Alternative Z´ bosons in E(6). 2015(10):63, Oct 2015. URL https://doi.org/10.1007/JHEP10(2015)063.

M. Steigerwald. MeV Mott polarimetry at Jefferson Lab. *AIP Conf. Proc.*, 570 (1):935–942, June 2001. URL https://aip.scitation.org/doi/10.1063/1.1384229.

The Jefferson Lab QWEAK Collaboration. Precision measurement of the weak charge of the proton. *Nature*, 557(7704):207–211, May 2018. doi: 10.1038/s41586-018-0096-0. URL https://doi.org/10.1038/s41586-018-0096-0.

The SLAC E158 Collaboration. Precision measurement of the weak mixing angle in møller scattering. *Phys. Rev. Lett.*, 95(8):081601, Aug 2005. doi: 10.1103/PhysRevLett.95.081601. URL https://link.aps.org/doi/10.1103/PhysRevLett.95.081601.

Vector Fields Inc. TOSCA data sheet. http://oss.jishulink.com/caenet/forums/upload/2012/07/16/159/52981267106456.pdf, 2012.

C. Wieman and A. Derevianko. Atomic parity violation and the Standard Model. Mar. 2019. URL https://arxiv.org/abs/1904.00281v1.

J. Woithe, G. J. Wiener, and F. F. Van der Veken. Let's have a coffee with the Standard Model of particle physics! *Phys. Educ.*, 52(3):034001, Mar. 2017. URL https://doi.org/10.1088/1361-6552/aa5b25.

C. S. Wu, E. Ambler, R. W. Hayward, D. D. Hoppes, and R. P. Hudson. Experimental test of parity conservation in beta decay. *Phys. Rev.*, 105(4):1413–1415, Feb. 1957. URL https://doi.org/10.1103/PhysRev.105.1413.

T. Ye. Calibrating the sensitivity of high-rate asymmetry measurements to beam motion. In *2020 Fall Meeting of the APS Division of Nuclear Physics*. American Physical Society, Nov. 2020. URL https://drive.google.com/file/d/1JSC5DyuGlOOQgTMs__-_gm7qnHudbxOq/view?usp=sharing.

T.-G. Yue, L.-W. Chen, Z. Zhang, and Y. Zhou. Constraints on the symmetry energy from PREX-II in the multimessenger era. Feb. 2021. URL https://arxiv.org/abs/2102.05267v1.

A. Zec. Compton polarimetry for the PREX-II experiment. In *2020 Fall Meeting of the APS Division of Nuclear Physics*. American Physical Society, Oct. 2020. URL https://drive.google.com/file/d/1JDybhH2dk3uWsOzjq0wBffQ5YIDfptIB/view?usp=sharing.

W. Zhang and S. Park. PREX-2 carbon contamination. https://prex.jlab.org/cgi-bin/DocDB/private/ShowDocument?docid=460, 2020.

Y. Zhao. An introduction to the contamination background study for MOLLER. https://moller.jlab.org/cgi-bin/DocDB/public/ShowDocument?docid=691, 2015.

P. A. Zyla, W. Zheng, $\cdots$, and Particle Data Group. Review of particle physics. *Progress of Theoretical and Experimental Physics*, 2020(8), 08 2020. ISSN 2050-3911. doi: 10.1093/ptep/ptaa104. URL https://doi.org/10.1093/ptep/ptaa104. 083C01.